Alma Mater Studiorum · Università di Bologna

Scuola di Scienze
Dipartimento di Fisica e Astronomia
Corso di Laurea Magistrale in Fisica

Experimental investigation and modelling of mid-infrared quantum cascade detectors operating at high temperature

Relatore:
Prof. Daniela Cavalcoli

Correlatori:
Prof. Carlo Sirtori

Dott. Azzurra Bigioli

Presentata da:
Giovanni Armaroli

Anno Accademico 2018/2019

Abstract

All'interno della banda di conduzione di materiali semiconduttori, le transizioni ottiche tra stati elettronici confinati possono essere progettate per assorbire fotoni nel medio e lontano infrarosso (4µm $< \lambda <$ 100µm). Queste transizioni sono la base di detector unipolari come il *quantum well infrared photodetector* (QWIP) [1] e il *quantum cascade detector* (QCD) [2]. Nel corso degli ultimi vent'anni si è assistito a un grande interesse nel comprendere le loro proprietà fisiche, così da poter migliorare le loro performance. I *focal plane array* di QWIP, raffreddati a temperature criogeniche, sono al giorno d'oggi la parte essenziale di telecamere ad alta definizione per il medio infrarosso e sono prodotti da varie compagnie. Il QCD, introdotto nel 2004, è basato su una struttura con molteplici pozzi quantici progettata per avere un processo di detezione di tipo fotovoltaico. In termini di rumore questo dispositivo è una promettente alternativa al QWIP, che generalmente soffre di un'alta corrente di buio [3].

Nel caso dei QWIP, un recente studio [4] ha dimostrato un metamateriale, chiamato *patch-antenna*, che è in grado di migliorare le performance del detector, specialmente ad alta temperatura. In questa geometria il dispositivo è posto all'interno di una cavità risonante composta da due piastre metalliche, che producono due effetti: concentrano ed aumentano il campo elettrico locale, incrementato l'interazione radiazione-materia, e agiscono come un'antenna, aumentando l'area effettiva in cui i fotoni sono raccolti.

Nel presente lavoro di tesi abbiamo studiato un dispositivo nel quale la regione attiva di un QCD a 8.6µm è stata inserita in una geometria di tipo *patch-antenna*. Su questo dispositivo abbiamo effettuato in primo luogo misure elettriche, per valutare le sue proprietà di trasporto in assenza di illuminazione. In questa situazione il trasporto è attivato termicamente e regolato dal livello di Fermi e dall'energia di attivazione. Abbiamo estratto l'energia di attivazione dalle misure di corrente di buio a diverse temperature e abbiamo confermato i nostri risultati con una simulazione degli stati elettronici nella regione attiva del dispositivo. In seguito abbiamo caratterizzato il processo di foto-detezione e la sua dipendenza dalla temperatura, comparandolo ad un QCD in una geometria standard, chiamata *mesa*. A temperature maggiori di 200 K è in grado di operare solamente il dispositivo patch-antenna e non viene misurata responsività da parte del mesa. Inoltre si osserva che, grazie all'effetto antenna della cavità, il QCD patch-antenna dimostra una buona detettività ad temperature alte, facilmente accessibili con un circuito di raffreddamento termoelettrico. Nell'ultima parte di questo lavoro ci siamo dedicati al progettare e simulare un nuovo QCD patch-antenna, che opera a 4.4µm. L'energia di transizione più alta rispetto al dispositivo a 8.6µm introduce delle sfide nel suo design e nella scelta dei materiali. Per superarle abbiamo introdotto un nuovo tipo di QCD, chiamato *step-well*, in cui sono presenti pozzi quantici di diverse profondità. In questo manoscritto riportiamo come abbiamo simulato questo sistema e presentiamo la struttura finale del QCD che abbiamo progettato.

Abstract

Optical transitions between confined electronic states in the conduction band of semiconducting materials can be engineered to absorb photons in the mid- and far-infrared (4µm $< \lambda <$ 100µm). These transitions are the building blocks of unipolar detectors such as the quantum well infrared photodetector (QWIP) [1] and the quantum cascade detector (QCD) [2]. Over the past twenty years there has been a great effort on the understanding of their physical properties, in order to improve their performance. Focal plane arrays of QWIP detectors, cooled at cryogenic temperatures, are nowadays the essential part of high definition mid-infrared cameras and are produced by several companies. The quantum cascade detector, demonstrated in 2004, is based on a multi-quantum well structure designed to have a photovoltaic detection process. In terms of noise properties, this detector is a promising alternative to the QWIP, that generally suffers from a high dark current [3].

In the case of QWIPs, a recent work [4] has shown that a sub-wavelength metamaterial, named *patch-antenna*, can boost the temperature performance of the detectors. In this architecture, the device is placed within a double-metal resonator, which produces two effects: it concentrates and enhances the local electric field, boosting light-matter interaction, and it acts as an antenna, increasing the effective photon collection area.

In the present thesis work, we studied a device in which a QCD active region operating at 8.6 µm has been inserted into a patch antenna geometry. On this device, we first performed electrical measurements to assess its transport properties in absence of illumination. Under these conditions, the electronic transport is thermally activated and regulated by the Fermi energy and the activation energy. We extracted the activation energy from dark current measurements at different temperatures and validated our results by simulating the electronic energy levels in the active region of the device. Then, we characterized the photo-detection response and its behavior as a function of temperature, comparing it to a QCD in a standard mesa architecture. Above 200K only the patch antenna operates and no responsivity from the mesa can be detected. Moreover, we observed that, thanks to the antenna effect of the double-metal cavities, the patch-antenna QCD displays good detectivity at high temperatures, easily accessible with a thermoelectric cooler. In the last part of the thesis work, we focused on the design and simulation of a new patch-antenna QCD, operating at 4.4 µm. The higher transition energy with respect to the 8.6 µm device, introduces challenges in its design and in the choice of the materials. To overcome them, we proposed a new QCD design, named *step-well*, where quantum wells of different heights are present in the structure. In this manuscript we describe how we were able to simulate such a system and we report the final QCD structure we designed.

Contents

Introduction

This thesis work concerns mid-infrared quantum cascade detectors (QCDs) made of III-V semiconductors, in particular GaAs, AlGaAs and InGaAs. In these devices the photo-detection process is based on intersubband (ISB) transitions, i.e. electronic transitions between energy states in a multi-quantum well structure. The advantage of ISB detectors is the possibility to design and control the electronic confinement by changing geometrical parameters such as the quantum well depth or width, i.e. the *quantum engineering.* Thanks to their ultra-fast response time (in the picosecond range), these detectors are promising for high speed applications, such as imaging and telecommunications. However, QCD performance is still limited by high thermal noise at room temperature, which is the main obstacle to their large scale diffusion. In this thesis work we explore a new QCD geometry, named *patch-antenna*, which is promising for enhancing the high temperature performance of the detector. In this architecture the device is embedded in a double-metal resonator, which enhances the local electromagnetic field and increases the effective photon collection area. In this manuscript we report the results of the characterization of these devices, along with simulations on the QCD active region.

Outline of the thesis

Chapter 1 presents a general discussion of the state of the art in infrared detection. In the first part, we cover the main practical applications concerning this spectral region. In the second part we describe the most relevant detector technologies for the infrared, i.e. the thermal and photonic ones, with a particular focus on the latter. We also introduce the figures of merit used to evaluate the performance of photonic infrared detectors.

Chapter 2 introduces the quantum cascade detector and its opto-electronic properties. In the first part, we recall the basic concepts of heterostructures and quantum wells, which are the building blocks of the QCD structure. In the second part, we cover the principles of optical transitions between subbands in quantum well structures, the physical mechanism that is at the basis of the QCD working principle. In the third part, we explain how a QCD is designed and we present the state of the art theoretical model of transport inside the device, along with a simplified transport model we developed. In the last part, we report the dark current measurements on the 8.6µm QCD, object of this thesis work. We also show the results of simulations we made on the active region of the device and compare them to the experimental data.

Chapter 3 presents the advantages of coupling infrared intersubband detectors to double-metal microcavities. In the first part, we cover the theory of optical waveguides and the latest advances in the study of optical properties of microcavity gratings. The second part presents the experimental results of the optical characterization we performed on the patch-antenna 8.6µm QCD. In particular, we report the results of the spectral response, responsivity and detectivity as a function of the detector temperature.

Chapter 4 covers the simulation and design of QCDs. In the first part, we recall the theoretical aspects at the basis of simulations of multi quantum well structures. In the second part, we describe how we simulated and designed a new type of QCD structure, operating at a 4.4µm wavelength.

Chapter 1

Infrared detection

The infrared (IR) band is the portion of the electromagnetic spectrum between the visible and the microwave bands. As Figure 1.1 shows, the IR can be divided into three regions: the near infrared (NIR), which extends from 0.75 to 2.5 µm, the mid infrared (MIR), from 2.5 to 30 µm and the THz range (also called Far Infrared), from 30 to 1000 µm.

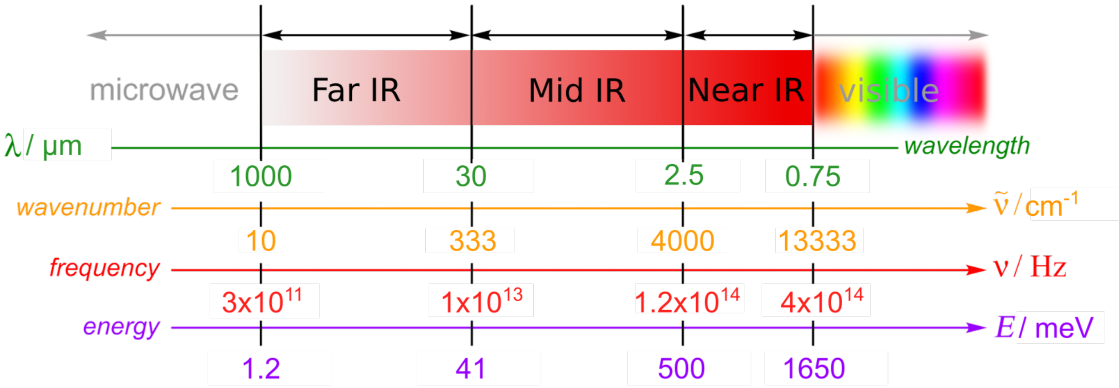

Figure 1.1: Schematic representation of the Infrared electromagnetic spectrum.

In this thesis we explore a type of quantum detector working in the mid-infrared range, for applications in molecular spectroscopy, thermal imaging and telecommunications. In the following we will cover how infrared detectors work and the main applications in this spectral region.

1.1 Applications in the infrared

There are many applications that take advantage of infrared radiation. Indeed, the IR spectral region is extensively used for scientific, security and civilian purposes. Herein we present the three most relevant applications: thermal imaging, molecular spectroscopy and telecommunications.

1.1.1 Thermal imaging

Due to Planck's law, any object with temperature close to room temperature emits radiation in the infrared band, with a peak of emission at a wavelength set by the temperature itself. Taking advantage of this phenomenon, cameras with sensors that detect infrared radiation can be used to determine the temperature of any body they are pointed at. A typical application is the determination of where heat losses in houses come from. Figure 1.2 shows a picture of a house taken with an infrared camera, where the color scale represents the value of temperature. It can be clearly seen that in this case windows are the main cause of heat loss. This technique is important from an environmental point of view, since it allows to determine where heat isolation has to be improved, in order to avoid waste of energy. Thermal imaging is also used to measure the temperature of the oceans from the satellites, to obtain data regarding the effects of global warming.

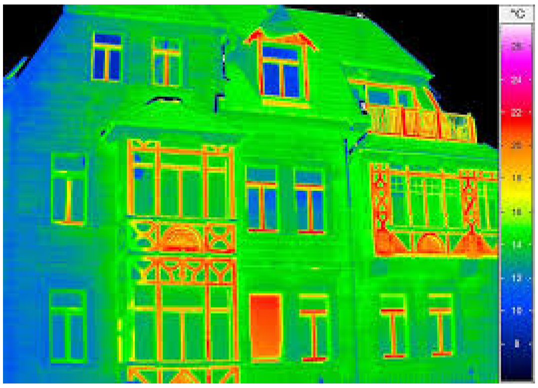

Figure 1.2: Image of the exterior of an house captured with an infrared camera. The color scale indicates the temperature. It is clear that in this case the most heat losses come from the windows (from [5]).

In the security and military domains, cameras that detect infrared radiation are used by the police and the army for night vision. In fact, at night there is no emission in the visible spectrum from the bodies in the environment, but there is still emission in the infrared due to their temperature, allowing to detect the presence of other humans in the dark. Moreover, with this technique missiles can be guided in the night towards their targets, typically planes, thanks to the thermal emission of their motors. These cameras are also used by firefighters to find living body caught in smoke clouds or to prevent the spread of fires on a large scale by localizing early the seats of fire.

1.1.2 Molecular spectroscopy

Having a 3 dimensional structure, molecules can rotate and vibrate in space. Their rotational and vibrational energies are quantized, i.e. they can assume only discrete values, which are determined by the structure of the molecule itself. Thus, photons with an energy equal to the difference between two roto-vibrational levels of a certain molecule are absorbed by it. In many molecules, these resonant energies fall in the IR range, making IR spectroscopy a very useful technique to study the composition and the structure of molecules. This technique consists of passing an IR beam through the sample and measure the percentage that is transmitted, i.e. the transmittance. In the final spectrum, dips appear at photon energies that correspond to a resonance frequency and by studying them it is possible to obtain compositional and structural information about the molecule. Figure 1.3 shows an example of an IR spectrum of the hexanoic acid, with the indication of which chemical bonds cause the transmission dips.

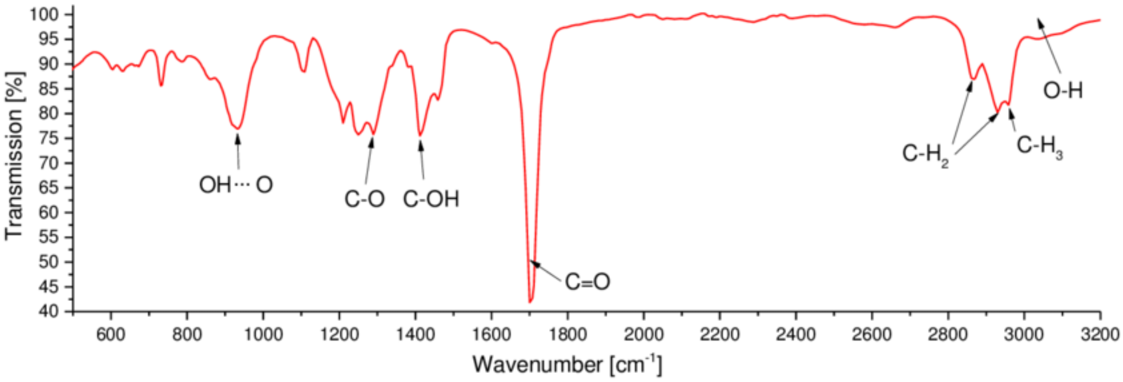

Figure 1.3: IR spectrum of the hexanoic acid. Dips in the transmittance occur when the photon energy resonates with a roto-vibrational transition of the molecule (from [6]).

1.1.3 Free space optical communication

Free Space Optical (FSO) Communication is an emerging technology that refers to transmission of information in unguided propagation media through the use of IR, visible or UV beams. It allows for wireless and fast data transfer between two fixed points over distances up to several kilometers. It also provides high optical bandwidth and therefore a much higher bit-rate than radio-frequency communication [7].

For FSO communication to be possible it is necessary to work with photon wavelengths that are not absorbed by the air, otherwise the signal is lost before reaching the receiver. Figure 1.4 shows the transmittance of the air as a function of the photon wavelengths in the MIR. It is clear that two *atmospheric windows* exist where more than 80% of the radiation is not absorbed by the air: one between 3 and 5 µm and the other between 8 and 14 µm. This is why the interest in the development of high performance sources and detectors operating at these wavelengths has drastically increased. The detectors we characterized for this thesis work operate at 8.6 µm, fitting in the second atmospheric window of the MIR. Fast response (up to GHz) is needed in sources and detectors used in FSO communication, in order to fully exploit its potential. This is why quantum sources such as QCLs and quantum detectors such as QWIPs and QCDs are the best candidates for this technology.

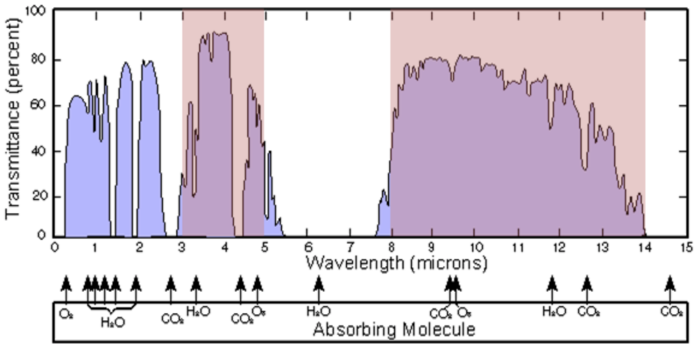

Figure 1.4: Atmospheric transmittance in the MIR range. It is possible to identify two atmospheric windows, at 3-5 µm and at 8-14 µm, where there is a low absorption of radiation by air molecules (from [8]).

This technology is appealing for a wide range of applications. It can be used to transfer data from different buildings on the earth, or to communicate with airplanes and satellites. In addition, it is promising for metropolitan area network (MAN) extension, local area network (LAN)-to-LAN connectivity, backhaul for wireless cellular networks and high definition TV and medical image/video transmission [7].

Despite its huge potential, FSO communication is still limited by its link reliability, especially in long ranges due to atmospheric turbulence. Experimental realizations of FSO in MIR have been demonstrated using a QCL. They show improved performance with respect to NIR in adverse conditions with reduced visibility [9].

1.2 Infrared detectors

There exist two main types of infrared detectors: thermal and photonic. One of the most important differences between these two types of detectors is the dependence of their response on the impinging photon wavelength. As shown in Figure 1.5, thermal detectors display a flat response, while photonic ones show a selective response with wavelength.

1.2.1 Thermal detectors

In thermal detectors, a temperature gradient, following the absorption of the incident radiation, causes the variation of certain physical properties of the material. By measuring this change, it is possible to obtain information on the incident beam. Since the change in temperature is generally does not depend on the photon wavelength, but just on the amount of incident power (or its rate of change), these types of detectors display a flat spectral response with wavelength.

The most important types of thermal detectors are *thermocouples* or *thermopiles*, *pyroelectrics*, *bolometers* and *Golay cells*. The former consists of a thermocouple put in contact with an IR absorbing element. The impinging radiation causes a temperature change in the absorber, which is sensed by the thermocouple. Thermopile

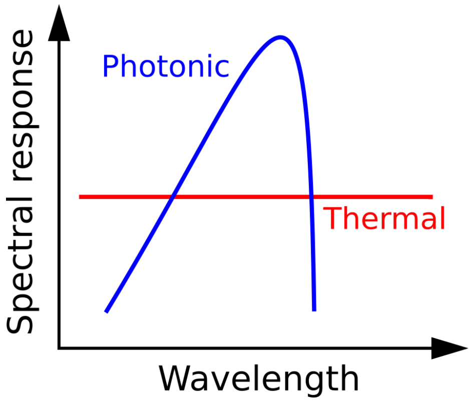

Figure 1.5: Schematic representation of the spectral response of photonic and thermal detector.

sensors are based on the same principle, except that in this case many thermocouples are connected in series, in order to reach a higher temperature sensitivity. Pyroelectric sensors exploit the temperature dependence of the electrical polarization that spontaneously develops in some crystals. The change in temperature caused by the radiation is sensed through a corresponding change in the electrical potential measured across the crystal. In bolometers the temperature dependence of the electrical resistance is used to detect radiation and, to this purpose, different materials can be used: metals, semiconductors and also superconductors. Finally, Golay cell detectors are based on the measurement of a pressure variation in a gas chamber due to the temperature change induced by the incident radiation.

Most thermal detectors work at room temperature, however their performance can be improved by decreasing the operating temperature. One of their biggest advantages is that they cover wide part of the infrared spectral region delivering acceptable values of detectivity, of the order of 10^9Jones (Figure 1.6). However, they are not suited for high frequency applications, due to their low response time, typically of the order of 10 to 100 ms [11]. For these types of applications, photonic detectors are able to provide better performance, since they typically display faster response times.

1.2.2 Photonic detectors

Photonic detectors are based on the interaction between the incoming radiation and the charge carriers in the material. If certain conditions are met, photons are absorbed and their energy is transferred to the electrons, which are excited to a higher energy state. The excited electrons then generate an electrical signal (current or voltage), which is the output of the sensor.

There are two main types of electronic transitions that are exploited to build infrared detectors: interband (IB) transitions and intersubband (ISB) transitions (Figure 1.7). The former type consists of transitions between the valence band and the conduction band of the detector. In this case the minimum photon energy that can be detected is fixed by the band gap energy (E_g) of the material. On

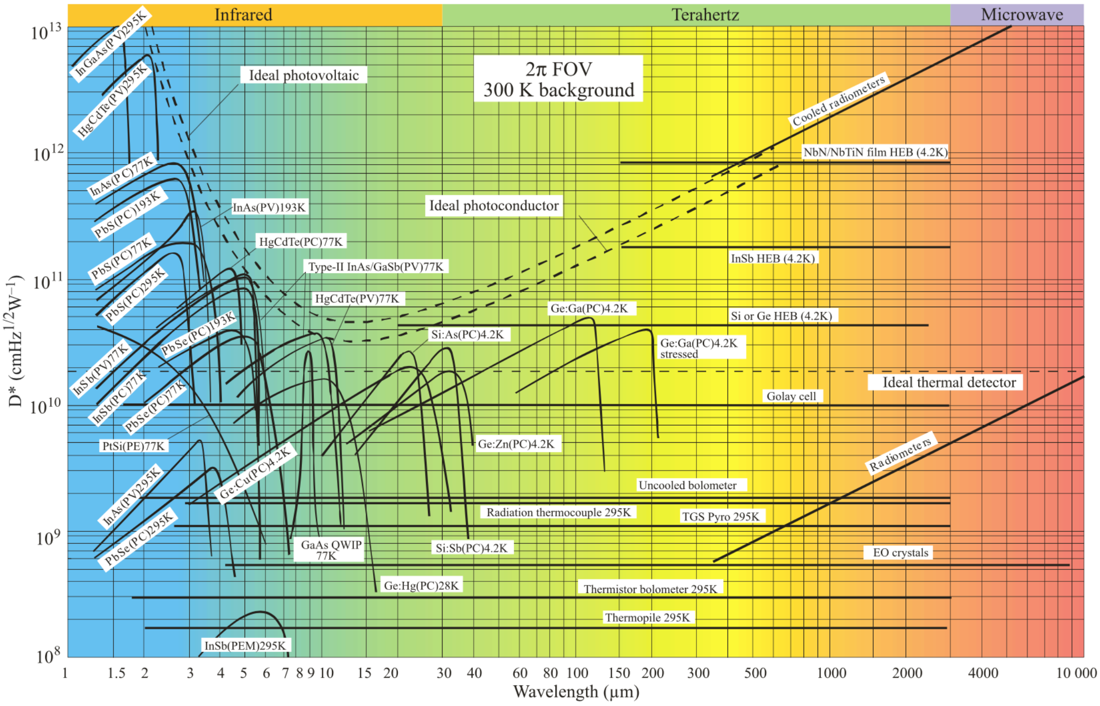

Figure 1.6: Detectivity of available photonic and thermal detectors when operating at the specified temperature (from: [10]).

the other hand, intersubband transitions occur between electronic levels within the same energy band, which might be either the valence band or the conduction band. Typically they occur in quantum structures, such as quantum wells, quantum dots or superlattices. The advantage of this class of detectors is that the transition energy can be set by choosing the right geometrical parameters when growing the quantum structure.

Figures of merit

Before discussing some examples of photonic detectors, we introduce the most important figures of merit that allow to evaluate the performance of such detectors and also give the possibility to compare it with other devices. The following is based on reference [12], where it is possible to find a more in depth description of the figures of merit of photodetectors.

Responsivity

Responsivity is a figure of merit that measures the output of the detector for a given input optical power (P_{in}) and in general it is a function of the impinging photon energy E. The most typical output for a detector is a photo-generated current (I_{photo}), yielding the formula for the responsivity:

$$\mathcal{R}(E) = \frac{I_{photo}(E)}{P_{in}(E)}. \tag{1.1}$$

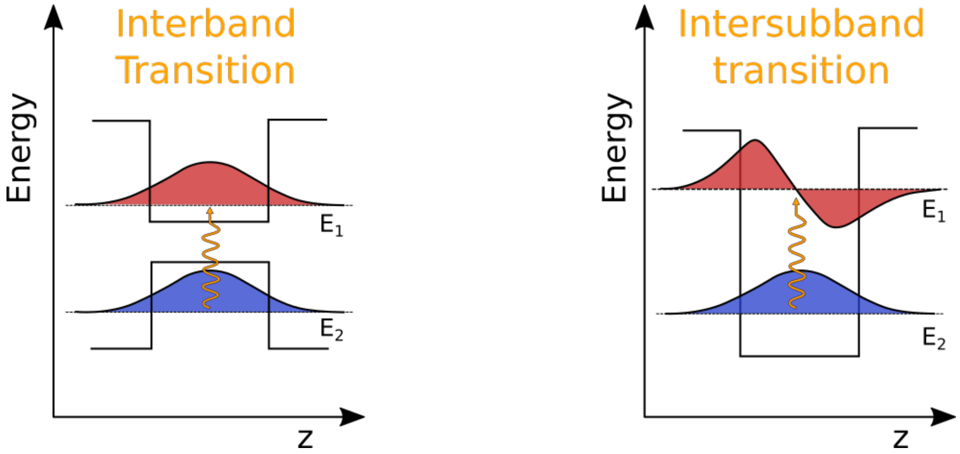

Figure 1.7: Schematic representation of energy as a function of one spatial coordinate for an interband transition (left) and an intersubband transition (right).

The units of the responsivity are then A/W. The photon flux $\Phi(E)$ is defined as the number of photons reaching the detector per unit second and per unit area:

$$\Phi(E) = \frac{1}{A_{det}} \frac{P_{in}(E)}{E}, \tag{1.2}$$

where A_{det} is the area of the detector exposed to the photon flux. Then, the photocurrent can be expressed as the number of charge carriers generated by each photon times the number of absorbed photons per second:

$$I_{photo}(E) = (eg) \times (\eta A_{det} \Phi(E)). \tag{1.3}$$

g is the photoconductive gain, which is generally between 0 and 1 and quantifies the effective photonic charge generated by each photon. η is the quantum efficiency, representing the probability for a photon to be absorbed by charge carriers in the detector. Now, by combining equations 1.1, 1.2 and 1.3 we obtain a new expression for the responsivity:

$$\mathcal{R}(E) = \frac{e\eta g}{E}. \tag{1.4}$$

Noise equivalent power

Any electronic device is affected by noise. There are three most relevant sources of noise in photodetectors. They are the Johnson-Nyquist noise (also known as thermal noise) i_{JN}, the generation-recombination noise i_{GR} and the photon noise i_P. The Johnson noise is due to the thermal energy of electrons, which causes them to randomly move in the device and in the whole circuit. i_{GR} and i_P are instead related to fluctuations in the number of carriers. In the first case these fluctuations are due to generation and recombination processes in the active region of the detector, while in the second case they are due to the quantized and random nature of the light source. We will assume the photon noise to be negligible with respect to the others and thus the expression for the total mean square current noise is:

$$i_N^2 = i_{JN}^2 + i_{GR}^2 = \frac{4k_BT}{R}\Delta f + 4egI\Delta f, \tag{1.5}$$

wherek_B is the Boltzmann constant, T is the device temperature, R is its resistance and I is the total current flowing in the circuit. The signal to noise ratio of the detector is then:

$$S/N = \frac{I_{photo}}{i_N}. \tag{1.6}$$

The noise equivalent power (NEP) is defined as the minimum power that is needed for the detector to produce a signal to noise ratio of 1, for a bandwidth of $\Delta f = 1\text{Hz}$. It is expressed as:

$$NEP = \frac{i_N}{\mathcal{R}\sqrt{\Delta f}}. \tag{1.7}$$

Detectivity

Although the NEP is a quantity that gives valuable information on the detector performance, it is still dependent on the detector area A_{det} and thus not ideal to compare different types of detectors. Therefore it is useful to introduce the specific detectivity, which contains a normalization by A_{det}:

$$D^* = \frac{\sqrt{A_{det}}}{NEP} = \frac{\mathcal{R}\sqrt{A_{det}}}{i_N}\sqrt{\Delta f}. \tag{1.8}$$

Its measurement unit is $\text{cmHz}^{1/2}\text{W}^{-1}$, usually named Jones. Since i_N depends on the detector temperature, also D^* does:

$$D^*(T) = \frac{\mathcal{R}\sqrt{A_{det}}}{\sqrt{4k_BT/R(T) + 4eg\left[I_{dark}(T) + I_{back,photo}\right]}}. \tag{1.9}$$

Here we have separated the two contributions to the total current I flowing in the circuit. The *dark current* I_{dark} is the current that flows in the photodetector in absence of external radiation sources and it is thermally generated in the active region. The current $I_{back,photo}$ is the photocurrent generated by the background, which is usually at room temperature and generates a blackbody radiation that is added to the radiation coming from the source. We define the *background current* I_{back} to be the total current that is not generated by the source, i.e.:

$$I_{back}(T) = I_{dark}(T) + I_{back,photo}. \tag{1.10}$$

We now look at the particular case of photovoltaic detectors, which are the the main interest in this thesis work. These detectors generally work close to 0V bias and in this condition we can consider $I_{dark} << I_{photo}$, thus allowing to define a 0V specific detectivity:

$$D_0^*(T) = \frac{\mathcal{R}_0\sqrt{A_{det}}}{\sqrt{4k_BT/R_0(T) + 4egI_{back,photo}}}, \tag{1.11}$$

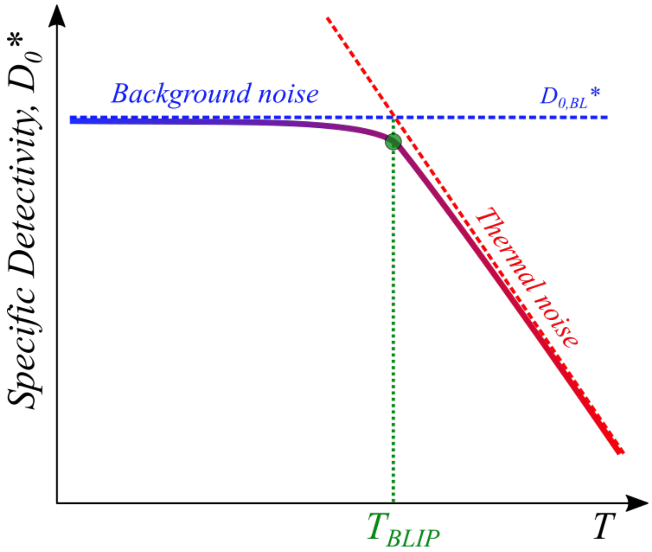

Figure 1.8: Temperature dependence of the specific detectivity at 0V bias. The BLIP temperature separates the two regions of the curve, the background noise limited one (blue) and the thermal noise limited one (red).

where R_0 is the resistance at 0V and it is calculated from the background current-voltage characteristic. At low temperatures the thermal noise becomes negligible with respect to the background noise, while at high temperatures the thermal noise dominates. Since the background noise can be considered temperature independent, the curve $D_0^*(T)$ can be divided into two parts (Figure 1.8). At low temperatures it is constant with temperature (blue line), while at high temperatures it decreases for increasing temperature (red line). The temperature at which these two curves intersect is called *Background Limited Infrared Performance* temperature, T_{BLIP}. The low temperature value of D_0^* is called background limited detectivity $D_{0,BL}^*$.

The *BLIP* temperature is the temperature below which it is useless to cool the detector further. It is then an important parameter to evaluate the temperature performance of infrared photodetectors, which is relevant for practical applications.

Time response

Let us assume that a time dependent optical signal $G(t)$ impinges on a photodetector. This might represent a challenge for the device if the signal varies suddenly or oscillates at high frequency. In fact, if the lifetime of photo-generated carriers τ is lower than the characteristic time in which $G(t)$ varies, then the output signal will not follow exactly the input signal. The equation that describes the time dependence of the number of photo-generated carriers Δn is:

$$\frac{d}{dt}\Delta n + \frac{\Delta n}{\tau} = \eta G(t). \tag{1.12}$$

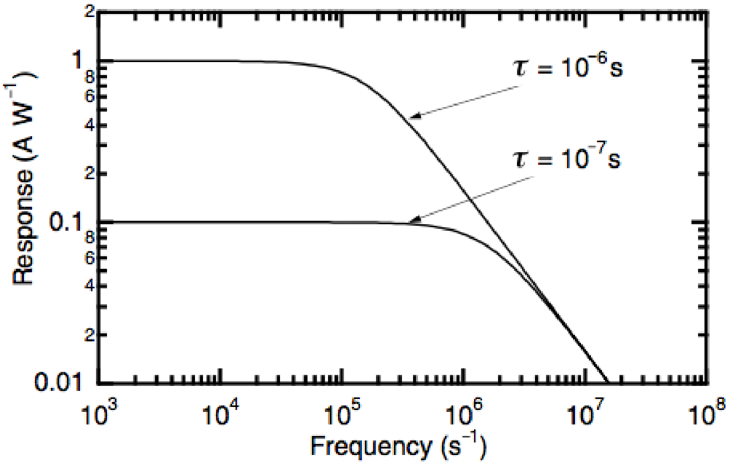

Figure 1.9: Time response of two photoconductors with different carrier lifetimes.

Consider the case of a sinusoidal signal $G(t) = G_0 sin(\omega t)$, then the solution is a sinusoidal response $\Delta n(t) = \Delta n(\omega)\sin(\omega t + \phi)$, with:

$$\Delta n(\omega) = \frac{\eta G_0 \tau}{\sqrt{1+(\omega\tau)^2}}. \tag{1.13}$$

Therefore, the output signal will always have a lower amplitude than the input one (negligible if $\omega\tau << 1$ and $\eta\tau \sim 1$) and a delay, defined by the phase ϕ. Figure 1.9 shows the time response of photodetectors with different carrier lifetimes. A critical frequency exists, below which the output signal is not able to replicate the input one and it is of the order of τ^{-1}. The figure also shows that a compromise between intensity of the output signal and maximum operating frequency has to be found. Indeed, materials with the best responsivities are affected by poor time response, and viceversa.

HgCdTe detector

Mercury Cadmium Telluride (also known as MCT) has been studied and optimized as a material for producing detectors since 1959, when Lawson and others [13] showed the possibility of achieving band gap tunability in this material. This allowed for the production of detectors based on interband transitions that work in different regions of the IR spectrum, covering a broad band from 1 to 12 µm. Nowadays these devices offer a detectivity as high as $D^* = 10^{12}$ Jones [10] and they are the most widely used semiconductor infrared detectors.

However, in the mid-infrared these detectors offer good performance only if cooled down to liquid nitrogen temperature (Figure 1.6). This is because a small band gap is needed for detecting MIR photons (hundreds of meV) and at room temperature electrons have enough thermal energy to overcome the gap and create thermal noise, which compromises the detector's performance. As a consequence, these detectors have to be placed in cryostats (Figure 1.10b) and be continuously cooled down during their operation, imposing practical limitations on some possible

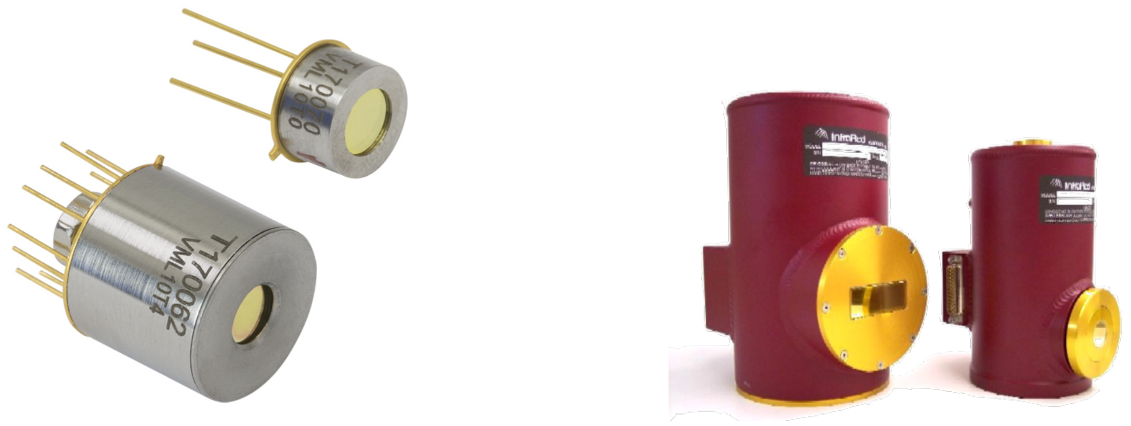

(a) (b)

Figure 1.10: (a) MCT detectors and (b) typical cryostats where they are positioned in order to cool them down to cryogenic temperatures.

applications. Due to the high technological interest in the mid-infrared region, many efforts have been made to find alternatives to MCT detectors, offering comparable performance, but also room temperature operation.

Another limitation of MCT detectors is that their response time of the order of $1\mu s$ [10] limits their frequency response, not allowing for fast applications such as in telecommunications, where GHz operation is required.

Finally, another factor has fuelled the race to alternatives to MCT detectors is the Minamata convention of 2013, which aims for the prohibition of the manufacture, import and export of mercury by the year 2020 [14].

One of the most promising alternatives to MCT detectors are quantum devices based on intersubband transitions. These provide several advantages, such as the possibility of setting the transition energy and fast response times, in the picosecond range. Moreover, they have been shown to provide good performance at room temperature.

Quantum well infrared photodetector

The quantum well infrared photodetector (QWIP) is the most famous example of intersubband detector. It was first proposed in 1987 by Levine and others [1] and it is a photoconductive unipolar device. The device is a stack of alternating layers of two materials with different band gaps, which creates a conduction band profile with multiple quantum wells, sandwiched between two highly doped contact layers, the emitter and the collector.

The absorption occurs in the quantum wells, which are moderately doped ($\sim 10^{11}\text{cm}^{-2}$ for mid-infrared detectors) so that the ground state of the well is populated by electrons. The absorption of photons promotes these electrons to an excited state, which can be either in the continuum (Figure 1.11a), or within the well itself (Figure 1.11b). In the first case, the QWIP is called bound to continuum (B-C), in the second case bound to bound (B-B). In order to collect the excited electrons and prevent them from de-exciting back to the ground state, an asymmetry in the band structure

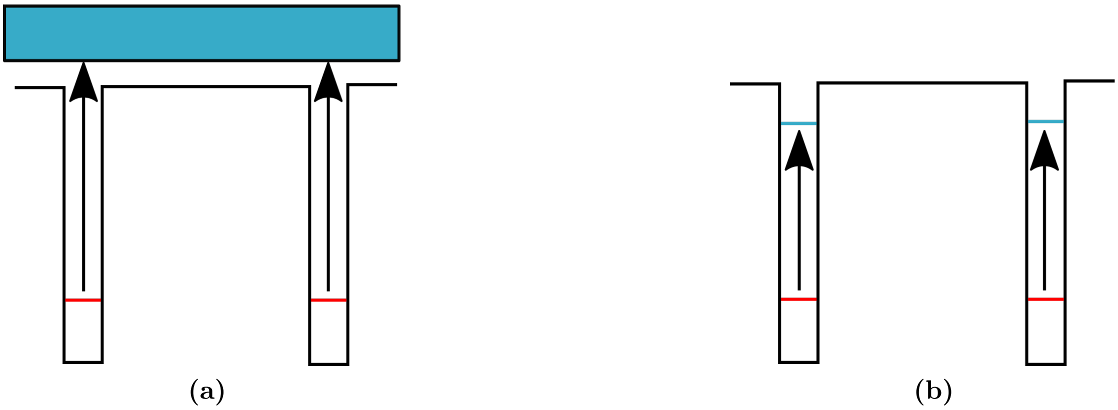

Figure 1.11: Schematic representation of the conduction band profile of (a) bound-to-bound and (b) bound-to-continuum QWIPs.

has to be introduced. This is achieved by applying an external bias, which generates an electric field that allows to collect the charge carriers and measure a photocurrent. Figure 1.12 shows the case of B-B QWIPs, where the photocurrent comes from the photo-excited carriers that either reach the continuum due to thermal excitation or that tunnel through the potential barriers.

Being ISB detectors, QWIPs have the advantage that they can be designed to absorb a particular wavelength. This can be done by changing the well width L_w (by acting on the thickness of the GaAs layer) and the barrier height (through the percentage of AlAs and GaAs in the alloy AlGaAs). Thus, it is possible to build QWIPs that detect radiation in a large range of the IR spectrum, from the THz to the MIR. A major difference with respect to IB detectors is that QWIPs have a narrower spectral response (Figure 1.6), which is centered around the wavelength defined by the transition energy inside the quantum well.

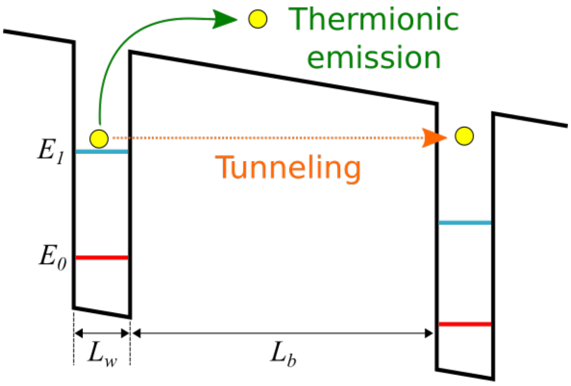

Figure 1.12: Schematic representation of the two main transport mechanisms in a bound-to-bound QWIP: tunneling and thermionic emission. In this case an external bias is applied to the device, causing the band bending.

Nowadays QWIPs provide high performance for IR detection, with competitive detectivity as well as high frequency response, theoretically up to 100 GHz [15].

The main drawback in QWIPs is the dark current, i.e. the current that flows in the device which is not due to photo-excited electrons, but to thermally excited electrons. The dark current exponentially increases with temperature, thus most QWIPs have to be cooled down to cryogenic temperatures to provide high performance operation. However, in the recent years solutions have been found to obtain good performance from these devices, even at room temperature. One example is the work by Ravikumar an others, who have demonstrated a 3-5 µm QWIP based on ZnCdSe/ZnCdMgSe with room temperature operation [16]. In 2018, Palaferri and others used a 9 µm QWIP based on GaAs/AlGaAs as a room temperature heterodyne receiver [4]. They achieved high performance at room temperature by embedding the multi quantum well structure in a double metal patch resonator, which, acting as an antenna, allowed to improve the signal to noise ratio and increase the operating temperature of the device. In this thesis work, we applied the idea of the patch resonators to another type of intersubband detector, the quantum cascade detector.

Quantum cascade detector

Quantum cascade detectors (QCD) are intersubband detectors based on a multi quantum well structure inspired by quantum cascade lasers (QCLs) [17]. They were first introduced in 2004 by Gendron and others [2]. As for QWIPs, the MQW structure is obtained by stacking several layers of two materials with different energy gaps. The width of the quantum wells is engineered in such a way that the electronic eigenstates create a cascade structure, as shown in Figure 1.13. The first well is called the *active well* and it is the only one that is doped. The doping is high enough to push the Fermi level above the ground state of the well, making it populated by electrons. When photons with an energy corresponding to the difference between the ground state and the excited state of the active well impinge on the device, charge carriers are promoted to the excited state. Then, they de-excite along the cascade, through longitudinal optical (LO) phonon scattering, down to the next active well. This structure is typically repeated for N periods in order to ensure a good signal to noise ratio.

The presence of the cascade generates an asymmetric structure that defines a preferential direction for the transport and makes these devices able to work without any external bias, unlike QWIPs. Another difference with respect to QWIPs is that in QCDs the transport is 2-dimensional, because it takes place within the quantum wells and it does not involve transitions to the continuum. This makes the theoretical modeling of the charge transport in QCDs easier to manage with respect to the 3-dimensional one of QWIPs. Moreover, the absence of a strong transport in the active region ensures a lower amount of thermally activated noise with respect to QWIPs, making QCDs devices with a low dark current (which is absent without any applied bias). This has allowed to easily achieve room temperature operation of QCDs. On the other hand, the absence of a strong transport is responsible for a lower responsivity with respect to QWIPs.

Being intersubband detectors, the photon wavelength that is detected can be set by changing geometrical parameters such as the width and height of the active well. QCDs have been demonstrated in the NIR [18], in the MIR [2] and in the THz range

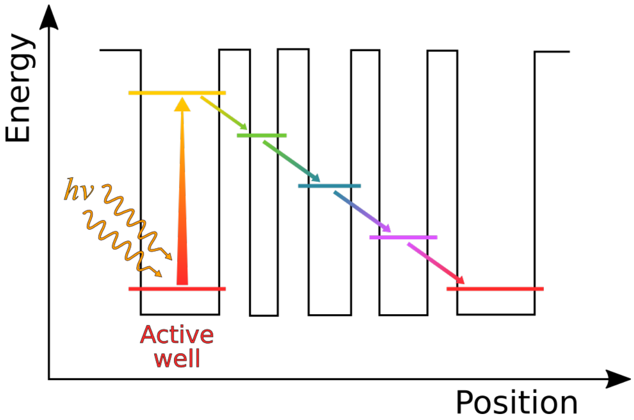

Figure 1.13: Scheme of the conduction band profile of a QCD and of the detection process, with electronic excitation in the active well and de-excitation along the cascade region.

[19]. In addition, QCDs are also promising for high speed applications, due to their response time of the order of picoseconds. Indeed, high speed operation up to 11 GHz has been already reported in QCDs based on GaN/AlGaN heterostructure by Vardi and others [20].

Chapter 2

Quantum Cascade Detector

In this chapter we cover the basics of quantum cascade detectors (QCDs). First, we recall the physics of quantum wells, the building blocks of QCDs, and we cover the theoretical modeling of electronic transitions in quantum structures. Then, we present the theory of thermally activated transport in quantum cascade structures. Finally, we report our experimental results on the characterization of a QCD in dark conditions, which allows to understand the role of thermally activated processes in the device.

2.1 Heterostructures and quantum wells

Heterostructures are systems where at least one interface between two different materials exists. The key characteristic that has determined their success is that they allow to design the conduction and valence band profile of a system. The progress in techniques that enable the control of material growth at the atomic scale has further increased their potential. Indeed, such an accurate growth, following an appropriate design, allows to generate energetic potentials that can confine electronic wavefunctions, paving the way to quantum devices, such as quantum lasers and quantum detectors. Confinement is possible in one, two, or three spacial dimensions and the corresponding systems are called quantum wells, quantum wires and quantum dots, respectively. In this thesis work we will only cover quantum wells, which are the basic components of quantum cascade detectors.

A quantum well (QW) is created by sandwiching a layer of a certain material (as thin as few nanometers) between two layers of another material with higher energy gap. Figure 2.1 shows a transmission electron microscope image of a multi quantum well (MQW) structure, where the wells are created by alternating InAs and $\mathrm{GaAs}_{1-x}\mathrm{N}_x$ layers, where x is a number between 0 and 1 that indicates the percentage of GaN in the alloy.

In the following, we briefly recall the main aspects of the theory of QWs, following references [22–24].

Given a single quantum well with thickness L_z along the growth direction z, the energy of an electron in the well can be calculated with the *particle in a box* model. Using the envelope function approximation, it is possible to write the electronic

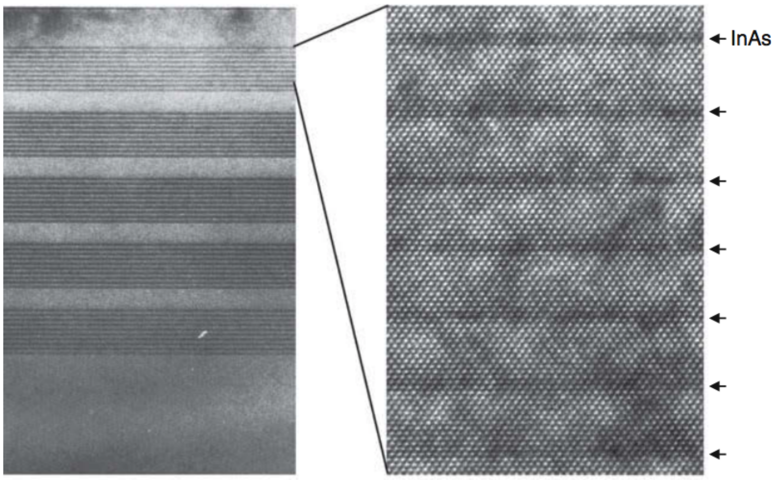

Figure 2.1: Transmission electron microscope image of a multiple QW structure made of InAs in GaAsN. in the high resolution image on the right the individual rows of atoms can be seen (from [21]).

wavefunction as a Bloch wavefunction multiplied by an envelope function $\chi(z)$:

$$\psi(\mathbf{r}) = \exp(i\mathbf{k}_{\perp}\mathbf{r})u_{\nu\mathbf{k}}(\mathbf{r})\chi_n(z), \tag{2.1}$$

where $\mathbf{r}$ is the 3-dimensional position vector, i is the imaginary unit, $\mathbf{k}_{\perp}$ is the in-plane wave vector and ν and n are integer numbers that label specific energy bands and subbands, respectively. According to Bloch's theorem, $u_{\nu\mathbf{k}}(\mathbf{r})$ is a function with the same periodicity as the lattice. Since the potential only depends on the z coordinate, it is possible to decouple the motion in the $x-y$ plane and the one in the z direction. The envelope function fulfills the one-dimensional Schrödinger

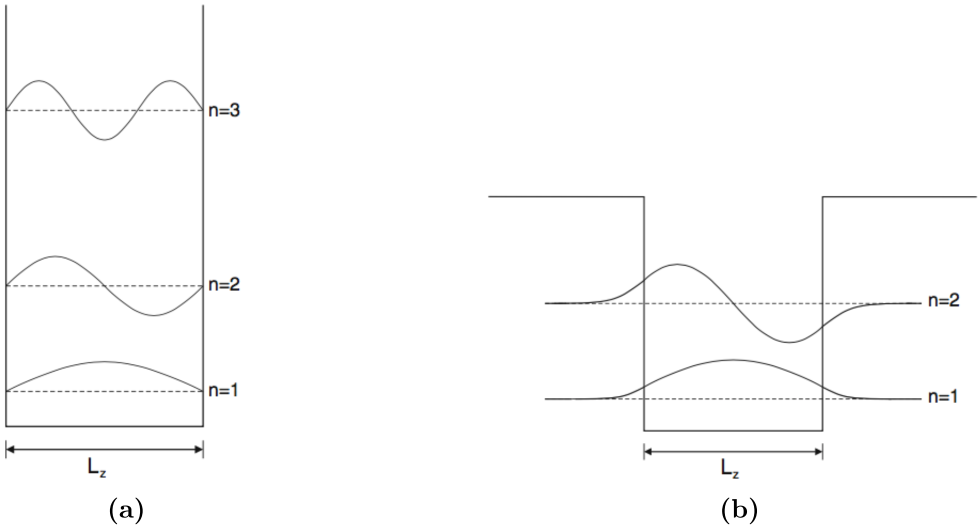

Figure 2.2: Schematic representation of the energy levels and the wavefunctions in (a) an infinite well and (b) a finite well.

equation:

$$\left[-\frac{\hbar^2}{2m^*}\frac{\partial^2}{\partial z^2}+E_c(z)\right]\chi_n(z)=E_n\chi_n(z), \tag{2.2}$$

where m^* is the effective mass of the material that forms the quantum well and E_c is the potential defined by the band discontinuity. We use the convention $E_c = 0$ inside the well and $E_c > 0$ in the barrier. In the approximation of

$E_c \to \infty$ in the barriers, the solution of 2.2 is quite easily calculated setting the boundary conditions $\chi(0) = \chi(L_z) = 0$, yielding:

$$E_n=\frac{\hbar^2}{2m^*}\left(\frac{n\pi}{L_z}\right)^2 \tag{2.3}$$

$$\chi_n(z)=\sqrt{\frac{2}{L_z}}\sin\left(\frac{n\pi}{L_z}z\right), \tag{2.4}$$

where E_n is the confinement energy and assumes discrete values, labeled by n. The equation in the $x-y$ plane yields the energy of a free particle $\hbar^2\mathbf{k}_\perp^2/2m^*$, since there is no confinement along that orientation. The total energy of the system is then given by the sum of the two contributions:

$$E_n(\mathbf{k}_\perp)=E_n+\frac{\hbar^2\mathbf{k}_\perp^2}{2m^*} \tag{2.5}$$

Note that E_n only depends on the effective mass m^*, which contains the transport properties of the material, and a geometrical parameter, the well width L_z. Thus, by changing these two parameters, one can design QW structures following a desired distribution of energy levels. Figure 2.2a shows a schematic representation of the first three solutions (n = 1,2, 3) of the Schrödinger equation for an infinite QW. Real world structures always have finite barriers and in that case Equation 2.2 leads to a transcendental equation that can be solved either graphically or numerically. Figure 2.2b shows the first two solutions of such a finite-barrier QW.

Equation 2.5 introduces the concept of *subbands*. Each value of n defines a subband, which has a free-particle parabolic dispersion relation (Figure 2.3a). Subbands are within an energy band, either the conduction band or the valence band, hence their name. The electronic occupation of each subband is calculated by the use of the Fermionic partition function, which fixes a certain density of energy states $g(E)$ at a given temperature. $g(E)dE$ is the number of states that are found between energies E and $E + dE$ per unit volume. It can be shown that in 2-dimensional systems, like a QWs, $g(E)$ is a step-like function, as shown in Figure 2.3b, and it can be expressed as:

$$g(E)=\frac{m^*}{\pi\hbar^2}\sum_j(E_F-E_j)\Theta(E_F-E_j), \tag{2.6}$$

where E_F is the Fermi energy and Θ is the Heaviside step function. Due to Pauli exclusion principle, charge carriers occupy available states, starting from the one

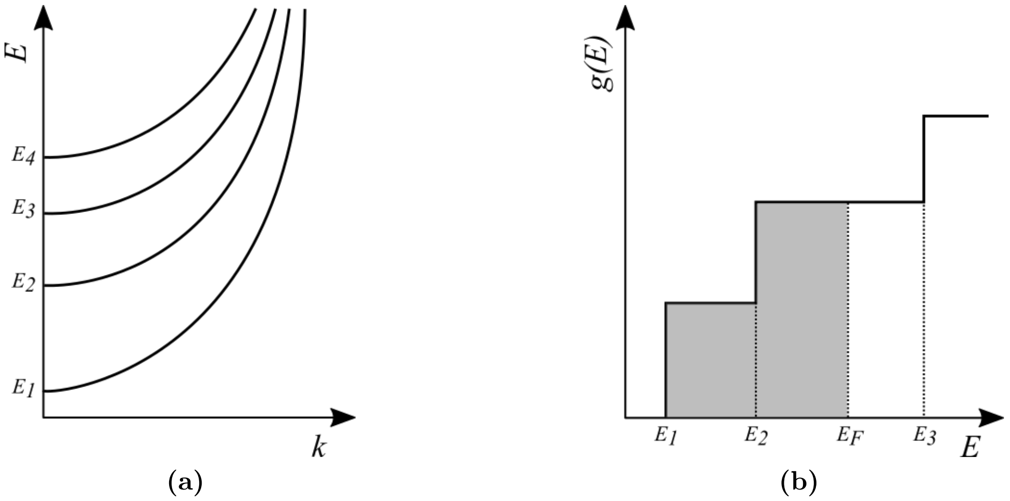

(a) (b)

Figure 2.3: Schematic representation of four subbands in a QW (a) and of the step-like density of states in 2D systems (b), with the grey area representing the occupied states.

with the lowest energy, up to the Fermi level, of energy E_F (Figure 2.3b). The Fermi energy at a temperature of 0K is given by the simple expression:

$$E_F^{0K} = \frac{\pi\hbar^2 n_{2D}}{m^*}. \tag{2.7}$$

Quantum sensors such as QCDs detect radiation thanks to photon-induced electronic transitions between different subbands. In the following section we cover the theory of such intersubband transitions.

2.2 Intersubband transitions

The first experimental observation of intersubband (ISB) transitions in semiconductors was made by West and Eglash in 1985 [25]. They demonstrated a Brewster angle ISB absorption in GaAs/AlGaAs QWs. Since then, an increasing effort has been made to exploit the unique properties of such transitions and produce high performance quantum devices, such as quantum lasers and quantum detectors.

In the following we present the calculations that yield the expression for the *absorption coefficient* in ISB transitions, based on reference [26]. Transitions are induced by an external electromagnetic radiation, which we assume to be monochromatic, with frequency ω and linearly polarized in the direction of $\mathbf{e}$, the polarization vector.

$$\mathcal{E}(\omega) = \mathcal{E}_\mathbf{0} \cos(\mathbf{q} \cdot \mathbf{r} - \omega t)\mathbf{e}, \tag{2.8}$$

where $\mathbf{q}$ is the propagation vector. This wave constitutes an external perturbation for the system, which causes an electronic excitation from an initial state i to a final state f. The transition rate W_{if} from i to f is then given by Fermi golden rule.

$$W_{if} = \frac{2\pi}{\hbar} |\langle\psi_i|H'|\psi_f\rangle|^2 \delta(E_f - E_i - \hbar\omega), \tag{2.9}$$

where δ is the Dirac delta function and H' is the interaction Hamiltonian:

$$H' = \frac{e}{2m^*}\left(\mathbf{A}\cdot\mathbf{p} + \mathbf{p}\cdot\mathbf{A}\right), \tag{2.10}$$

with $\mathbf{p}$ being the dipole moment and $\mathbf{A}$ the vector potential. The latter is defined by $\mathcal{E} = -\partial\mathbf{A}/\partial t$. At this point, we apply the dipole approximation, which assumes the wavelength of the radiation to be large compared to the characteristic dimension of the system, which in our case is the QW width. This generally fulfilled in the infrared, since IR radiation has wavelengths of the order of µm, while typical QW widths are in the range of nm. In this approximation $\mathbf{A}$ and $\mathbf{p}$ commute, yielding:

$$W_{if} = \frac{\hbar}{2\pi}\frac{e^2\mathcal{E}_0^2}{4m^{*2}\omega^2}|\langle\psi_i|\mathbf{e}\cdot\mathbf{p}|\psi_f\rangle|^2\delta(E_f - E_i - \hbar\omega). \tag{2.11}$$

Thanks to the properties of the Bloch functions and considering a slowly varying envelope function, it is possible to split the expression of the matrix element into two terms [27]:

$$\langle\psi_i|\mathbf{e}\cdot\mathbf{p}|\psi_f\rangle = \mathbf{e}\cdot\langle u_\nu|\mathbf{p}|u_{\nu'}\rangle\langle\chi_n|\chi_{n'}\rangle + \mathbf{e}\cdot\langle u_\nu|u_{\nu'}\rangle\langle\chi_n|\mathbf{p}|\chi_{n'}\rangle \tag{2.12}$$

where ν, ν' and n, n' are the band and subband indices of the initial and final states, respectively. The first term is related to interband transitions. It contains a dipole matrix element of Bloch functions, which gives rise to the interband polarization selection rules, and an overlap integral of envelope functions, which determines selection rules for the electron and hole quantum numbers in the subbands. If $\nu = \nu'$, i.e. if the transition occurs within a single band, then this term is null. The second term is instead related to ISB transitions. It contains an overlap integral of Bloch functions, which vanishes if $\nu \neq \nu'$, and a dipole matrix element of envelope functions, which is what determines the ISB absorption. It is then convenient to study separately the latter term:

$$\langle\chi_n|\mathbf{e}\cdot\mathbf{p}|\chi_{n'}\rangle = \int \mathrm{d}\mathbf{r}\chi_n^*(z)[\mathrm{e_x p_x} + \mathrm{e_y p_y} + \mathrm{e_z p_z}]\chi_{n'}(z). \tag{2.13}$$

Due to the orthogonality of the envelope functions, the terms proportional to $\mathrm{e_x}$ and $\mathrm{e_y}$ vanish, except when initial and final states are identical. Thus, the expression for the matrix element that determines the ISB absorption simplifies to:

$$\langle n|\mathbf{p_z}|n'\rangle = \int dz\chi_n^*(z)p_z\chi_{n'}(z). \tag{2.14}$$

This means that, in order to have an ISB absorption process, the electric field of the radiation must have a component along the z direction. This is the well known polarization selection rule for ISB transitions. It plays an important role in the design of detectors, since radiation that has normal incidence on the surface does not generate any ISB transition.

It is useful to define a new quantity named *oscillator strength* between two subbands n and n':

$$f_{nn'} = \frac{2}{m^*\hbar\omega_{n',n}}|\langle n|\mathrm{p_z}|n'\rangle|^2 = \frac{2m^*\omega_{n',n}}{\hbar}|\langle n|z|n'\rangle|^2, \tag{2.15}$$

where $\omega_{n,n'} = (E_n - E_{n'})/\hbar$. This dimensionless quantity allows to compare the transition strengths of different systems. It also has the property that the sum of the oscillator strengths related to the transitions from an initial state n to all the available final states n' is equal to unity:

$$\sum_{n'} f_{nn'} = 1. \tag{2.16}$$

If we consider the case of the transition between the first two levels of an infinite QW, we can easily obtain the oscillator strength f_{12} by calculating the dipole matrix element using the wavefunctions 2.4. The result is $f_{12} = 0.96$, which then results by far the strongest transition from the ground state of the QW. Indeed, due to Equation 2.16, the sum of all other oscillator strengths $\sum_n f_{1,n+1}$ only contributes by 4% to the total excitation process.

We can finally derive the expression of the absorption coefficient for ISB transitions. We consider a flux Φ of radiation impinging at an angle θ with respect to the growth axis of the layers of a multi-QW structure with N_w quantum wells. Then, the absorption coefficient $\alpha_{2D}(\omega)$ is the fraction of electromagnetic energy absorbed by the 2D electron system and it is calculated summing over all the possible transitions the ratio between $W_{nn'}$ and Φ:

$$\begin{aligned} \alpha_{2D}(\omega) &= N_w \sum_{nn'} \frac{W_{nn'}(\omega)}{\Phi A \cos(\theta)} \\ &= N_w \frac{e^2 h}{4\pi\epsilon_0 \mathtt{n} c m^*} \frac{\sin^2(\theta)}{\cos(\theta)} \sum_{nn'} n_{2D} f_{nn'} \frac{\Gamma}{(E_{n'} - E_n - \hbar\omega)^2 + \Gamma^2/4}, \end{aligned} \tag{2.17}$$

where $\mathtt{n}$ is the index of refraction, c the speed of light in vacuum and n_{2D} the 2D density of states. The term $\cos(\theta)$ is introduced because the effective interaction length is $L_w \cos(\theta))$, while the $\sin^2(\theta)$ comes from the polarization selection rule of ISB transition. Indeed, if the incident radiation impinges perpendicularly to the growth direction, the absorption coefficient vanishes. Γ is the half width at half maximum (HWHM) of a Lorentzian distribution that replaces the energy-conserving Dirac delta contained in the transition rate $W_{nn'}$. This is introduced because in real multi-QW structures the carrier lifetime in the excited state is not infinite, but typically of the order of ps and its value depends on the relaxation processes that occur in the system. These processes can be divided into inelastic and elastic ones. Therefore, it is useful to define the linewidth as a sum of two contributions:

$$\Gamma = \hbar \left(\frac{1}{2T_1} + \frac{1}{T_2} \right), \tag{2.18}$$

where T_1 is related to inelastic processes and T_2 to the elastic ones (note that the former contributes only half as strongly as the latter). Typical inelastic relaxation processes are acoustic and optical phonon emission, with the optical one being the most relevant contribution to T_1. Interface roughness scattering or ionized impurity scattering are instead the most usual elastic process and generally they both determine T_2. In order to obtain a narrow linewidth, a precise and slow growth (generally

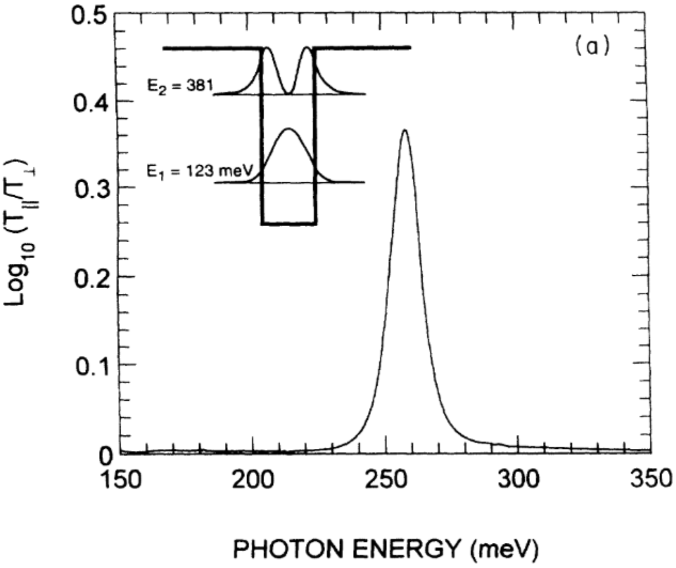

Figure 2.4: Measured absorbance of a AlInAs/GaInAs quantum well (from [28]).

by molecular beam epitaxy) of the QWs has to be done. If performed correctly, this allows to get close to the intrinsic broadening limit due to the only optical phonon emission. Figure 2.4 shows an experimental spectrum of a AlInAs/GaInAs quantum well where a linewidth of few tens of meV is observed.

2.3 Quantum Cascade Detector

2.3.1 Working principle

The quantum cascade detector is a device based on ISB transition in a multi-QW structure. Figure 2.5a shows a computer simulation of the band profile of a QCD operating at 4µm. The structure can be divided into two parts: the active well (well A) and the cascade region (wells from B to H).

The active well is where the photon absorption takes place. It is designed in such a way that it contains two electronic levels (A_1 and A_2). This well is highly doped ($\sim 10^{11}$cm^{-2}), so that the Fermi level is above the ground state A_1, which is therefore populated by electrons. Among the wells in the structure, this is the only one that is doped. When photons with a wavelength corresponding to the energy difference between the two levels (4µm in this case) reach the structure, they excite electrons to the higher energy state A_2.

The charge transfer to the cascade is ensured by resonant tunneling between A_2 and the ground state of well B. It is important that this tunneling process is faster than the relaxation process between the two levels in the active well, otherwise most of the charge carriers would de-excite back to the ground state A_1, producing a significantly lower photocurrent and responsivity. The use of resonant tunneling allows to create a thick barrier that separates the active well from the extraction cascade, with the

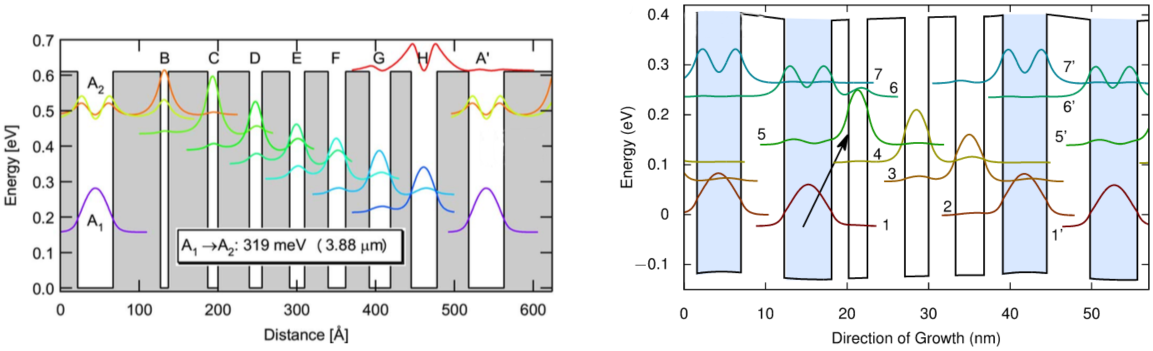

(a) **(b)**

Figure 2.5: Band simulations of quantum cascade detectors. In the regular geometry (a) the optical transition occurs in the first well between levels A_1 and A_2 (from [29]). (b) shows an alternative geometry that exploits a diagonal transition between two different wells (from [30]).

advantage of increasing the device resistance (and thus reduce the thermal noise) without weakening the escape probability. We point out that alternative geometries also exist, such as the diagonal QCD, where the active transition occurs between two energy states situated in different wells (Figure 2.5b). This geometry is particularly efficient and it holds the record for the highest responsivity at room temperature, 17 mA/W [30].

The QWs forming the cascade are engineered in such a way that their difference in energy is close to the longitudinal optical phonon energy E_{LO}. Indeed, the emission of such phonons is the most important relaxation mechanism in QCDs. The value of E_{LO} depends on the materials used to build the device (e.g. 36 meV in GaAs, 32 meV in $In_{0.53}Ga_{0.47}As$ [3]).

The gain of a QCD g is determined by the ratio between the escape probability and the capture probability p_e/p_c. The capture probability is typically close to unity. The escape probability depends mainly on the LO phonon scattering times from the resonant states A_2 and B_1 to the ground state A_1 (τ_{rel}) or to the extractor state C_1 (τ_{esc}). It is defined as $p_e = \tau_{rel}/(\tau_{rel} + \tau_{esc})$, so that a high gain can be achieved by designing the structure in such a way that $\tau_{rel} >> \tau_{esc}$. The relaxation time is typically of the order of picoseconds, thus a resonant tunneling time of hundreds of femtosecond, at most, is needed.

Typically, the structure described above is repeated more times, creating N_p periods. In this way, N_p photons are required in order to generate a single photoelectron. On one hand this decreases the photoconductive gain by a factor of N_p, but on the other hand it increases the absorption quantum efficiency, thus an ideal number of period exists for a given device (for details see [3]).

2.3.2 Electronic transport in QCDs

Thermalized cascade model

This model was first presented by C. Koeniguer and others [31] to describe the *dark current*, i.e. the current in absence of external radiation, of QCDs. The model assumes the interaction between electrons and longitudinal-optical (LO) phonons to be the most relevant mechanism that enables charge transfer in the structure. Interaction with acoustic phonons, interface roughness and electron-electron interaction are not considered in this model. The transition rate $S_{ij}(E)$ (in s^{-1}) from an initial state of energy E in subband i towards subband j is calculated integrating a matrix element involving the electron-optical-phonon Hamiltonian. This integration is carried out considering all the possible final states with energy $E \pm \hbar\omega_{LO}$ in subband j, where $\hbar\omega_{LO}$ is the LO-phonon energy. The rate of phonon absorption is indicated with $S^{a}_{ij}(E)$ and the rate of emission with $S^{e}_{ij}(E)$.

The global absorption rate (G^{a}_{ij}) and emission rate (G^{e}_{ij}) of LO-phonons are calculated through an integration over all the occupied initial states, assuming a Fermi-Dirac distribution of electrons $f(E)$:

$$G^{a}_{ij} = \int_{\epsilon_j - \hbar\omega_{LO}}^{+\infty} S^{a}_{ij}(E) f(E)[1 - f(E + \hbar\omega_{LO})] n_{opt}\, g(E) dE \tag{2.19}$$

$$G^{e}_{ij} = \int_{\epsilon_j + \hbar\omega_{LO}}^{+\infty} S^{e}_{ij}(E) f(E)[1 - f(E - \hbar\omega_{LO})](1 + n_{opt}) g(E) dE, \tag{2.20}$$

where n_{opt} is the Bose-Einstein statistic function accounting for the phonon population, $g(E)$ is the 2D density of states and ϵ_j is the energy minimum of subband j. The total transition rate is then given by the sum of the emission and absorption term:

$$G_{ij} = G^{a}_{ij} + G^{e}_{ij}. \tag{2.21}$$

Figure 2.6a shows the transitions with the highest rate between two consecutive cascades in a GaAs/AlGaAs QCD with 40 periods of 7 quantum wells, at $T = 80\mathrm{K}$. The solid lines represent the main transitions (with rate above $4 \times 10^{18}\mathrm{m}^{-2}\mathrm{s}^{-1}$), whereas the dashed lines concern the other main transitions (with rate above $1 \times 10^{18}\mathrm{m}^{-2}\mathrm{s}^{-1}$ and below the main transitions). Transitions within a single cascade reach rates two orders of magnitude higher, due to the strong electron-LO phonon coupling.

Since QCDs are photovoltaic detectors, they generally work close to 0V. Thus, in this model, the bias V is introduced as a small perturbation in the energy of the system, equal to eV. To describe the system under an external bias we can use the concept of quasi-Fermi level from the theory of the p-n junction. We define a quasi-Fermi level for each cascade of the QCD, so that the quasi-Fermi level of cascade A is related to that of cascade B via: $E^{A}_{F} = E^{B}_{F} + eV$. Each level of cascade A is increased accordingly in energy by an amount of eV, as depicted in Figure 2.6b.

When no bias is applied to the device, thermodynamical equilibrium is reached and the transition rate from a cascade A to its consecutive cascade B is equal to the

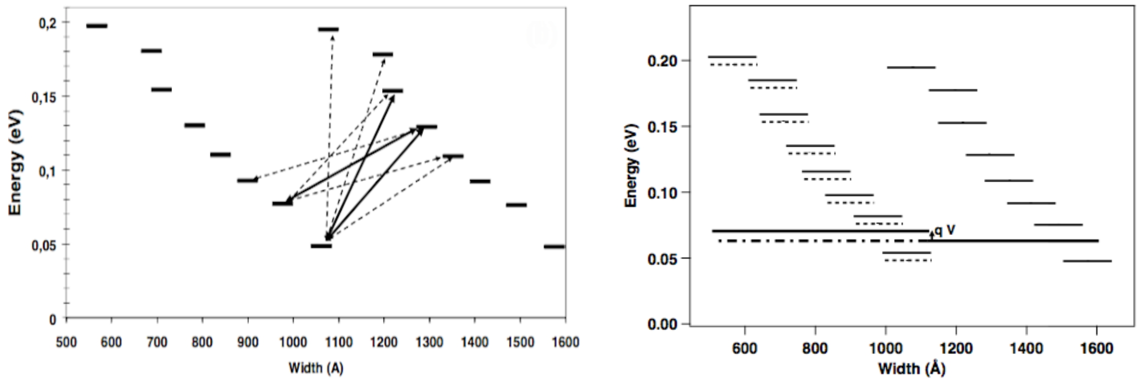

(a) (b)

Figure 2.6: (a) Most relevant transitions between two consecutive cascades of a GaAs/AlGaAs QCD at $T = 80\text{K}$. The solid lines represent the fastest transitions, the dashed lines the other main transitions. (b) Effect of a bias voltage V on a QCD. The dashed lines represent the energy levels at zero bias (from [31]).

transition rate from B to A. Whenever an external bias applied, the equilibrium is broken and a dark current raises:

$$J_d(V) = e \sum_{i \in A} \sum_{j \in B} (G_{ij}(V) - G_{ji}(V)). \tag{2.22}$$

By calculating the contribution coming from the absorption and the emission of LO phonons and assuming no dependence of the electronic wavefunctions on the small bias, the following expression of the dark current is obtained [32]:

$$J_d(V) = J_0 \left[\exp\left(\frac{eV}{k_B T} \right) - 1 \right], \tag{2.23a}$$

$$J_0 = e \sum_{i \in A} \sum (G^a_{ij}(0) + G^e_{ji}(0))_{j \in B} = eG_{tot}. \tag{2.23b}$$

Equation 2.23a is the typical expression of the J-V curve of a diode, with a saturation current J_0 that is related to the transitions taking place within the QCD.

From this model it is also possible to extract a relevant quantity for a photovoltaic detector such as a QCD, the resistance at zero bias R_0. The importance of this parameter stems from Equation 1.11: it determines the thermal noise of the detector. A high value of R_0 is desirable to lower the contribution of the Johnson noise and increase the specific detectivity. By linearizing Equation 2.23a, considering $eV/k_BT << 1$, the following expression for R_0 is derived:

$$R_0 A_{det} = \frac{k_B T}{e^2 \sum_{i \in A} \sum_{j \in B} G_{ij}}. \tag{2.24}$$

It is common practice to normalize R_0 by the detector area A_{det}, to allow comparison among devices with different physical dimensions.

In this model the current is calculated as the result of a variation of the distribution of carriers as a function of the energy from cascade A to cascade B. Thus, the transport inside a QCD can be described as a *diffusion process*, due to the presence of an inhomogeneous chemical potential [31][32]. Therefore, Equation 2.24 can be seen as an Einstein relation which links a macroscopic quantity such as R_0 to the microscopic transition processes described by G_{ij}. Indeed, by considering $R_0 A_{det} = V/J_d$, with $V = \mathcal{E} \cdot l$ and $J_{d=} e n \mu \mathcal{E}$ (l is the period of the structure, n is the 3D electron concentration, μ the electron mobility and $\mathcal{E}$ the amplitude of the applied electric field), we obtain:

$$R_0 A_{det} = \frac{l^2}{e n_{2D} \mu}, \tag{2.25}$$

where $n_{2D} = n/l$. Then we find the usual Einstein relation $D/\mu = k_B T/e$, with the diffusion coefficient D expressed in terms of the transfer rates:

$$D = \frac{l^2 \sum_{i \in A} \sum_{j \in B} G_{ij}}{n_{2D}}. \tag{2.26}$$

Schottky diode analogy of a QCD

As proposed by A. Delga [33] and Z. Asghari [34] in their PhD theses, it is possible to approximate one period of a QCD with an ideal Schottky diode (Figure 2.7). The highly doped active well corresponds to the metal, with electronic states occupied up to the Fermi level. The cascade region, with its intrinsic electronic concentration, corresponds to the depletion region in the semiconductor. The well depth defines the Schottky barrier of the diode.

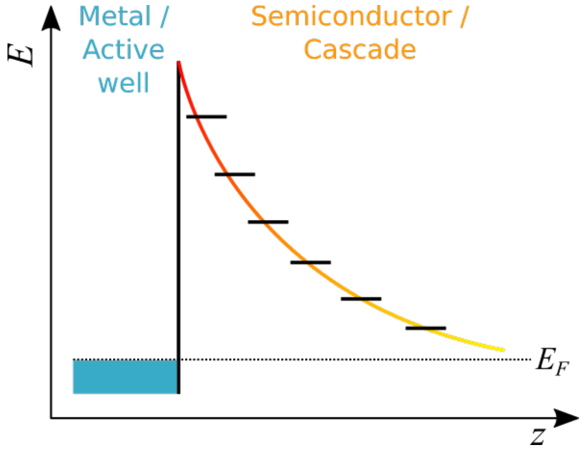

Figure 2.7: Schematic representation of the analogy between one period of a QCD and a Schottky contact.

Using this analogy, on the basis of the results reported above, we obtained a simplified expression for the J-V curves of a QCD, with respect to equations 2.23a and 2.23b. As already discussed, the transport that takes place in a QCD and generates the dark current can be considered as a diffusion process. Therefore, we can adapt to QCDs the classical result of the *diffusion current* in a Schottky diode, which is [23][35]:

$$J_{Diff}(V) = e\mu N_C \mathcal{E} \exp\left(-\frac{F_B}{k_B T}\right)\left[\exp\left(\frac{eV}{k_B T}\right) - 1\right], \tag{2.27}$$

where F_B is the Schottky barrier height and N_C is the conduction band edge density of states, given by $2(m_e k_B T/2\pi\hbar^2)^{3/2}$, with m_e the electron mass. This expression has now to be adapted to the case of QCDs. Using the Einstein relation for the mobility, we can express it as:

$$\mu = \frac{eD}{k_B T}, \tag{2.28}$$

where D is given by 2.26. We can also substitute the Schottky barrier height F_B with the *activation energy*, that we indicate by E_a. This quantity refers to the minimum energy that charge carriers have to acquire in order to generate a dark current in the device. Then, the $J - V$ characteristic of a QCD can be approximated with:

$$J_d(V) = \frac{e^2 D N_C \mathcal{E}}{k_B T} \exp\left(-\frac{E_a}{k_B T}\right)\left[\exp\left(\frac{eV}{k_B T}\right) - 1\right]. \tag{2.29}$$

Then, for small applied biases, it is possible to obtain a temperature dependence of the type:

$$\ln(J_d \cdot T) \propto -\frac{E_a}{k_B T}, \tag{2.30}$$

Then, an Arrhenius-type plot of $\ln(J_d \cdot T)$ as a function of $1/k_B T$ is expected to yield a straight line with slope equal to the activation energy. This is a practical way to obtain an estimate of the activation energy directly from measurements of dark current at different temperatures.

2.4 Characterization of QCD transport

2.4.1 Sample description

In this section we present experimental results and simulations on the QCD operating at 8.6µm which is the main object of this thesis work. The active region is a GaAs/$Al_{0.35}Ga_{0.65}As$ structure with 8 periods of 5 QWs. The active well has a nominal n-type doping of 1.25×10^{18}cm^{-3}. The injector and extractor contacts are made of GaAs with doping of 5 and 6×10^{18}cm^{-3}, respectively. The sample was grown by molecular beam epitaxy at University of Leeds[1]. The growth sheet is reported in Appendix A. The device used for this characterization is in a patch-antenna architecture, as described in Section 3.2.1.

Figure 2.8 shows a simulation of the sample's band diagram, performed using a computer program developed by C. Sirtori[2], A. Vasanelli[2] and others, which solves the Schrödinger equation for a given input potential. Each eigenstate is associated with a letter, that indicates the cascade, and a number, which labels the energy states within a cascade.

---

[1] University of Leeds, Leeds LS2 9JT, United Kingdom.

[2] École Normale Supérieure, 75005 Paris, France.

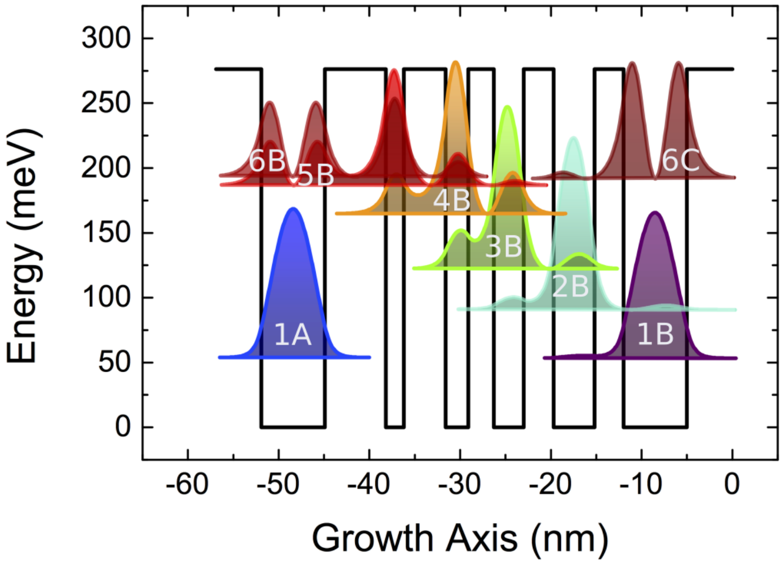

Figure 2.8: Band simulation at 0V bias of the 8.6µm QCD characterized in this thesis work.

2.4.2 Experimental results

In order to characterize the transport properties of the QCD, we measured the current voltage characteristic in *dark* condition. An infrared detector is considered to be in dark condition if the temperature of the environment inside its field of view is lower than or equal to that of the detector (T_{det}). Figure 2.9 shows the experimental setup used to acquire the dark current-voltage (I-V) characteristics of the device at different temperatures. The detector is put in a cryostat in order to control T_{det} through the balance between the flux of liquid nitrogen and a heating wire. Then, within the cryostat, the device is enclosed in a cold chamber, or so called *cryo-shield*, at temperature $T_{shield} \leq T_{det}$, so that the condition for dark measurement is

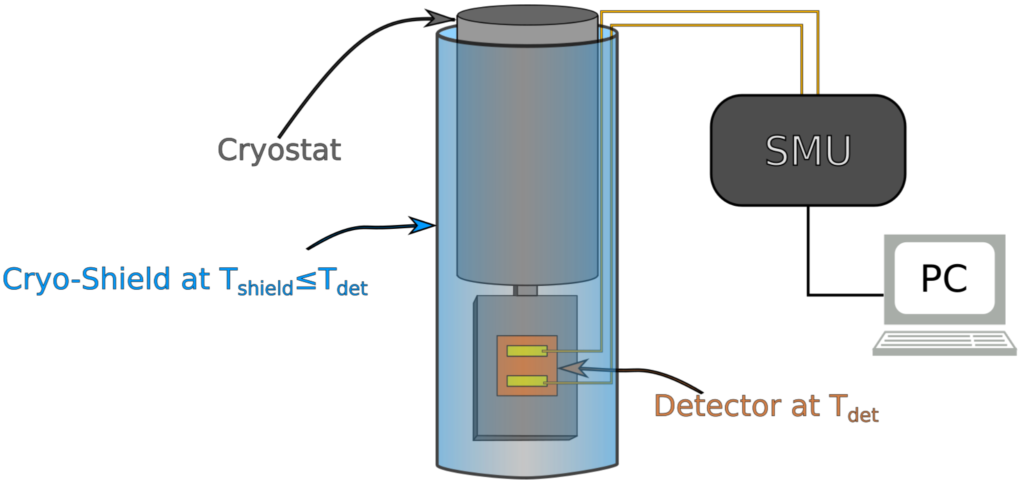

Figure 2.9: Schematic representation of the experimental setup for dark I-V characterization as a function of temperature.

met. The cryostat used for these measurements is a Janis ST-300. The I-V curve is measured by connecting the contacts of the device to the two inputs of a Keithley 2400 Source Measure Unit (SMU). This instrument is controlled by a LabVIEW program and it is able to bias the device and measure the resulting current.

Figure 2.10 shows the dark I-V curves measured with this setup, in the range from liquid nitrogen temperature (78K) to room temperature (300K). The device shows a rectifying I-V, as expected from Equation 2.23a. However, moving closer room temperature an increasingly resistive behaviour is observed. Indeed, the ratio between the currents at +0.8V and -0.8V decreases from 294, at 78K, to 6, at room temperature. Therefore, we can consider Equation 2.23a to be valid only in the low temperature regime. Figure 2.11 shows the differential resistance calculated by differentiation of the I-V curves, $R = (\mathrm{d}I/\mathrm{d}V)^{-1}$.

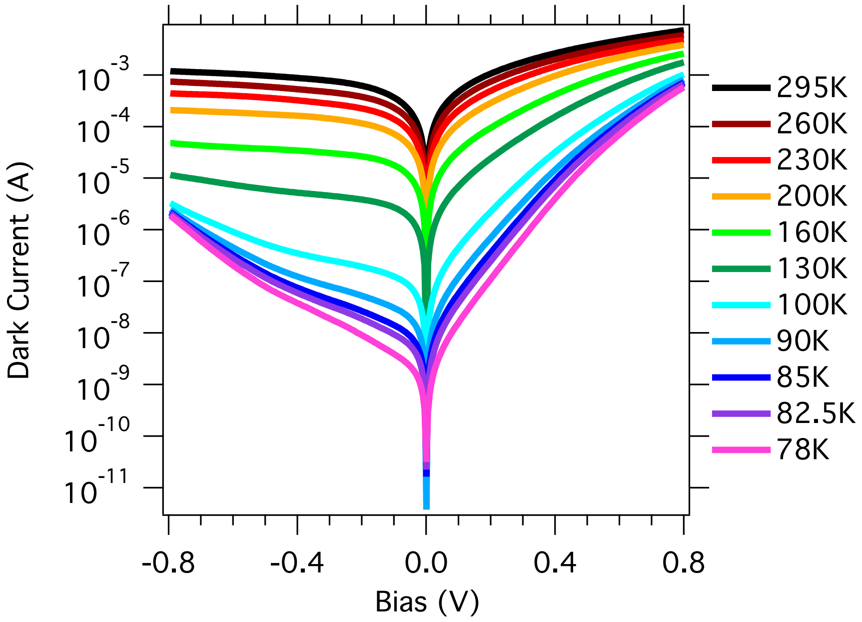

Figure 2.10: Dark current-voltage characteristics of the QCD measured in a temperature range between 78K and room temperature.

From the curves of the resistance we extracted the resistance at 0V bias R_0, as a function of temperature. Its behaviour as a function of inverse temperature is plotted in Figure 2.12. An exponential dependence is observed, as expected from the results reported in the literature [31][32].

From the dark I-V curves we extracted the activation energy following the method reported in Section 2.3.2. Figure 2.13 shows the Arrhenius plots of the product $I_d \cdot T$ at negative and positive applied biases. The red lines are the linear fits from which it was possible to extract the activation energy of the device as a function of the bias. We performed the fits only in the low temperature regime (from 78K to 100K), where Equation 2.23a describes correctly the dark I-V characteristic. The resulting plot of activation energy versus bias is reported in Figure 2.15, where it is compared to the same plot obtained through computer simulations.

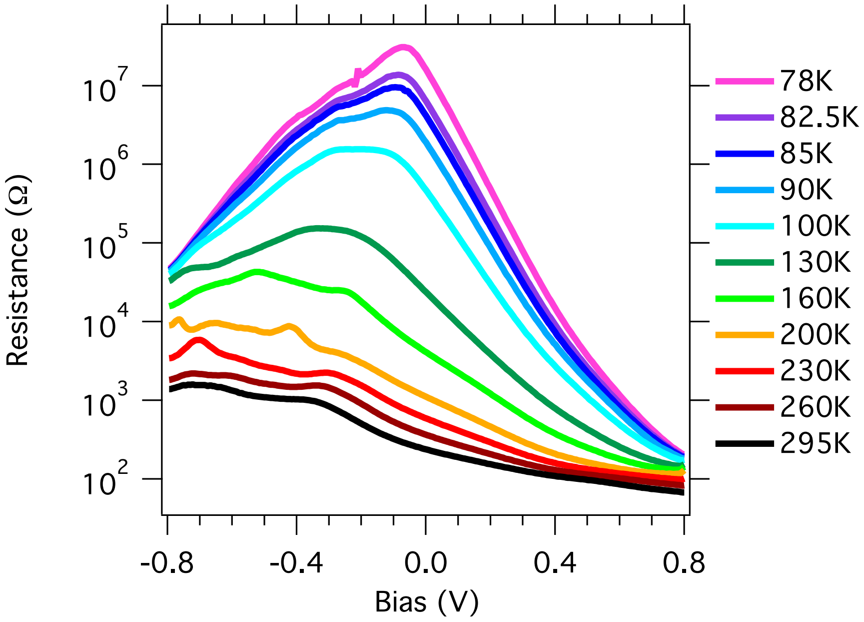

Figure 2.11: Differential resistance of the device calculated from the dark I-V curves.

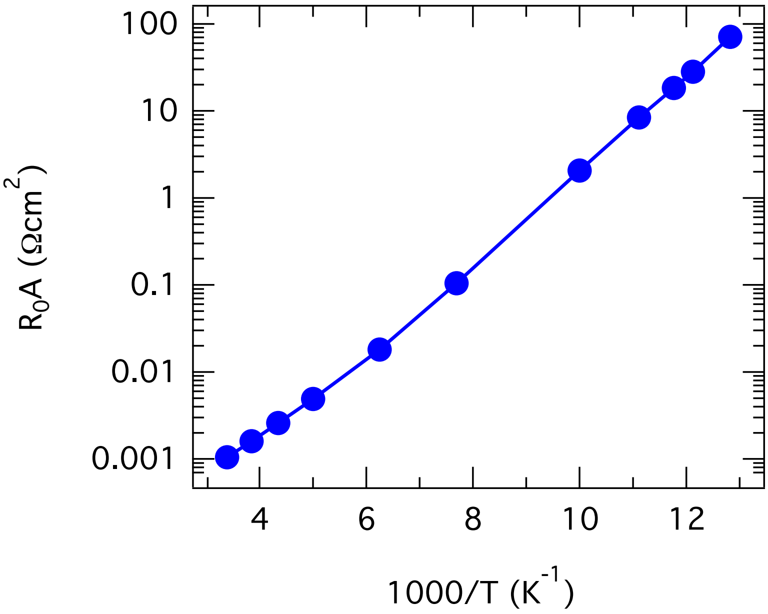

Figure 2.12: Product of the resistance at zero bias times the detector area as a function of inverse temperature.

2.4.3 Active region simulations

The activation energy can also be extracted from simulations on one period of a QCD at different applied biases, considering the thermally activated electronic transitions between energy levels in the system. We considered the initial state of the transitions to be the Fermi level in the active well, which we calculated using Equation 2.7. Considering a value of $m^* = m^*_{GaAs} = 0.067m_e$ and n_{2D} equal to the nominal

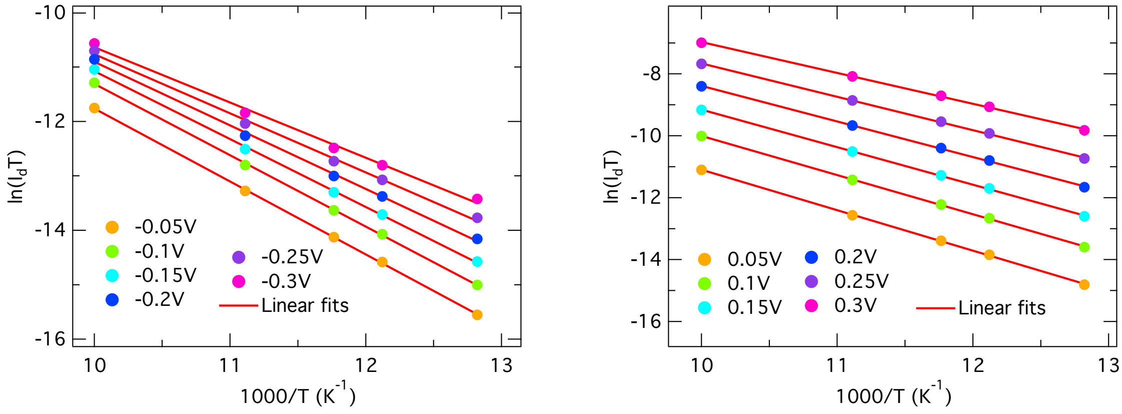

(a) **(b)**

Figure 2.13: Arrhenius plots of the product between the dark current and temperature for negative (a) and positive (b) bias. The red lines are the linear fits from which the activation energy was extracted.

concentration in the active well multiplied by the well width (5nm), we calculated the Fermi level to be 22.33 meV above the ground state of the active well. Then, we chose the final state to be the excited level of the active well, assuming this type of transition to be more relevant than other diagonal ones. However, there actually exist two excited states in the active well of the QCD, with a small energy separation (from 5 to 15 meV, depending on the applied bias). The choice we made on which of the two levels to consider depends on the particular band structure at a given bias. Figure 2.14 shows two simulations of the structure at negative (-0.32V) and positive (0.32V) bias.

At negative bias, the electric field accelerates the excited electrons in the positive direction of the growth axis, so we considered level 1A to be the initial state. The energy of the final state was chosen to be an average of the eigenstates 5B and 6B. The reason for this is that electrons in both of these levels display a not negligible probability of being in the first QW as well as in the second one. This means that both 5B and 6B can concur to the tunneling process that allows thermally activated carriers to access the extraction cascade and generate a dark current. At positive bias the electric field acts in the opposite direction, therefore we chose level 1C as the initial state. Due to the direction of the current, the final state is again at the top of the cascade. In this case, however, the simulation predicts level 6B to give negligible contribution to the tunneling process. Therefore at this bias we considered the final state to be only the 5B level.

We performed the simulations also at ±0.16, ±0.096 and 0 V bias. For each simulation we calculated the activation energy following the procedure described above. The simulated activation energy as a function of the bias is presented in Figure 2.15, where it is compared to the experimental one, obtained with the Arrhenius plot method described in the previous section. The two results show a good agreement, except for the point at -0.32 V. This discrepancy might be due to diagonal transitions that are triggered at such applied bias, decreasing the value of E_a.

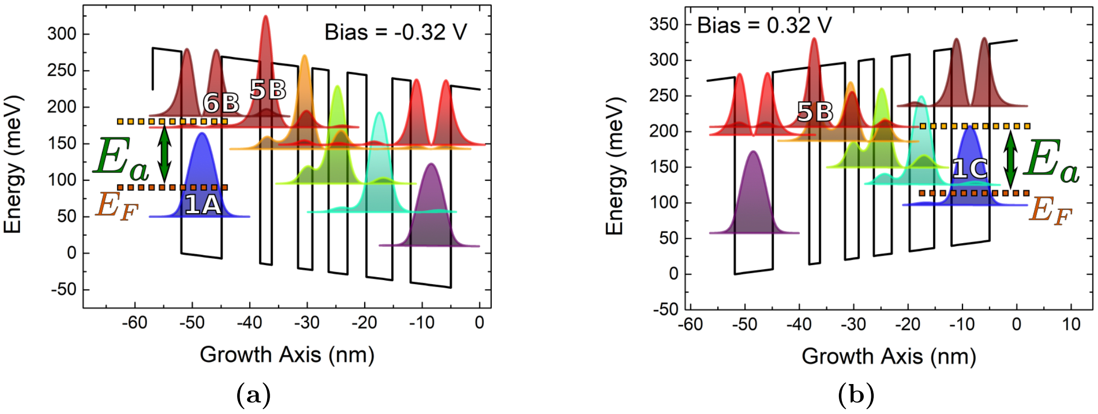

Figure 2.14: Simulations of the QCD active region at ±0.32 V. In both graphs are indicated the position of the Fermi level and the activation energy.

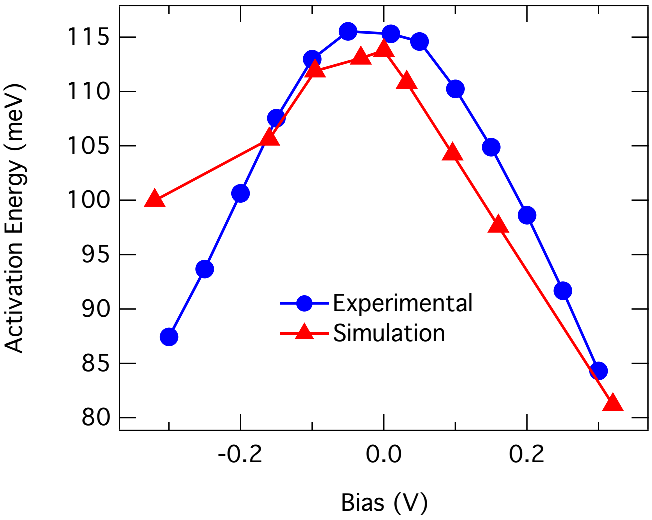

Figure 2.15: Activation energy as a function of the bias applied to the device. The experimental result (blue dots) is compared to the outcome of the simulations (red triangles).

Chapter 3

Patch-antenna microcavities for enhanced MIR detection

In this chapter we cover the optical properties of microcavities and their use for enhancing the performance of MIR detectors. In the first part, we recall the basics of optical waveguide and we report the state of the art theory of arrays of optical microcavities. Then, we show the benefits that such microcavities can bring to MIR detectors performance. Finally, we show our experimental results on the first ever reported optical characterization of a QCD in a microcavity array geometry. We will show that this device shows enhanced responsivity, detectivity and operating temperature with respect to a standard QCD.

3.1 Optical properties of photonic microcavities

This section is divided into three parts. In the first one we cover the theory of one of the simplest types of optical waveguide: the planar waveguide. In the second part we adapt the formalism for a planar waveguide to an array of cavities with sub-wavelength dimensions. Finally, in the third part, we report the recent discoveries on the positive effects that such miniaturized cavities can have on the performance of ISB detectors.

3.1.1 The Planar Waveguide

An optical waveguide is a system that consists of two main parts: a core, where light is confined, and a cladding, surrounding the core. The core and the cladding are made of materials with indexes of refraction chosen in such a way that light undergoes total internal reflection, remaining always within the core.

We will consider the case of metal-dielectric-metal planar waveguides, where a dielectric layer of thickness L, sandwiched between two metallic plates (Figure 3.1), creates a resonant cavity. Maxwell's equations can be used to obtain the expression of an electromagnetic wave propagating in such a system. In absence of electric charges and in the assumption of electric and magnetic fields in the form $\mathcal{E} \propto e^{\boldsymbol{k}\cdot\mathbf{r}-i\omega t}$ and $\mathcal{H} \propto e^{\boldsymbol{k}\cdot\mathbf{r}-i\omega t}$, Maxwell's equations yield the Helmholtz equations [36]:

$$\nabla^2\mathcal{E}(\mathbf{r}) + \omega^2\varepsilon\mu\mathcal{E} = 0 \tag{3.1}$$

$$\nabla^2 \mathcal{H}(\mathbf{r}) + \omega^2 \varepsilon \mu \mathcal{H} = 0 \tag{3.2}$$

where ε and μ are the electric permittivity and magnetic permeability of the dielectric layer. In the planar waveguide there is no dependence of $\mathcal{E}$ and $\mathcal{H}$ on the y direction (using the frame of reference of Figure 3.1), therefore we can set $\partial\mathcal{E}/\partial y = 0$ and $\partial\mathcal{H}/\partial y = 0$. Putting these two conditions into equations 3.1 and 3.2, two independent electromagnetic modes are obtained, denoted as transverse electric (TE) and transverse magnetic (TM) [37]. In the TE mode the electric field is perpendicular to the plane of incidence, with components $(0, \mathcal{E}_y, 0)$ and the magnetic field has in-plane components $(\mathcal{H}_x, 0, \mathcal{H}_z)$. Instead, in the TM mode the magnetic field is transverse to the plane of incidence $(0, \mathcal{H}_y, 0)$ and the electric field has components $(\mathcal{E}_x, 0, \mathcal{E}_z)$. The expressions for for the confined field waves are:

$$\begin{cases} \mathcal{H}_z \propto & \cos(k_z z)\exp(ik_x x) \\ \mathcal{E}_z \propto & \cos(k_z z)\exp(ik_x x) \end{cases}, \tag{3.3}$$

where the z component of the wavevector is quantized due to the boundary conditions imposed by the presence of the metallic plates:

$$k_z = m\pi/L, \tag{3.4}$$

with m an integer number that equals 1,2,3,... in the TE mode and 0,1,2,... in the TM mode. These integers define a set of modes, which are labeled TE$_m$ and TM$_m$. In Figure 3.1 the zeroth, first and second order TM and TE modes are represented.

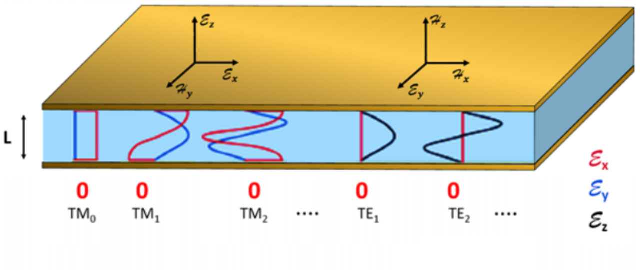

Figure 3.1: Planar metal-dielectric-metal cavity. 0-th, 1st and 2nd order TE and TM modes are schematically represented.

The x-y plane wavevector is indicated with $k_\parallel$ and it follows the dispersion relation

$$k_\parallel = \sqrt{\varepsilon\mu\omega^2 - \left(\frac{m\pi}{L}\right)^2}. \tag{3.5}$$

For a given m, a cutoff frequency ω_{cutoff} exists, below which $k_\parallel$ takes imaginary values:

$$\omega_{cutoff,m} = \frac{\pi m}{L}\frac{1}{\sqrt{\varepsilon\mu}} \tag{3.6}$$

Thus the only mode without a cutoff frequency is the TM$_0$ mode, which shows a light-cone dispersion relation $\omega = k_\parallel/\varepsilon\mu$. Therefore, we can have the excitation of the only TM_0 mode if the radiation has a frequency $\omega \leq \omega_{cutoff,1}$. This condition corresponds to:

$$L \leq \frac{\lambda}{2\mathtt{n}}, \tag{3.7}$$

where $\mathtt{n}$ is the refractive index of the medium. Thus, a mono-mode excitation is achieved if the cavity has a sub-wavelength dimension. For example, if we consider a dielectric layer of GaAs and a MIR radiation with $\lambda = 9\mathrm{µm}$, the refractive index is ~ 3.3 and we obtain a mono-mode condition for $L \lesssim 1.4\mu\mathrm{m}$.

3.1.2 Microcavity gratings

In the previous section we analyzed the case of a macroscopic planar waveguide. In the following we will study how the waveguide properties when the dimensionality of the systems is reduced. In particular, we will consider an array of of square patches (Figure 3.2), where the electromagnetic field is confined in x and y directions.

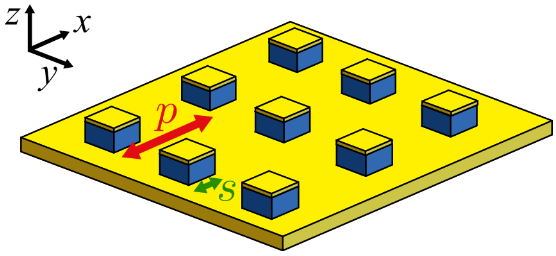

Figure 3.2: Schematic representation of an array of square patches of size s and periodicity p

The patches are squared, with side equal to s, and the periodicity of the structure is defined by $p = s + a$, where a is the distance between two adjacent patches. We consider a GaAs dielectric layer embedded between the two metallic plates, with sub-wavelength thickness $L < \lambda$. As discussed previously, this implies that the only mode that is present within the stripes is the TM_0. Figure 3.3 shows a simulation from reference [38] of the vertical component of the electric field $\mathcal{E}_z$. We observe that $\mathcal{E}_z$ shows a standing-wave behaviour along the confined direction. To understand the mechanism that causes this, it is useful to introduce the effective index of refraction $\mathtt{n}_{eff}$. Its value is approximately that of the GaAs refractive index in the double metal regions ($\mathtt{n}_{eff} = \mathtt{n}_{\mathrm{GaAs}} = 3.2 - 3.3$ in the IR), while in the regions between the stripes it is approximately equal to that of air ($\mathtt{n}_{eff} \approx 1$). This generates an impedance mismatch of the EM modes between the two regions, which causes the reflection of the TM_0 modes at the interfaces, generating a standing wave behaviour [39].

As for any resonant cavity, discrete modes are allowed, which we label with the letters N and M, which take into account confinement in the x and y directions, respectively. The resonant frequencies of the cavity can be expressed as:

$$\nu_{NM} = \frac{c}{2\mathtt{n}_{eff}s}\sqrt{N^2 + M^2}, \quad \lambda_{NM} = \frac{2\mathtt{n}_{eff}s}{\sqrt{N^2 + M^2}}, \tag{3.8}$$

with the corresponding fields of the resonant modes:

$$\mathcal{E}_z(x) = \mathcal{E}_0 \cos\left(\frac{\pi N}{s}x\right)\cos\left(\frac{\pi M}{s}y\right), \quad \mathcal{H}_y(x) = \mathcal{H}_0 \sin\left(\frac{\pi N}{s}x\right)\cos\left(\frac{\pi M}{s}y\right). \tag{3.9}$$

We observe that the resonance frequencies do not show any dependence on the angle of incidence of the radiation. Indeed, from formula 3.8 one can see that ν_{NM} is fixed once the material between the metal plates and the size of the cavities are determined.

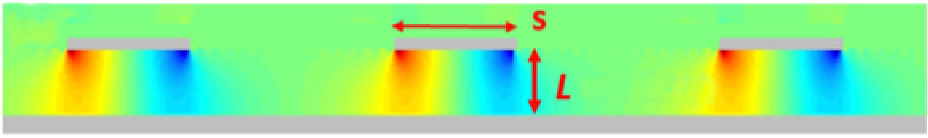

Figure 3.3: Simulation of the vertical component of the electric field $\mathcal{E}_z$ in an row of three square patches. The maximal values are in red and minimal in blue. A standing-wave behaviour is observed (from [38]).

This confinement vanishes for thick resonators (large L). In this case, the resonant modes inside a cavity couple with the neighboring ones, creating a unique de-localized mode [39]. A similar behaviour is observed when, for a fixed thickness L, the separation between stripes a is reduced.

Resonant absorption

When a beam of IR light with a wavelength equal to the resonant mode of the cavity (with wavelength λ_{res}) impinges on it, resonant photon absorption occurs. Under this condition, photons are coupled into the mode and their energy is dissipated by ohmic losses of the metallic plates.

From an experimental point of view this phenomenon can be studied by sending a polychromatic beam of radiation at a certain angle θ onto the structure and measuring the intensity of the reflected beam. Figure 3.4 shows the result of such an experiment on a MIR microcavity of size $s = 1.3$µm. The reflectivity R, i.e. the fraction of reflected radiation, shows a clear dip at an energy corresponding to a resonant mode in the microcavity. The beam is completely reflected ($R = 1$) below 80 and above 200 meV, whereas a strong resonant absorption is observed at around 140 meV, with absorption of 90% of the radiation energy.

The dip minimum with value $1 - R_{min}$, also named contrast C, measures how much energy of the incident wave the structure is able to absorb. It is possible to obtain an expression for the reflectivity as a function of the incident photon frequency using the scattering matrix approach [39][41]. The result is a lorentzian shape, which can be written as:

$$R(\nu) = 1 - \frac{1 - R_{min}}{1 + \frac{(\nu-\nu_{res})^2}{\pi^2\nu_{res}^2}Q^2}, \tag{3.10}$$

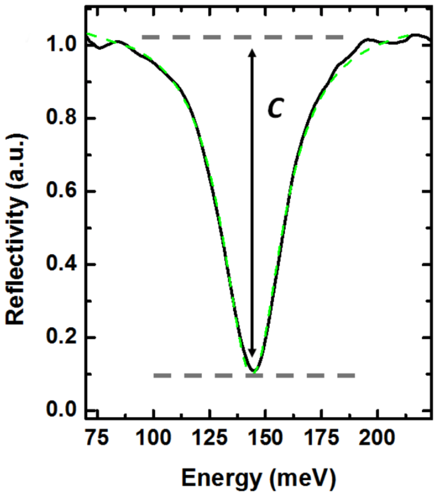

Figure 3.4: First order reflectivity dip of a MIR microcavity of size $s = 1.3\mu m$. The dashed green line is the lorentzian fit of the curve, on the basis of Equation 3.10 (from [40]).

where ν_{res} is the resonance frequency of the cavity and Q is the quality factor of the cavity, defined by $Q = 2\pi\nu_{res}/\Delta\nu$, with $\Delta\nu$ the full width at half maximum (FWHM) of the reflectivity dip. In microcavity structures the value of the quality factor is determined by two components, one related to radiative losses Q_{rad} and one to non radiative losses Q_{loss} (e.g. ohmic energy dispersion in the metallic walls). The quality factor can be calculated through:

$$\frac{1}{Q} = \frac{1}{Q_{rad}} + \frac{1}{Q_{loss}}. \tag{3.11}$$

Patch-antenna effect

It has been shown both theoretically and experimentally that arrays of planar resonators are able to collect the incident radiation from a large cross section [39][42]. Given an array with periodicity p, we can divide it in different cells of area $\Sigma = p^2$ as in Figure 3.5.

Considering an incident photon flux Φ, the contrast $C = 1 - R_{min}$ in the reflectivity spectrum indicates the fraction of absorbed photons. Since the number of incident photons per unit time on each square patch is given by $\Phi\Sigma$, the collection area of each element of the array is [43]:

$$A_{coll} = (1 - R_{min})\Sigma = C\Sigma. \tag{3.12}$$

Thus, from the reflectivity spectrum it is possible to experimentally determine the collection area of the structure. Equation 3.12 indicates that with an appropriate design of the array, it is possible to obtain patches with a collection area larger than the physical area of the patches themselves. This is known as *patch-antenna effect.*

Following [43], we can write the collection area also as:

$$A_{coll} = \frac{A^1_{coll}(Q_{loss})}{\left(1 + \frac{A^1_{coll}(Q_{loss})}{4\Sigma}\right)^2}, \quad A^1_{coll}(Q_{loss}) = \frac{64}{\pi}\frac{V}{\lambda_{res}}Q_{loss}, \tag{3.13}$$

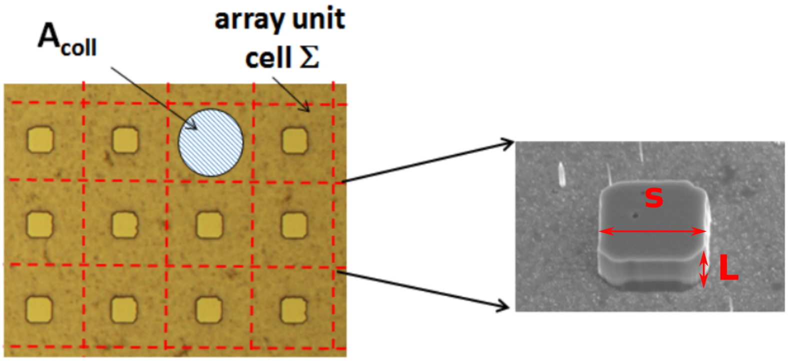

Figure 3.5: Optical microscope image of an array of square patches (left) and scanning electron microscope image of a single patch (right) (from [43]).

where $V = \sigma L$ is the patch volume and λ_{res} the resonant wavelength of the cavity. $A^1_{coll}(Q_{loss})$ is the collection area obtained by letting $\Sigma \to \infty$ for a given Q_{loss} and therefore it is the collection area of a single isolated patch. It is also the largest collection area that we can achieve. Indeed, it is evident from Equation 3.13 that if we increase the array density the collection area of the single patches decreases. Figure 3.6 shows the dependence on Σ of the collection area. Experimental data (in black), obtained from the reflectivity spectra following Equation 3.12, are compared with a simulation (in red), based on Equation 3.13.

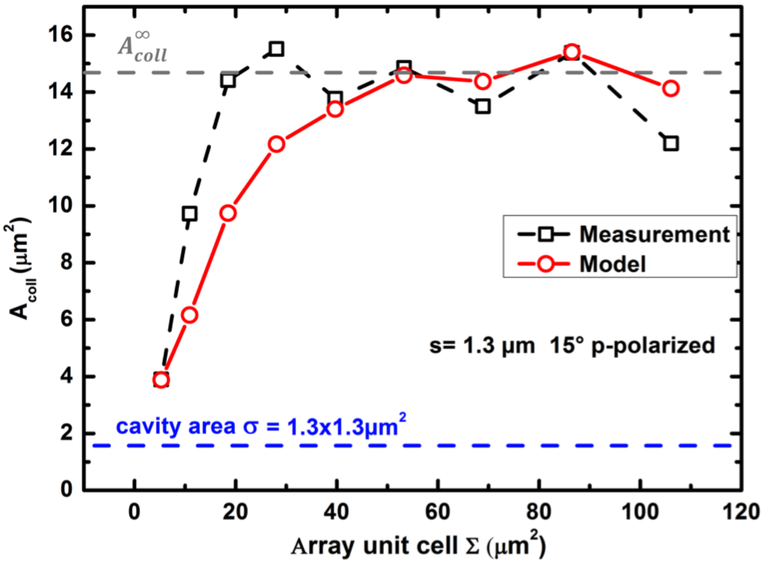

Figure 3.6: Collection area of an individual MIR patch as a function of Σ. The experimental data (in black) are compared with the theory (in red) (from [43]).

3.1.3 Photonic microcavities for enhanced IR detection

Recent works reported in the literature have exploited the extraordinary properties of patch-antenna structures described in the previous section to enhance the performance of ISB infrared detectors. The idea is putting the active region of an IR detector within the double metal cavity in order to increase the effective photon collection area, leading to improved signal to noise ratio and enhanced temperature performance. This idea has been applied so far to QWIP detectors for the THz [44][45] and the MIR [38][4] bands.

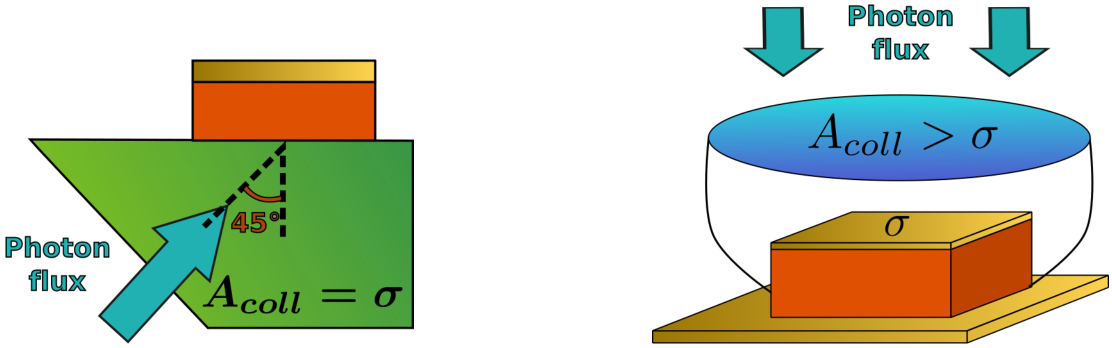

(a) (b)

Figure 3.7: Schematic representations of (a) the mesa geometry and (b) the patch-antenna array geometry.

In the following, we compare two different geometries for IR detectors. The first one is the *mesa* geometry, which is the standard geometry for ISB photodetectors. In the mesa configuration the device is exposed to the radiation through a 45° facet (Figure 3.7a). This angle allows to maximize the ISB absorption in the QWs, due to the ISB polarization rule. In this case, the collection area of the detector is equal to its electrical area σ. The second geometry is the *patch-antenna*, where the active region of the detector is placed in a double metal cavity. In this case, a single device is made of N^2 patches which are connected together to form a $N \times N$ array. As discussed previously, in this configuration there is no more a limitation related to the polarization of the incoming radiation and thus the photon flux can be perpendicular to the detector surface (Figure 3.7b).

ISB absorption and responsivity

Due to the effect on the detector performance of the patch-antenna geometry, we can redefine the figures of merit for IR detectors embedded in double metal cavities and then compare them to those of detectors in a mesa geometry.

According to equations 1.3 and 1.4, the photocurrent generated by a photon flux Φ impinging on a device can be written as:

$$I_{photo} = \mathcal{R} A_{coll} \Phi E_{trans}, \tag{3.14}$$

where $\mathcal{R}$ is the device responsivity and E_{trans} is the energy of the active transition in the device. For a QCD this corresponds to the energy difference between the two levels in the active QW. As discussed in Chapter 2, the dark current can be expressed as

$$I_{dark} \propto \sigma J_0 \exp\left(-\frac{E_a}{k_B T}\right), \tag{3.15}$$

where σ is the electrical area of the device, J_0 is the saturation current density and E_a is the activation energy. From the comparison of Equations 3.14 and 3.15, it is already evident why a patch-antenna geometry can lead to enhanced performance. Indeed, patch devices can have a larger collection area than mesa devices, thus providing a higher photocurrent for the same dark current. If we consider the data in Figure 3.6, in this case the collection area is from two to seven times larger than the electrical area, thus producing an increase in the photocurrent of the same factor, with respect to the mesa geometry.

The mesa quantum efficiency η_{mesa} can be expressed as [38][40]:

$$\eta_{mesa} = N_w L_w \frac{\sqrt{\varepsilon} E_p^2}{4c\hbar^2} \frac{\sin^2\theta}{\cos\theta} \frac{\hbar\Gamma}{(E - E_{trans})^2 + \frac{(\hbar\Gamma)^2}{4}}, \tag{3.16}$$

where N_w and L_w are the number and width of active QWs, θ is the angle of incidence, Γ is the linewidth of the quantum transition and E_p is the plasma energy defined by

$$E_p = \frac{e^2 \hbar^2 f_{12} n_{2D}}{2m^* \varepsilon L_w E_{trans}}. \tag{3.17}$$

The responsivity of the mesa device can be determined following Equation 1.4. However, we need to consider the influence that the geometry itself has on the responsivity. Indeed, only a fraction $\xi_{mesa} = 0.5$ of the radiation couples with ISB transitions, due to polarization selection rule. Moreover, in this geometry, radiation has to penetrate the substrate before reaching the active region, therefore also the transmission coefficient of the substrate t has to be taken into account. The responsivity of the mesa is then given by

$$\mathcal{R}_{mesa} = (t\xi_{mesa}) \times \left(\frac{eg}{E_{trans}} \eta_{mesa}\right). \tag{3.18}$$

The responsivity of an array of microcavity devices can be obtained through a model based on conservation of energy within the cavity, developed in references [38] and [46]. When radiation enters the microcavity, a fraction of its initial energy U enables ISB transitions and the remaining part is dissipated via ohmic losses in the metallic plates. Thus, we can write a rate equation in this form:

$$\left.\frac{dU}{dt}\right|_{cavity} = \left.\frac{dU}{dt}\right|_{isb} + \left.\frac{dU}{dt}\right|_{ohm}. \tag{3.19}$$

In the same way, we can define the quality factor of the cavity related to the ohmic losses Q_{ohm} and the quantity B_{isb}, that defines the fraction of the electromagnetic field absorbed by the ISB quantum transition. Thus, the non radiative loss quality factor introduced in Equation 3.11 can be expressed as:

$$\frac{1}{Q_{loss}} = \frac{1}{Q_{ohm}} + B_{isb}. \tag{3.20}$$

The quantum efficiency of the microcavity array can be seen as the ratio of the ISB dissipation rate and the total dissipation rate within the cavity:

$$\eta_{array} = \frac{B_{isb}}{B_{isb} + 1/Q_{ohm}} = B_{isb} Q_{loss}. \tag{3.21}$$

In an inefficient array, most part of the energy is dissipated though ohmic losses and then $Q_{ohm} << B_{isb}$, leading to $\eta_{array} \to 0$. In the opposite case, $B_{isb} >> 1/Q_{ohm}$ and most part of the energy is used to excite ISB transitions, leading to $\eta_{array} \to 1$. Quality factors are generally kept around 4-5, since a higher value would imply a narrow spectral response, which in practice might not be useful because it would limit the operation of the device to a very small bandwidth. The most efficient situation for real devices is then a tradeoff where $B_{isb} \approx 1/Q_{ohm}$, with $\eta_{array} \approx 0.5$.

The responsivity of the array then becomes

$$\mathcal{R}_{array} = (C\xi_{array}) \times \left(\frac{eg}{E_{trans}} \eta_{array} \right), \tag{3.22}$$

where C is the contrast of the resonant cavity, which determines the fraction of radiation that is actually absorbed by the cavity, and $\xi_{array} = 0.7 - 0.8$ is a polarization coefficient introduced because the metallic wires, which electrically extract the photocurrent from the patches, reflect back the impinging radiation [40].

We can now compare the efficiencies of the mesa and array devices by calculating their ratio:

$$\frac{\eta_{array}}{\eta_{mesa}} = \frac{\cos\theta}{\sin^2\theta} \frac{\lambda_{trans}}{2\pi L} Q_{loss}. \tag{3.23}$$

Let us consider the case of a sub-wavelength microcavity with $\lambda_{trans} = 9\mu m$, $L = 1\mu m$ and an angle of incidence $\theta = 45°$. According to Equation 3.23, in this configuration, a loss quality factor larger than 4.4 is enough to obtain a higher quantum efficiency in the array with respect to the mesa device. This gain in quantum efficiency is easier to obtain in the case of a sub-wavelength microcavity, where the ratio λ_{trans}/L is greater than 1, otherwise a higher Q_{loss} is needed.

Detectivity and temperature performance

We can now compare the specific detectivity D^* of a QCD in the mesa and array configuration, to understand what is the expected impact of the microcavities on the performance of this type of detector.

First, we consider the 0V detectivity of the mesa. Its temperature dependence follows from Equation 1.11:

$$D^*_{0,mesa}(T) = \frac{\mathcal{R}_{0,mesa}\sqrt{\sigma_{mesa}}}{\sqrt{4k_B T/R_0(T) + 4egI_{back,photo}}}, \tag{3.24}$$

where we have considered the effective detector area to be the electrical area of the mesa $A_{det} = \sigma_{mesa}$. From Equation 3.14, we can consider $I_{back,photo} = \mathcal{R}_{0,mesa}\sigma\Phi_{300K}E_{trans}$, assuming the environment to be at room temperature (300K). Now, we can study the two limiting behaviours of the mesa detectivity, i.e. when $T = 0$ K and when $T >> T_{BLIP}$:

$$\begin{aligned} D^*_{0,mesa}(T=0) &= \sqrt{\frac{\mathcal{R}_{0,mesa}}{4egE_{trans}\Phi_{300K}}} && (3.25)\\ D^*_{0,mesa}(T>>T_{BLIP}) &= \mathcal{R}_{0,mesa}\sqrt{\frac{\sigma}{4k_BT/R_{0,mesa}(T)}}. && (3.26)\end{aligned}$$

For an array, we can write analogously:

$$D^*_{0,array}(T) = \frac{\mathcal{R}_{0,array}\sqrt{A_{coll}}}{\sqrt{4k_BT/R_{0,array}(T) + 4egI_{back,photo}}}, \tag{3.27}$$

where we considered $A_{det} = A_{coll}$. In this case, the background photocurrent is $I_{back,photo} = \mathcal{R}_{0,mesa}A_{coll}\Phi_{300K}E_{trans}$ and the two limiting values are

$$\begin{aligned} D^*_{0,array}(T=0) &= \sqrt{\frac{\mathcal{R}_{0,array}}{4egE_{trans}\Phi_{300K}}} && (3.28)\\ D^*_{0,array}(T>>T_{BLIP}) &= \mathcal{R}_{0,array}\sqrt{\frac{A_{coll}}{4k_BT/R_{0,array}(T)}}. && (3.29)\end{aligned}$$

The ratio of the array and mesa detectivities in the low temperature regimes is then:

$$\frac{D^*_{0,array}(T=0)}{D^*_{0,mesa}(T=0)} = \sqrt{\frac{\mathcal{R}_{0,array}}{\mathcal{R}_{0,mesa}}}. \tag{3.30}$$

In order to calculate this ratio in the high temperature regime, we observe that the array (mesa) resistance is inversely proportional to its electrical area σ_{array} (σ_{mesa}). This yields the equation $R_{0,array}/R_{0,mesa} = \sigma_{mesa}/\sigma_{array}$. Thus, the high temperature ratio can be expressed as:

$$\frac{D^*_{0,array}(T>>T_{BLIP})}{D^*_{0,mesa}(T>>T_{BLIP})} = \frac{\mathcal{R}_{0,array}}{\mathcal{R}_{0,mesa}}\sqrt{\frac{A_{coll}}{\sigma_{mesa}}\cdot\frac{\sigma_{mesa}}{\sigma_{array}}} = \frac{\mathcal{R}_{0,array}}{\mathcal{R}_{0,mesa}}\sqrt{\frac{A_{coll}}{\sigma_{array}}} \tag{3.31}$$

Figure 3.8 shows a schematic comparison of the mesa and array detectivity curves as a function of temperature. At low temperatures, where the device is background limited, the ratio of the two detectivities just depends on the ratio of the two corresponding responsivities. Thus, in array QCDs, it is possible to achieve an increase in detectivity thanks to the improved absorption efficiency of a patch cavity over a mesa (*microcavity effect*). In this case, however, there is no advantage related to the higher collection area in the array device. The reason for this is that not only the detectivity, but also the background photon noise increases with the collection area.

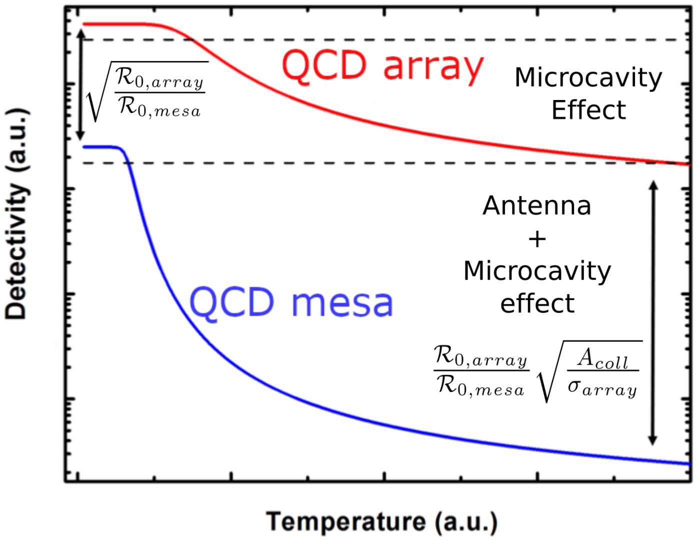

Figure 3.8: Temperature dependence of the QCD specific detectivity in mesa and array geometries. The latter can improve the device performance, especially in the high temperature regime, thanks to a combined microcavity and antenna effect.

At high temperatures, instead, where the device is limited by thermal noise, the effect of the higher collection area is visible and the ratio of the two detectivities does not only depend on the ratio of the responsivities, but also on A_{coll}/σ_{array}. Thus, we can say that an *antenna effect* is added to the microcavity one. As a result, the largest improvement due to the microcavities is observed at high temperatures.

3.2 Electro-optical characterization of a patch-antenna QCD

Up to now, the only patch-antenna ISB detectors that have been reported in the literature are QWIPs [44][45][38][4]. These works confirm the predictions discussed in the previous section. Particularly relevant are the results reported in reference [4] by D. Palaferri and others, who achieved room temperature operation of a 9 µm patch-antenna QWIP.

In this thesis work, we report for the first time a characterization of a QCD in this type of geometry, showing that the microcavities are beneficial for the performance of these types of detector as well.

3.2.1 Sample description

The wafer of the active region described in Section 2.4.1 was processed by Azzurra Bigioli[1] at Paris Diderot University[2] to create the patch array. The device is a matrix of 15x15 square patches (Figure 3.9). On top of each patch is deposited a PdGeTiAu layer, which creates an ohmic contact with the underlying GaAs. All the elements in a single row are connected by a TiAu wire, which is in contact both with the PdGe and with the active region. TiAu creates a Schottky contact with the semiconducting materials and thus ensures that the charge carriers are collected only from the PdGe contact. The wires then reach a common pad, where it is possible to create, via thermal bonding, the electrical contact to perform the measurements. The ground signal is taken from a metallic substrate, common to all patches.

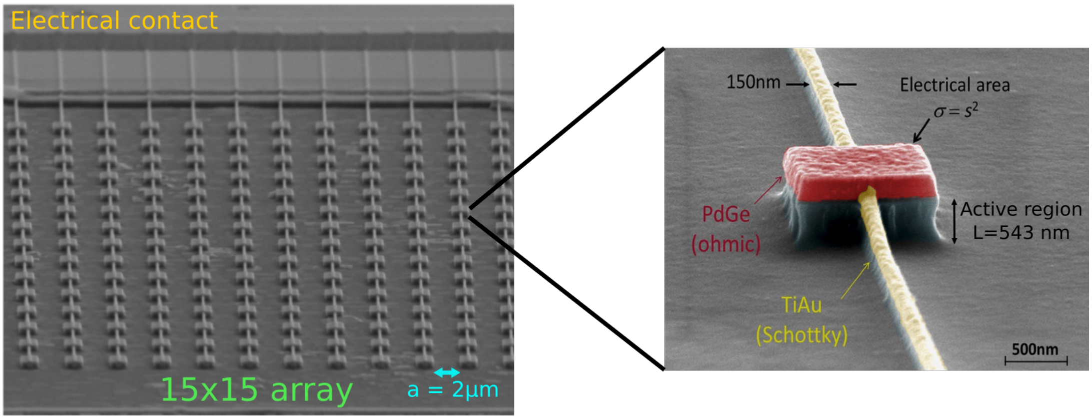

Figure 3.9: Scanning electron microscope images of the patch array (left) and of a single square patch (right).

Samples with four different patch sizes s were produced: 1.15µm, 1.2µm, 1.3µm and 1.4 µm. These values were chosen on the basis of Equation 3.8 and of the simulation reported in Figure 2.8. The optical transition predicted by the simulation has a corresponding wavelength λ_{res} ≈8.9µm. The patch with a resonant wavelength equal to λ_{res} is then expected to have size $s \approx \lambda_{res}/2\mathtt{n}_{eff} \approx 1.35$µm (with $\mathtt{n}_{eff} = 3.3$

---

[1] École Normale Supérieure, 75005 Paris, France.

[2] Université Paris Diderot, 75013 Paris, France.

[39]). Also patch cavities expected to be off-resonance were produced (1.15 and 1.2 µm), in order to study what is their effect on the spectral response of the device.

3.2.2 Spectral Response

The first optical measurements we performed on the devices are photoresponse spectra as a function of the patch size s and of temperature. Figure 3.10 shows the experimental setup we used for these measurements. The sample is placed inside a Janis ST-300 cryostat with ZnSe windows, which are transparent in the spectral range between 7 and 12 µm. The temperature in the cryostat determined by the balance between the flow of liquid nitrogen and the current flowing into a heater wire in the cryostat. The internal temperature is measure by a thermocouple, whose output is sent to a Lakeshore 331 temperature controller. The proportional-integral-derivative (PID) controller in the Lakeshore 331 sets the current flow needed to reach the desired temperature. The whole cryostat is kept under high vacuum (below 10^{-4} mbar) by a turbomolecular pump, to avoid condensation and decrease thermal exchange with the environment.

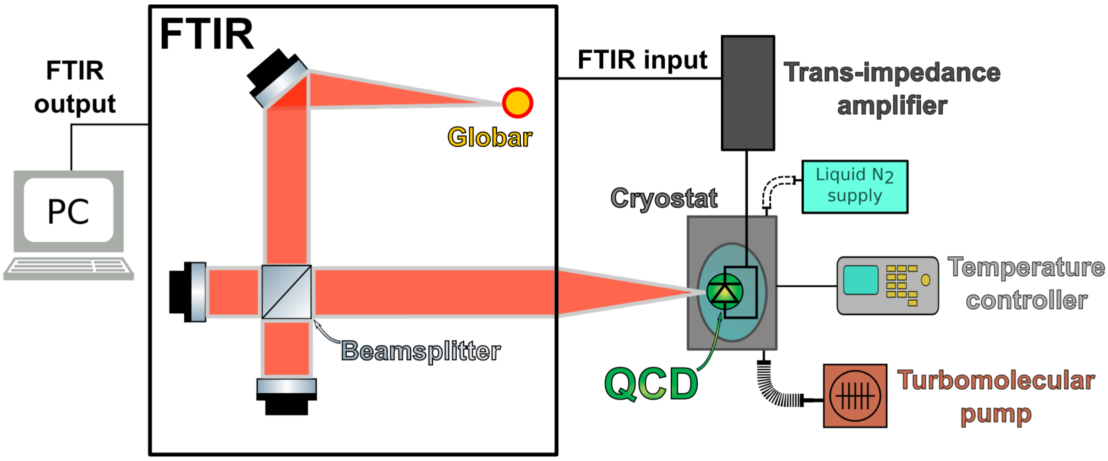

Figure 3.10: Schematic representation of the experimental setup for the measurement of the QCD spectral photoresponse.

We measured the spectral response with a Bruker Vertex 70 Fourier transform infrared (FTIR) spectrometer. This instrument has an internal source of polychromatic MIR radiation (called *globar*), which is a blackbody with a temperature of ≈ 1000 K. This beam is reflected by a mirror towards a beamsplitter, i.e. an optical element that partly transmits and partly reflects the radiation, splitting the initial beam in two. The two beams are reflected by two mirrors back to the beamsplitter, where they recombine. Finally, the resulting beam is sent to the output of the instrument and focused onto the sample. The output current from the sample is amplified by a Femto DLPCA-200 transimpedance amplifier and sent to the FTIR itself, which delivers the result to the PC. One of the two mirrors is able to move, creating an optical path difference between the two beams. Thus, this part of the FTIR is essentially a Michelson interferometer. The output signal is measured as a function of the optical path difference and then Fourier transformed to obtain a spectrum as a function of the wavenumber k (with dimensions of an inverse length). From the wavenumber it is possible to obtain the photon wavelength ($\lambda = 1/k$) and energy ($E = hck$). For more details on how an FTIR spectrometer works we refer the interested readers to [47] and [48]. Typically, several mirror scans are performed to measure as many spectra, which are then averaged together in order to reduce the noise.

Finding the resonant patch size

First we acquired the spectral response of the four samples with different patch sizes at liquid nitrogen temperature (~78K) and without an external bias. The goal is to identify at which patch size the resonance energy of the microcavity is the same as the energy of active transition in the QCD. In order to compare correctly the four spectra, we performed the measurements under the same experimental conditions (aperture in the globar source, number of scans, spectral resolution, amplifier gain). The result of the measurement is shown in Figure 3.11. We normalized to 1 the curve with the highest peak and scaled the other spectra accordingly.

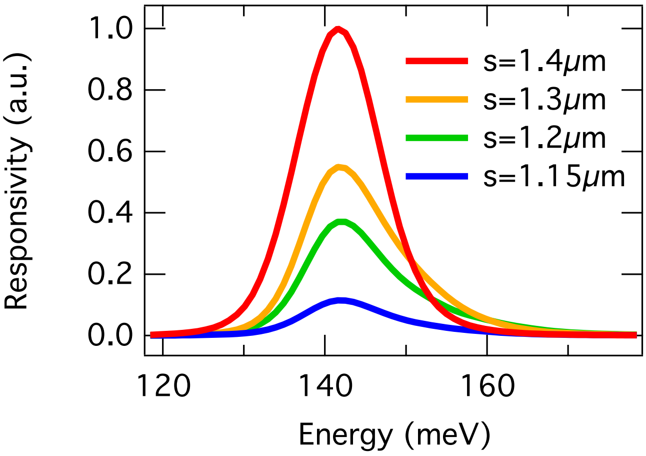

Figure 3.11: Photoresponse spectra at T =78K and without applied bias of four patch-antenna QCDs with different patch sizes. In the sample with s = 1.4μm the microcavity resonates with the optical transition of the QCD, generating a symmetric and more intense signal.

These data show how strong can be the effect of the cavity on the device response: a change in s of few hundreds of nanometers causes remarkable changes in the output signal. These spectra allowed us to state that resonant patch size is s = 1.4μm. Indeed, the corresponding spectrum has substantially higher intensity than the others. For example, its peak response is 10 times higher than the s = 1.15μm sample.

Another indicator of the resonance between cavity and QCD is the shape of the spectra. The s = 1.4μm has a symmetric shape, while all the others display broadening at high energies. This effect is directly related to the presence of the microcavity. Indeed, these spectra are a combination of two responses: one due to the ISB transition in the QCD $R_{ISB}(E)$, which is the same in all samples, and one due to the microcavity absorption $R_{cavity}(E)$, which depends on s. In particular, due to Equation 3.8, a lower s implies a higher resonance energy of the cavity and thus an absorption peak at higher energies, for a given quality factor of the cavity Q. Figure 3.12 shows a simplified model to understand the effect of the cavity on the QCD spectrum. On the left, the black curve represents R_{ISB}, with a peak at 140 meV, while the red and blue dashed lines represent R_{cavity} for two different resonance energies of the cavity, one at 150 meV (blue curve) and one at 140 meV (red curve), which is in resonance with R_{ISB}. If we approximate the resulting spectrum of a patch QCD with the product of the two spectral responses $R_{ISB} \times R_{cavity}$, we obtain the two spectra reported on the right. In the case where the cavity absorption does not resonate with the ISB absorption, the spectrum has a lower intensity and shows a broadening at higher energies. Instead, when cavity and ISB absorption resonate, the resulting spectrum has a higher intensity and it is symmetric.

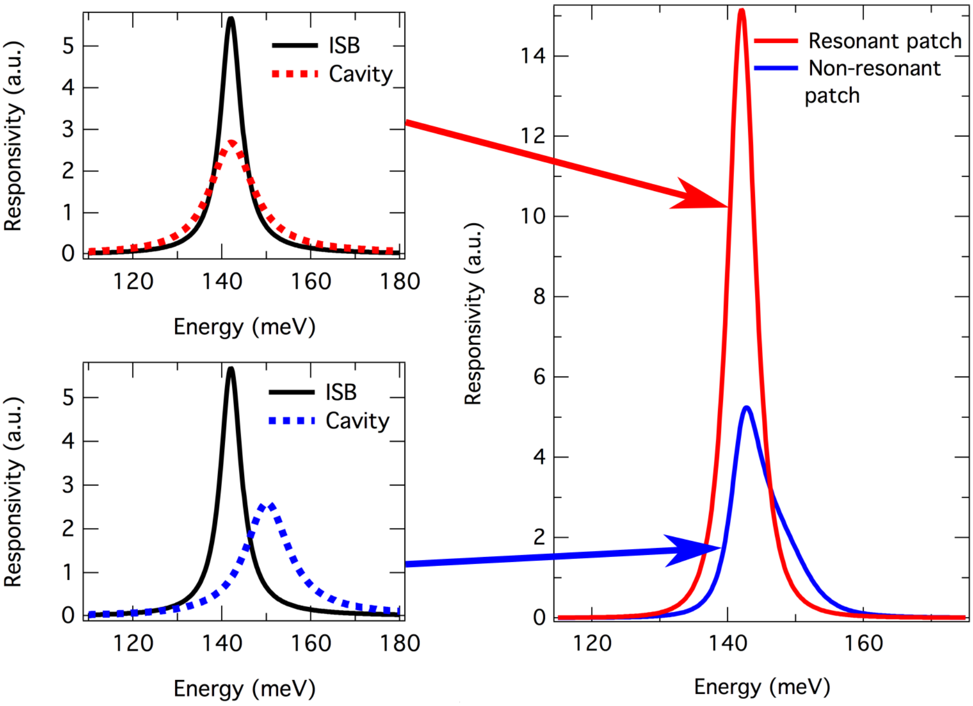

Figure 3.12: Effect of the microcavity on the absorption spectrum of a QCD. If the cavity absorption energy corresponds to the ISB absorption energy, the intensity is maximized and the resulting spectrum is symmetric.

Through these measurements we were able to find the device with resonant patch size ($s = 1.4$µm) and thus we carried out the whole characterization only on this detector. Therefore, all the experimental results reported in the following concern this device.

High temperature performance

For practical applications, it is relevant to study how the detector temperature affects the spectral response. We measured the spectral response with an applied bias of 0V and at 210, 260 and 295 K temperatures, of interest for Peltier-cooled applications. Figure 3.13a shows the measured spectra, compared with the one measured at liquid nitrogen temperature. Figure 3.13b shows the integral of each spectrum, as a function of the detector temperature.

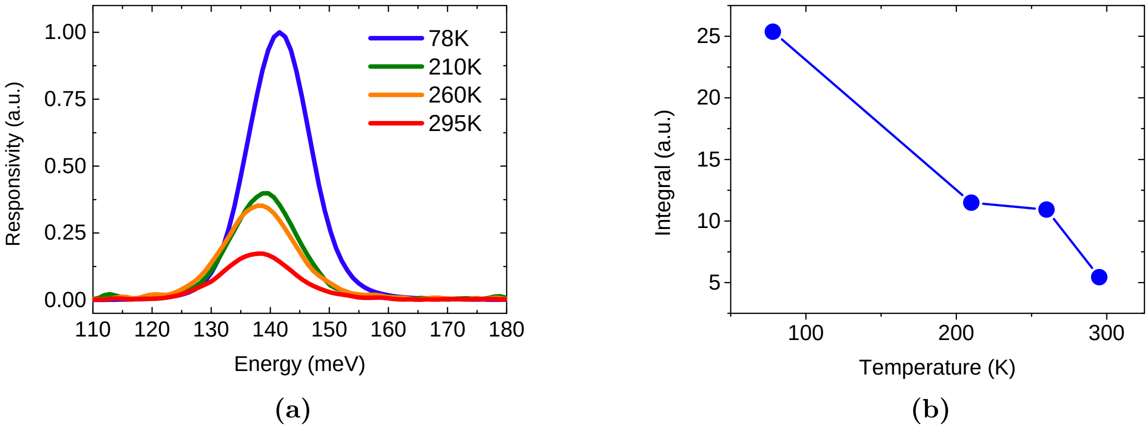

(a) (b)

Figure 3.13: (a) Spectral response at 0 applied bias of the $s = 1.4\mu m$ device at different temperatures of the device. (b) Integral of the four spectra as a function of the device temperature.

The detector achieves room temperature operation, although a drop in intensity occurs as temperature increases. From 78K to 260K we observe a decrease by approximately a factor of two in the integral, which turns to a factor of five at room temperature. The temperature drop of the QCD responsivity is a well known behaviour, reported multiple times in the literature [3][30]. However, the physical mechanism that causes this is still unknown. Indeed, electronic transport should be always confined in the multi-QW structure and charge carriers should not loose their velocity at high temperatures, leading to a temperature-independent responsivity.

We observe a significant decrease in the signal from 260 to 295 K, which is unexpected, especially because from 210 to 260 K a much lower drop is observed. We suggest that this behaviour might not be related to the device itself, but to the limitations imposed by our experimental setup and, in particular, by the transimpedance amplifier. At high temperatures the 0 Volts resistance of the device decreases by more than four orders of magnitude (Figure 2.11), which is not an ideal condition for operating a current amplifier. Indeed, these instruments typically work best with a high impedance input. A possible way to check the validity of this hypothesis would be to let the output current flow though a shunt resistor and then to measure the voltage drop across it with a voltage amplifier. In this case, the device resistance should not affect the output of the measurement.

3.2.3 Background I-V characteristics

The device is said to be in *background* condition if the only external source of radiation is the environment, having a temperature greater than the device temperature. Thus, from Equation 1.10, in this condition the total current is a sum of two contributions: the photocurrent due to the background radiation and the dark current.

The experimental setup for this measurement is the same as for the dark I-V (Figure 2.9), except that the cryo-shield is not used in this case. Instead, the sample is exposed to the environment radiation though the cryostat windows. We performed the measurement for different detector temperatures, from 78K to room temperature. The results are shown in Figure 3.14.

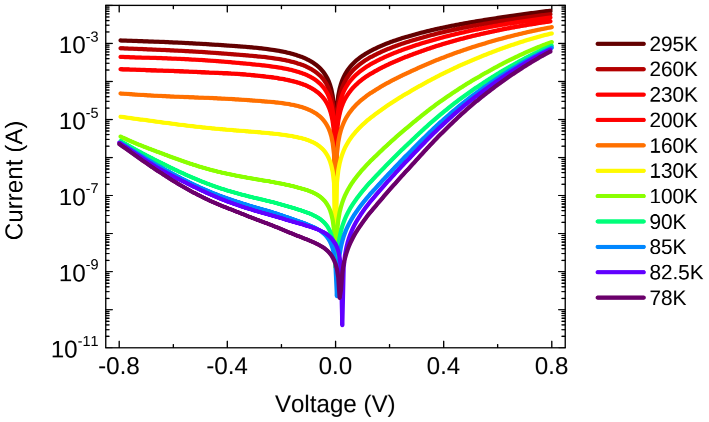

Figure 3.14: Background I-V characteristics of the patch-antenna QCD at different temperatures

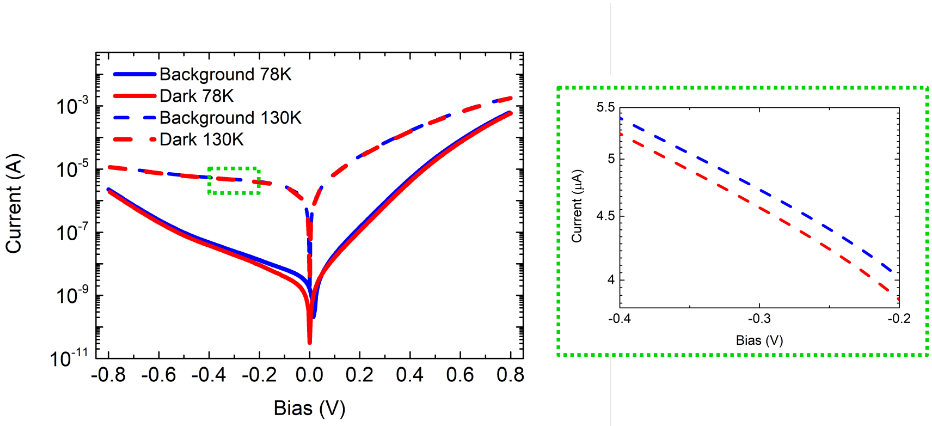

Figure 3.15: Dark and background I-V characteristics of the QCD at temperatures of 78 and 130 K. The graph on the right shows an enlargement of the 130K curves, showing that also in this case we observe a higher background current, due to the photocurrent generated by background radiation.

It is interesting to compare these curves with the dark I-V characteristics reported in the previous chapter (Figure 2.10). In Figure 3.15 we report the dark and background characteristics at two different temperatures: 78 and 130 K. By comparing the two curves at 78K, we can observe that the background current is always higher than the dark one. This is expected from Equation 1.10, indeed the difference between the two is exactly the photocurrent due to the background radiation. Moving to higher temperatures this photocurrent becomes weaker, but it is still present, as shown for 130K temperature in the enlargement on the right of Figure 3.15.

3.2.4 Responsivity

From the definition of responsivity (Equation 1.1) we know that, in order to obtain its value, we need to measure the photocurrent flowing in the device due to an external source and the incident power on the detector. In the following we explain the setup and the techniques we used to accomplish these tasks, along with the experimental results.

Power calibration

The incident power on a detector P_{in} can be calculated as the energy integral of the product of the power emitted by the source $P_e(E)$ with the detector responsivity normalized to 1, $\mathcal{R}_n(E) = \mathcal{R}(E)/\mathcal{R}_{max}$:

$$P_{in} = \int P_e(E)\mathcal{R}_n(E)\mathrm{d}E. \tag{3.32}$$

The emitted power can be also written as:

$$P_e(E) = \Omega A_{det} I(E), \tag{3.33}$$

where Ω is the solid angle seen by the detector, A_{det} is the light collection area and $I(E)$ is the emitted irradiance. In our case, the source of radiation is a Stanford Research Systems SR830 blackbody at temperature $T = 1000°\mathrm{C}$. The irradiance is then given by Planck's law for blackbody radiation:

$$I(E) = \frac{2\pi}{\hbar^3 c^2}\frac{E^3}{e^{E/k_B T} - 1}, \quad T = 1000°\mathrm{C}. \tag{3.34}$$

It is convenient to express the irradiance as its peak value I_{max} times the normalized irradiance curve $I_n(E)$. Therefore, Equation 3.32 can be rewritten as:

$$P_{in} = \Omega A_{det} I_{max} \Sigma_{det}, \quad \Sigma_{det} = \int I_n(E)\mathcal{R}_n(E)\mathrm{d}E, \tag{3.35}$$

where Σ_{det} represents an overlap integral between the emitted irradiance and the detector responsivity. Since the value of I_{max} is unknown, we cannot use directly Equation 3.35 to calculate the incident power on the QCD. Therefore, we performed a power calibration using an Teledyne Judson MCT (model J15D22), with a responsivity curve $\mathcal{R}_{MCT}(E)$ provided by the manufacturer. If the MCT and the QCD collect the blackbody radiation from the same solid angle Ω, then we have that:

$$P_{in,QCD} = \frac{A_{QCD}\Sigma_{QCD}}{A_{MCT}\Sigma_{MCT}} P_{in,MCT}. \tag{3.36}$$

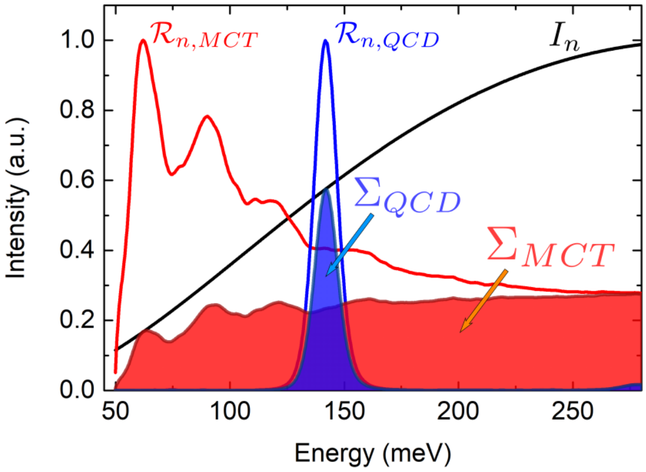

Figure 3.16: Graphic result of the calculation of the overlap integrals Σ_{MCT} and Σ_{QCD} on the basis of Equation 3.35. The red and blue lines are the normalized responsivities of MCT and QCD, respectively. The black line is the normalized blackbody radiation at $T = 1000°\text{C}$.

I_{max} is the same for both detectors, because it just depends on the source, so it is simplified in the equation and it is not needed anymore. Therefore, we can extract the incident power on the QCD knowing the incident power on the MCT detector. Figure 3.16 shows the graphic result of the calculation of Σ_{MCT} (red area) and Σ_{QCD} (blue area). The red and blue lines are the normalized MCT and QCD responsivities, respectively. The MCT curve was provided by the manufacturer. As QCD responsivity curve we took the spectrum at 78K and 0V bias. The black line is the normalized 1000°C blackbody irradiance predicted by Equation 3.34.

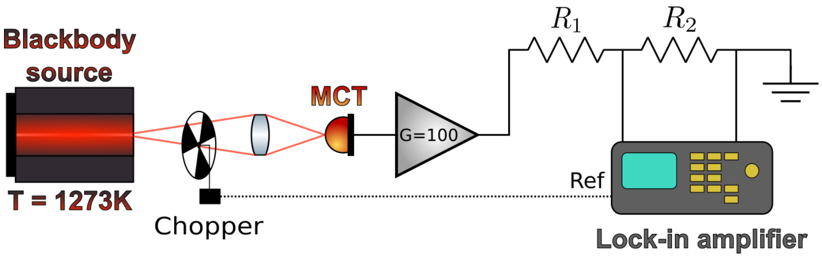

Figure 3.17: Experimental setup for the measurement of the incident power on the MCT detector.

Figure 3.17 shows a schematic representation of the experimental setup we used to measure the incident power on the MCT detector. The 1000°C blackbody radiation is produced by a Boston Electronics IR-564/301 source and it is focused on the MCT detector. The output signal V_{MCT} is then amplified with a gain $G = 100$. In order to avoid the influence of the blackbody radiation from the environment (at 25°C), we placed an optical chopper in front of the source, spinning at a frequency sent by a controller to the reference input of a lock-in amplifier. Because the output from the amplifier overcomes the maximum input voltage accepted by the lock-in, we added a voltage divider to the circuit, with two resistances $R_1 = 10\text{k}\Omega$ and $R_2 = 1\text{M}\Omega$. The lock-in amplifier measures the voltage $V_{lock-in}$ across R_2.

It is straightforward to show that the value of V_{MCT} can be extracted from the measured $V_{lock-in}$ through the formula:

$$V_{MCT} = \frac{1}{G} \times \frac{R_1 + R_2}{R_2} \times \frac{\pi}{\sqrt{2}} V_{lock-in}, \tag{3.37}$$

where the factor $\pi/\sqrt{2}$ is introduced because the lock-in amplifier measures the root mean square value of the voltage oscillation, caused by the presence of the chopper. The incident power on the MCT detector is then

$$P_{in,MCT}(E) = \frac{V_{MCT}}{\mathcal{R}_{MCT}(E)}. \tag{3.38}$$

In our case, we are interested in the incident power at the energy corresponding to the peak of the QCD responsivity ($E = 141.5\text{meV}$), since the detector responds only in a narrow band around that value. Calculating $P_{in,MCT}(141.5\text{meV})$,we obtained an incident power on the QCD of

$$P_{in,QCD} = 90\text{nW}.$$

Photocurrent measurements

Figure 3.18 shows the experimental setup used for the measurement of the photocurrent as a function of the bias applied to the device. As for the previous measurements, the device is put in a cryostat cooled by a liquid nitrogen supply. The source is the same blackbody at $T = 1000°\text{C}$ used for the incident power measurement. Also in this case, an optical chopper is put in front of the source and connected to the reference input of the lock-in amplifier in order to measure only the signal due to the source and not the one coming from the background. The total current I flows into a shunt resistor with resistance $R_{shunt} = 220\Omega$, creating a voltage drop

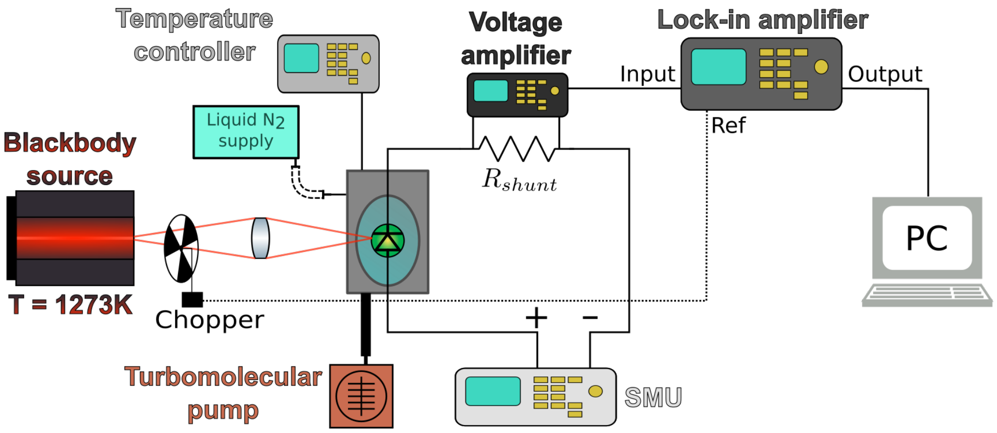

Figure 3.18: Schematic diagram of the experimental setup used for the photocurrent measurement.

$V_{lock-in}$ across it. This voltage is amplified by a Stanford Research Systems SR560 Voltage Amplifier with gain $G = 10^4$ and then sent to the input of the lock-in amplifier. The circuit is biased through the Keithley 2400 source measure unit (SMU). A LabVIEW program on the PC controls the bias applied by the SMU and acquires the output signal from the lock-in and the current I, measured by the SMU.

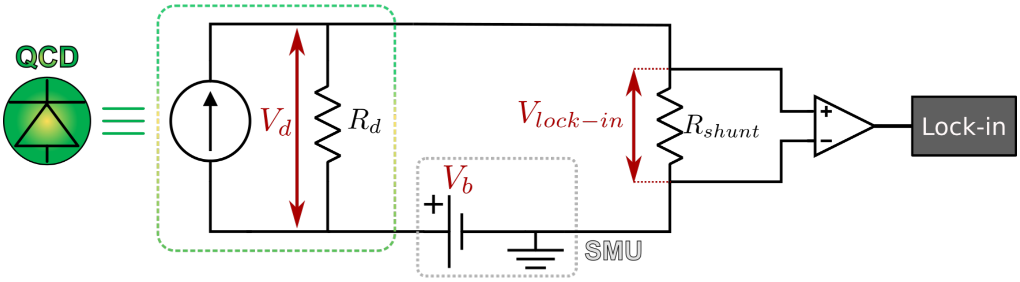

Figure 3.19: Equivalent circuit of the setup in Figure 3.18.

Figure 3.19 shows the equivalent circuit of the setup in Figure 3.18. The QCD can be modeled as a current source in parallel with the device resistance R_d. The current source models the generation of (i) the photocurrent due to the blackbody I_{photo}, (ii) the background photocurrent $I_{back,photo}$ and (iii) the dark current I_{dark}. Our interest is to measure I_{photo} as a function of the bias applied to the device V_d. I_{photo} is separated from the other two contributions thanks to the optical chopper and the lock-in amplifier. V_d does not correspond to the total bias applied by the SMU V_b, due to the presence of R_{shunt}. Solving the equivalent circuit using Thévenin's theorem it is possible to obtain the following expression for V_d:

$$V_d = \frac{R_d}{R_d + R_{shunt}}(V_b - R_{shunt}I). \tag{3.39}$$

Therefore, in order to calculate V_d, also I and R_d are needed. The former is measured directly by the SMU and acquired by the LabVIEW program. The latter is calculated from an I-V characteristic, acquired after the photocurrent measurement, under blackbody illumination. From the I-V the resistance of the device is easily obtained through $R_d = (\mathrm{d}I/\mathrm{d}V)^{-1}$. It is necessary to measure separately the I-V characteristic, otherwise the presence of R_{shunt} would influence the result. Once obtained the photocurrent, it is possible to calculate the responsivity dividing I_{photo} by the incident power on the detector P_{in}, measured at the previous stage.

Figure 3.20b shows the resulting experimental curves of the responsivity as a function of the bias applied to the device. We measured these curves at different temperatures, from liquid nitrogen temperature to room temperature. Figure 3.20a shows the same curves measured on the mesa reference device. In this case the measurements were performed from liquid helium temperature (4K) to 210K. For practical reasons we report only those above 78K.

Figure 3.22 compares the responsivity at -0.1V of the mesa and patch devices as a function of temperature. A boost in the responsivity due to the microcavity effect is clearly visible in the patch detector with respect to the mesa. At liquid nitrogen temperature the responsivity of the former is six times larger than that of the latter. At 210 K the the enhancement is even larger, by a factor of 10. At room temperature and -0.1V, we report a responsivity of 65.7 mA/W, which is significantly higher than the highest value reported in the literature for QCDs in the 9µm spectral range, i.e. 16.9 mA/W [30].

3.2.5 Detectivity

Following Equation 1.9, we calculated the specific detectivity of the device from its responsivity. We obtained the generation-recombination noise using the background I-V characteristics discussed in Section 3.2.3. We calculated the Johnson noise using the resistance calculated from the same I-V characteristics. We considered a detector area equal to the collection area A_{coll} of the microcavities, i.e. the unit cell area $\Sigma = (s + a)^2$ multiplied by the number of elements of the array, 125, times the contrast measured in the reflectivity spectra measure in the reflectivity spectra $C = 0.8$. We repeated the same calculations also for the mesa reference in order to compare the performance of the two geometries. In this case we considered the detector area to be the electrical area $\sigma$of the mesa detector.

Figure 3.21 shows the results for (a) the mesa and (b) the patch array geometries. A higher specific detectivity is observed at every temperature in the patch device, with respect to the mesa.

Figure 3.23 shows the comparison of the mesa and patch detectivities as a function of temperature, for a fixed voltage of -0.1V. As expected from the theory of patch-antenna detectors (Section 3.1.3), we observe the most relevant boost in detectivity at high temperatures, thanks to both the microcavity and antenna effects. At liquid nitrogen temperature the patch D^* is greater than the mesa one by a factor of ~5.5, which is in agreement with the value of 6.1 predicted by Equation 3.30, calculated using the experimental values of the two responsivities at this temperature. At 200K this factor becomes ~16.3, close to the value of 13.7 predicted by Equation 3.31. We also note that at room temperature the patch detector has a detectivity comparable to the one at 170K of the mesa. Therefore, thanks to the patch antenna architecture, in the high temperature range, we were able to achieve a 130K increase in the operating temperature, keeping the same detector performance as in the mesa device.

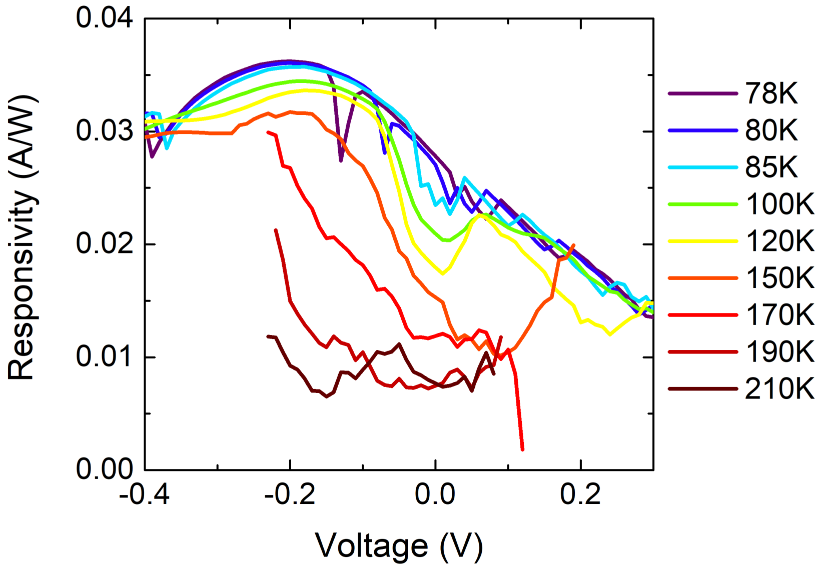

(a)

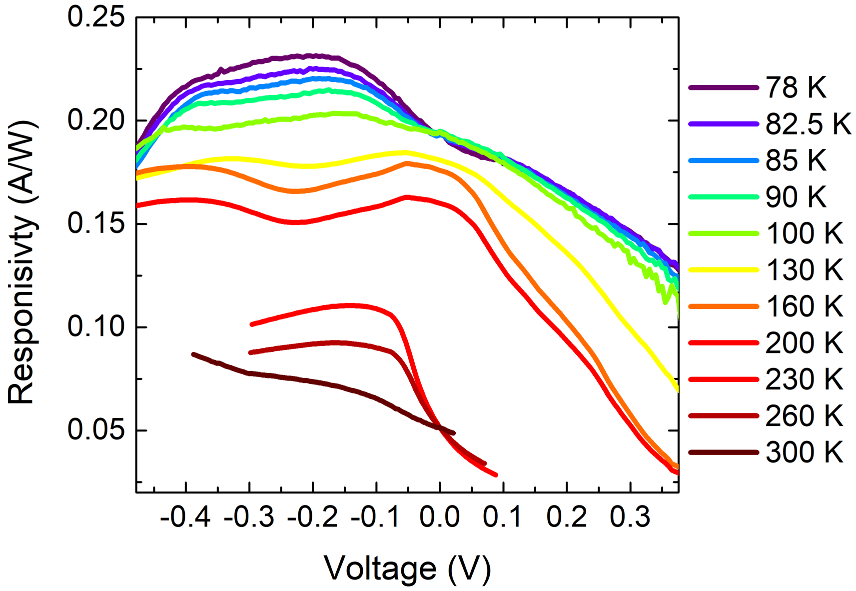

(b)

Figure 3.20: Responsivity as a function of the bias applied to the device for (a) the reference mesa and (b) the patch-array device.

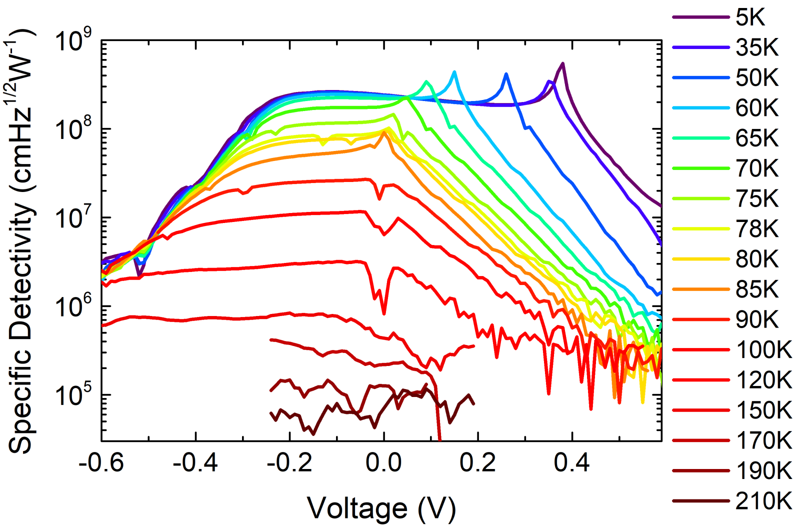

(a)

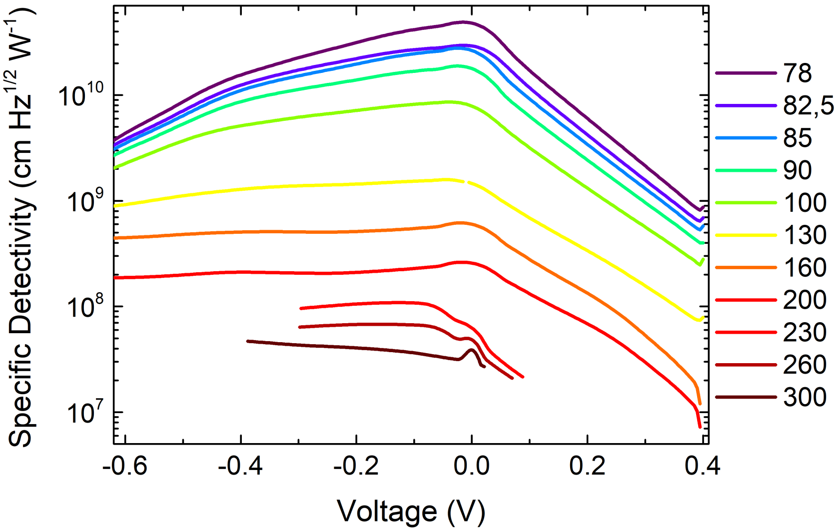

(b)

Figure 3.21: Specific detectivity as a function of the bias applied to the device for (a) the reference mesa and (b) the patch-array device.

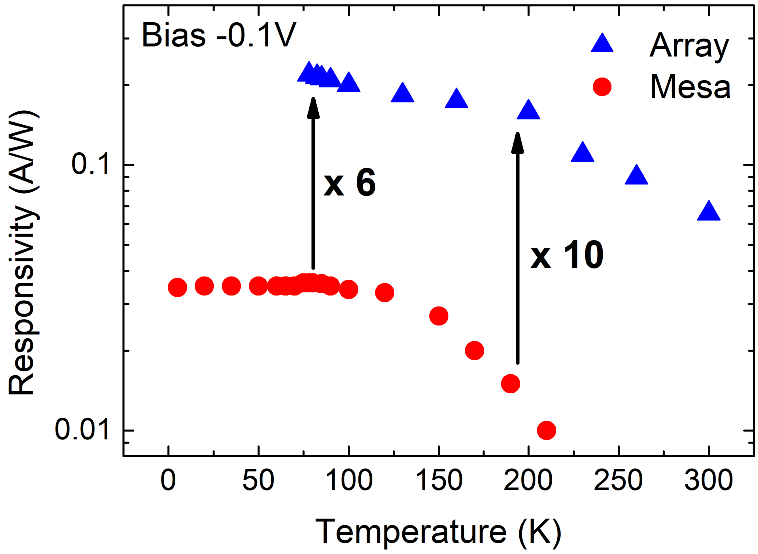

Figure 3.22: Comparison of the mesa (red dots) and patch-array (blue triangles) responsivity at -0.1V as a function of temperature. We report a responsivity enhancement by a factor of 6 at low temperature and by a factor of 10 at 200K.

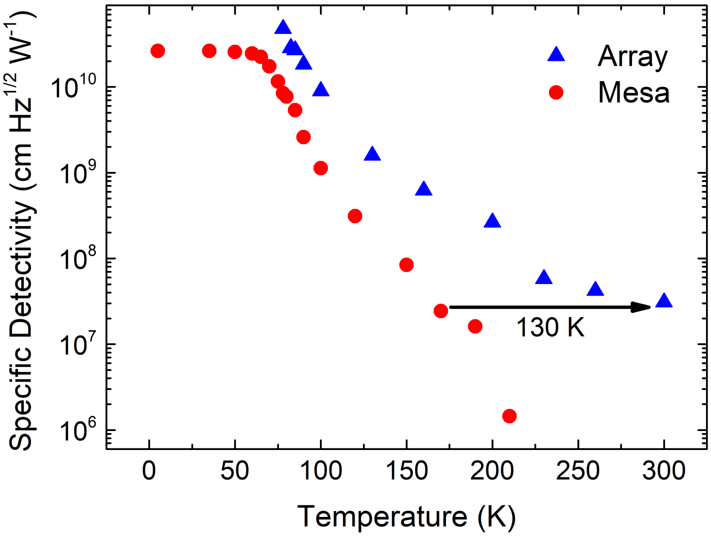

Figure 3.23: Comparison of the mesa (red dots) and patch-array (blue triangles) detectivity at -0.1V as a function of temperature. At room temperature our array QCD displays the same performance as the mesa reference at 170K.

Chapter 4

Design of a new QCD generation

In this chapter, we focus our attention on computer simulations for the design of the QCD active region. First, we briefly recall the theory needed to simulate the band structure of multi-QW systems, such as QCDs. Then, we report our work concerning the design of a patch-antenna QCD operating at a 4µm wavelength. As we shall see, a device of this kind introduces some challenges that we were able to overcome by introducing a new type of QCD, that we refer to as *step-well QCD*. We explain the modifications implemented in the Schrödinger-Poisson solver in order to simulate such structure and we finally report the results of the simulations.

4.1 Simulating the QCD active region

The production process of a QCD (and of any other ISB device) can be divided into three main steps:

1. *Simulation*: A computer program is used to simulate the band structure of the device. Parameters such as the materials used in wells and barriers, the QWs height and the QWs width are changed, as a function of the operating wavelength and desired performance, until the desired result is achieved.
2. *Growth*: The heterostructure designed during step 1 is produced by epitaxial growth and then the device is processed. This part is performed in clean room.
3. *Characterization*: Measurements are carried out on the final device to assess its electrical and optical properties.

Figure 4.1 shows some of the most important parameters that have to be optimized during the design of a new QCD. The first one is the transition energy E_{trans} in the active well. Its value determines the spectral region where the detector operates and it is chosen on the basis of the particular applications the QCD is made for. The value of E_{trans} influences the choice of the materials for wells and barriers, which have to provide a conduction band offset (CBO) larger than the transition energy itself. Also the energy difference between adjacent levels of the cascade E_{ij}, with $j = i + 1$, has to be optimized. Indeed, as discussed in Section 2.2, E_{ij} should be close to the LO phonon energy in order to create a faster and more efficient transport along the cascade.

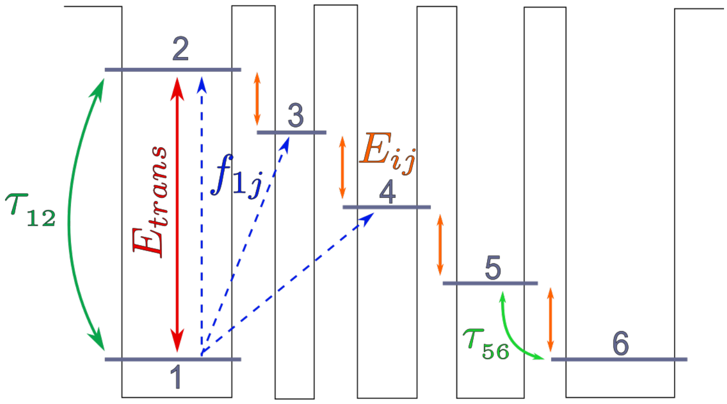

Figure 4.1: Schematic representation of some of the key parameters to be optimized during the QCD design.

Other important parameters are the relaxation times τ_{ij} between the energy levels in the structure (labeled by i and j). The relaxation time of the active transition (τ_{12} in the case of Figure 4.1) should be higher than the extraction time to the cascade region, otherwise most part of the photo-excited electrons would de-excite back to the ground state, instead of giving their contribution to the photocurrent. Also the relaxation time between the last level of the cascade region and the ground state of the following period (τ_{56}) has to be optimized. Its value should be minimized, in order to avoid accumulation of charge carriers in level 5, which would slow down the transport in the structure and also create, between levels 5 and 1, a capacitive effect, detrimental for high speed applications.

The oscillator strength f_{ij} between different levels is another key parameter in the design of the active region. In particular, it is important that the oscillator strength of the active transition f_{12} is as close as possible to unity, to ensure that most part of electrons in the ground state are excited to level 2 and do not take part in diagonal transitions.

It is therefore necessary to have a computer program that is able to simulate the electronic eigenfunctions for a given potential and also to calculate the scattering times and oscillator strengths between energy levels. In the following, we briefly cover the theory that is needed to perform these calculations and we explain the working principle of the program for the simulations used during this thesis work.

4.1.1 Band structure calculation in multi-QW systems

As already discussed in Section 2.1, inside a crystalline solid the electronic eigenstates can be calculated solving the time-independent Schrödinger equation:

$$\left[\frac{\mathbf{p}^2}{2m} + V(\mathbf{r})\right]\psi(\mathbf{r}) = E\psi(\mathbf{r}), \tag{4.1}$$

where m is the electron mass and $V(\mathbf{r})$ is a potential with the same periodicity as the crystal lattice: $V(\mathbf{r}) = V(\mathbf{r}+\mathbf{R})$, with $\mathbf{R}$ the lattice constant. Bloch's theorem states that the eigenfunctions that solve Equation 4.1 are in the form [49]:

$$\psi_{\nu\mathbf{k}}(\mathbf{r}) = \frac{e^{i\mathbf{k}\cdot\mathbf{r}}}{\sqrt{V}} u_{\nu\mathbf{k}}(\mathbf{r}), \tag{4.2}$$

where V is the unit cell volume, ν is the band index and $u_{n\mathbf{k}}(\mathbf{r})$ is a period function such that $u_{\nu\mathbf{k}}(\mathbf{r}) = u_{\nu\mathbf{k}}(\mathbf{r}+\mathbf{R})$ and $\hbar\mathbf{k}$ is the *crystal momentum.* By putting Equation 4.2 into 4.1 and using approximations such as the tight binding or the pseudo-potential methods [50] it is possible to obtain the full band structure of the system. However, a description of the band structure just in the vicinity of the conduction and valence band extrema is typically sufficient to correctly predict the electronic and optical properties of the system. For this reason, a very popular method to solve the Schrödinger equation is through the $\mathbf{k}\cdot\mathbf{p}$ approximation, that allows to calculate the band structure in the vicinity of the $\mathbf{k} = \mathbf{0}$ point.

k·p perturbation theory

By inserting Equation 4.2 into 4.1, we obtain a Schrödinger equation for the periodic functions $u_{\nu\mathbf{k}}(\mathbf{r})$:

$$\left(\underbrace{\frac{p^2}{2m} + V(\mathbf{r})}_{H(\mathbf{k}=\mathbf{0})} + \underbrace{\frac{\hbar\mathbf{k}\cdot\mathbf{p}}{m} + \frac{\hbar^2\mathbf{k^2}}{2m}}_{W(\mathbf{k})} \right) u_{\nu\mathbf{k}}(\mathbf{r}) = E_{\nu\mathbf{k}} u_{\nu\mathbf{k}}(\mathbf{r}), \tag{4.3}$$

where we have split the Hamiltonian into two parts: a $\mathbf{k}$-independent part $H(\mathbf{k} = \mathbf{0})$ and a $\mathbf{k}$-dependent part $W(\mathbf{k})$, that we will treat as a perturbation in $\mathbf{k}$. The fundamental idea at the basis of this theory is indeed using $u_{\nu\mathbf{0}}$ as a basis for the expansion of the eigenfunctions and energy eigenvalues at finite $\mathbf{k}$.

Assuming the band structure to have a minimum at energy $E_{n\mathbf{0}}$, it is possible to show that, applying $\mathbf{k}\cdot\mathbf{p}$ perturbation theory, we obtain a parabolic energy dispersion relation close to the Γ point (Figure 4.2) [50]:

$$E_{\nu\mathbf{k}} = E_{n\mathbf{0}} + \frac{\hbar^2\mathbf{k^2}}{2m^*}, \tag{4.4}$$

where m^* is the effective mass, which in $\mathbf{k}\cdot\mathbf{p}$ is expressed as [50]:

$$\frac{1}{m^*} = \frac{1}{m} + \frac{2}{m^2\mathbf{k}^2} \sum_{\nu'\neq\nu} \frac{|\langle u_{\nu\mathbf{0}}|\mathbf{k}\cdot\mathbf{p}|u_{\nu\mathbf{0}}\rangle|^2}{E_{\nu\mathbf{0}} - E_{\nu'\mathbf{0}}}. \tag{4.5}$$

Equation 4.5 shows that the electron mass in a solid differs from the free electron mass because of the coupling between electronic states in different bands, through the $\mathbf{k}\cdot\mathbf{p}$ term. If we consider the only conduction (c) and valence (v) bands, we can write the conduction band energy as:

$$E_{c\mathbf{k}} = E_{c\mathbf{0}} + \frac{\hbar^2\mathbf{k^2}}{2m} + \frac{\hbar^2\mathbf{k^2}}{2m}\frac{|p_{cv}|^2}{E_g} = E_{c\mathbf{0}} + \frac{\hbar^2\mathbf{k^2}}{2m}\left(1 + \frac{E_P}{E_g}\right), \tag{4.6}$$

where $p_{cv} = \langle u_{c\mathbf{0}}|p|u_{v\mathbf{0}}\rangle$ is the isotropic momentum matrix element, E_g is the band gap energy and $E_P = 2|p_{cv}|^2/m$ is the *Kane energy* (≈ 20 eV in III-V semiconductors [52]).

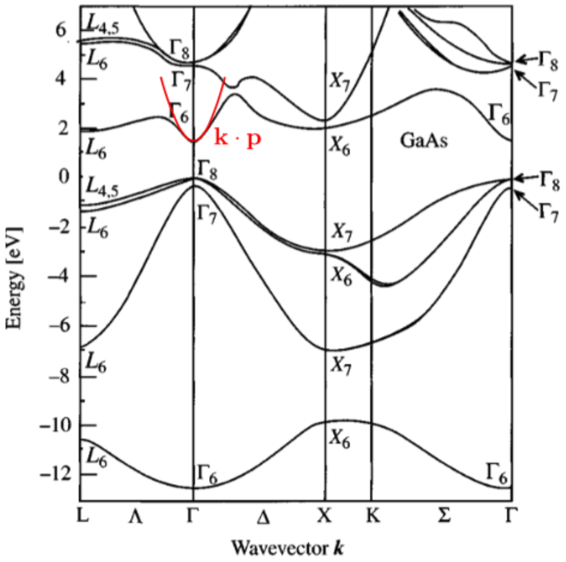

Figure 4.2: Band structure of GaAs (black lines) and result of $\mathbf{k} \cdot \mathbf{p}$ approximation close to the Γ point (red line) (from [51])

Kane model

The parabolic approximation of Equation 4.4, yielded by the $\mathbf{k} \cdot \mathbf{p}$ method, becomes less and less valid for lower values of the effective mass [12]. This is because E_g decreases for a smaller m^*, resulting in a stronger interaction between the conduction and valence bands, which causes larger deviations from the parabolic approximation.

The first model to take into account conduction band non-parabolicity was first proposed in 1957 by E. O. Kane [53] for the case of the InSb band structure. The model considers just the conduction band and three valence bands: heavy holes, light holes and split-off bands(Figure 4.3). The light and heavy holes bands are degenerate in $\mathbf{k} = \mathbf{0}$ and their energy separation with the split-off band is denoted by Δ_{so}. Considering these four bands, the perturbation $W(\mathbf{k})$ can be written as a 8x8 matrix (the factor of 2 is due to the spin). The energy dispersions $E(\mathbf{k})$ are then the eigenvalues of this matrix and one can find that, in this approach, the dispersions are not parabolic anymore. As we shall see later, this non-parabolicity can be taken into account by including an energy dependence in the effective mass: $m^* = m^*(E(\mathbf{k}))$.

Application to QW systems

Our interest is to simulate multi QW structures, therefore we shall see how the Kane model can be optimized for such systems. The heterostructure forming a QW is made by two materials, one with a lower energy gap E_g^W, which produces the well, and one with a higher energy gap E_g^B, forming the barrier. This creates conduction and valence band profiles that vary as a function of the growth direction z: $E_c(z)$ and $E_v(z)$ (Figure 4.4).

In general the two materials in the well and in the barrier display a different values of the effective mass. Therefore, in heterostructures, there is a z-dependence

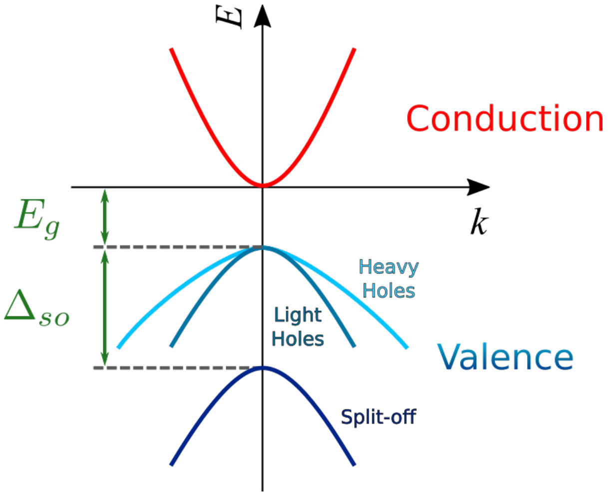

Figure 4.3: Scheme of the band structure considered in the framework of Kane model for a direct III-V semiconductor.

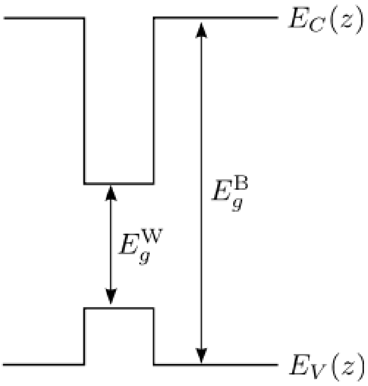

Figure 4.4: Conduction and valence band profiles of a heterostructure. The "W" denotes the well region and the "B" the barrier region.

of the effective mass, in addition to the energy dependence: $m^* = m^*(E, z)$. As discussed in Section 2.1, in these systems it is useful to adopt the envelope function approximation (Equation 2.1). The Schrödinger equation in the confinement direction z for the envelope function $\chi_n(z)$ reads:

$$\left[-\frac{\hbar^2}{2}\frac{\partial}{\partial z}\frac{1}{m^*(E_n, z)}\frac{\partial}{\partial z} + E_c(z) + V_{ext}(z)\right]\chi_n(z) = E_n\chi_n(z), \tag{4.7}$$

where we have introduced an external potential V_{ext}, to consider contributions than are additional to the band discontinuity. In our case, the only external contribution we will consider is a bias applied to the structure, which acts only on the z direction. Along the $x - y$ plane no confinement or external contribution exists, therefore the eigenfunctions and energy eigenvalues are those of free particles.

Following Reference [28], we can reduce the number of bands in the Kane model to three considering the coupling of the conduction band states with the light holes and split-off states. The heavy holes states are decoupled from the original 4x4

Hamiltonian, which becomes the 3x3 matrix:

$$H = \begin{pmatrix} E_c(z) & \sqrt{\frac{2}{3}\frac{p_{cv}}{m}}p_z & -\sqrt{\frac{1}{3}\frac{p_{cv}}{m}}p_z \\ -\sqrt{\frac{2}{3}\frac{p_{cv}}{m}}p_z & E_{lh}(z) & 0 \\ \sqrt{\frac{1}{3}\frac{p_{cv}}{m}}p_z & 0 & E_{so}(z) \end{pmatrix}, \tag{4.8}$$

where lh and so label the the light hole and split-off band edges, respectively. This Hamiltonian acts on a vector of three envelope functions Φ, one for each band:

$$H \begin{pmatrix} \Phi_c \\ \Phi_{lh} \\ \Phi_{so} \end{pmatrix} = E \begin{pmatrix} \Phi_c \\ \Phi_{lh} \\ \Phi_{so} \end{pmatrix}. \tag{4.9}$$

If we are interested only in the energy levels above the conduction band edge (which is the case for QCD simulations), we can solve the problem expressing the equation in the first row as a function of those in the second and third:

$$p_z \frac{2}{m^*(E,z)} p_z \Phi_c + E_c(z)\Phi_c = E\Phi_c, \tag{4.10}$$

where the energy and position dependent effective mass is given by [28]:

$$\frac{1}{m^*(E,z)} = \frac{1}{m}\left[\frac{2}{3}\frac{E_p}{E - E_{lh}(z)} + \frac{1}{3}\frac{E_p}{E - E_{so}(z)}\right]. \tag{4.11}$$

If we adopt the convention of Figure 4.3, setting the conduction band edge energy to zero, the effective mass can be expressed in terms of E_g and Δ_{so}:

$$\frac{1}{m^*(E,z)} = \frac{1}{m}\left[\frac{2}{3}\frac{E_p}{E + E_g(z)} + \frac{1}{3}\frac{E_p}{E + \Delta_{so}(z) + E_g(z)}\right]. \tag{4.12}$$

4.1.2 Calculation of transition parameters

As discussed above, in addition to the band structure of the system, we are also interested in parameters regarding the transitions between two arbitrary states i and j of the structure. In particular, the most relevant ones are the scattering times and the oscillator strengths. In the following we briefly cover how these parameters can be calculated.

Scattering time

For III-V semiconductor multi-QW systems the three most important scattering mechanisms are [54][55]:

1. *Interface roughness*: An elastic scattering mechanism that is due to imperfections at the interface between two different semiconductors. This type of scattering is relevant in the case of multi-QW structures, which display a high density of interfaces.

2. *Alloy disorder*: An elastic scattering mechanism that appears in systems that contain alloys. The disorder inevitably present in alloy compounds introduces inhomogeneities in the periodic potential, which causes electron scattering. It is important to consider this phenomenon in multi-QW structures because it often occurs that they contain alloys such as AlGaAs, InGaAs and others.
3. *LO-phonon emission*: an inelastic scattering mechanism that is typically the most efficient for ISB transitions. Electrons relax to lower energy subbands and part of the lost energies generates longitudinal optical phonons.

Each of these processes has a characteristic scattering rate for a given transition $i \to j$. The total scattering rate can be computed through Matthiessen's rule [23], which states that the total scattering rate is equal to the sum of the scattering rates of the different mechanisms at play:

$$\frac{1}{\tau_{ij}^{tot}} = \frac{1}{\tau_{ij}^{IR}} + \frac{1}{\tau_{ij}^{alloy}} + \frac{1}{\tau_{ij}^{LO}}, \tag{4.13}$$

where "*IR*", "*alloy*" and "*LO*" indicate the interface roughness, alloy disorder and LO-phonon emission mechanisms, respectively. The equations for the calculation of these three scattering rates are reported in Appendix B. In order to calculate these rates it is necessary to fix some parameters that depend on the material choice (e.g. lattice constant, LO-phonon energy, etc.) and to know the wavefunctions of the system, which are obtained by solving the Schrödinger equation.

Oscillator strength

As already discussed in Section 2.2, the oscillator strength of a transition from state i to state j can be expressed as:

$$f_{ij} = \frac{2}{m^* \hbar \omega_{ij}} |\langle \psi_j | p_z | \psi_i \rangle|^2 = \frac{2m^* \omega_{ij}}{\hbar} |\langle \psi_j | z | \psi_i \rangle|^2, \tag{4.14}$$

where $\hbar\omega_{ij}$ is the transition energy. The term $d_{ij} = \langle \psi_j | z | \psi_i \rangle$ is generally referred to as *dipole matrix element* and it is the electric dipole moment associated with the transition between the states i and j. This is also a relevant parameter for active region design because its direction gives the polarization of the transition, determining how the system will interact with an electromagnetic wave of a given polarization.

4.1.3 C++ program for active region simulations

The computer program we used in this thesis work for simulating the QCD active region was developed by Carlo Sirtori, Angela Vasanelli, Giulia Pegolotti and others. It is written in C++ programming language and it is based on a numerical method to solve the Schrödinger equation 4.7 [56][24]. The program finds numerically, point by point, the solutions to this differential equation, allowing to find the solutions for arbitrary potentials, also in the case of a non-zero applied bias.

In the following we report the input file of the program, where we have introduced example values, and a brief explanation of the purpose of each parameter.

```
efield = −0.0001
matchoice = 1
xcont = 0.5
nbwells = 2
Epot = 0.5
T = 300
barriers(1) = 30
wells(1) = 44
multiplier_well(1)=0
multiplier(1)=100
barriers(2) = 62
wells(2) = 12
multiplier_well(2)=25
multiplier(2) = 100,0
```

- `efield` is the value of the electric field applied to the structure, expressed in V/Å.
- `matchoice` can take values from 1 to 5 and each value corresponds to a particular combination of the materials for barrier and wells:
  1. GaAs/AlGaAs
  2. InGaAs/InP
  3. InGaAs/AlGaAs
  4. InAs/AlSb
  5. InGaAs/AlInGaAs

  Once defined the material choice, the following physical parameters are fixed for both the barriers and the wells and saved in specific variables, indicated in parenthesis: m^* (variable `m_b` for barriers and `m_w` for wells), Δ_{so} (`dso_b` and `dso_w`) and E_g (`Eg_b` and `Eg_w`). In the case of *ternary* compounds, these parameters are calculated from the value of `xcont`, following to Vegard's law [22, 23]: $\xi_{\mathrm{A}_x\mathrm{B}_{1-x}\mathrm{C}} = (1-x)\xi_{AC} + x\xi_{BC}$, where ξ is one of the three parameters.
- `xcont` is the percentage x of the material AB (e.g. AlAs) in the ternary alloys in the form $\mathrm{A}_x\mathrm{B}_{1-x}\mathrm{C}$ (e.g. $\mathrm{Al}_x\mathrm{Ga}_{1-x}\mathrm{As}$).
- `nbwells` is the number of QWs in the structure.
- `Epot` is the conduction band offset, that has to be calculated by the user on the basis of the chosen materials.
- `T` is the temperature of the system.
- `barriers(i)` is the width of the `i`-th barrier, expressed in Å.
- `wells(i)` is the width of the `i`-th well, expressed in Å.

- `multiplier_well(i)` can take values from 0 to 100 and it is a percentage value that is used to scale the height of the `i`-th well. The height of the well is calculated through `Epot` × [1 − `multiplier_well`/100].
- `multiplier(i)` has the exact same purpose as `multiplier_well(i)`, but for the barriers. In this case the barrier height is calculated through `Epot` × `multiplier`/100.

The potential of the structure is constructed by repeating the last four terms for each quantum well, with the appropriate input values.

To calculate the band structure of the system, the program solves the Schrödinger Equation 4.7, which contains the z- and energy-dependent effective mass $m^*(E, z)$. A corresponding vector `m_z`, containing the value of the effective mass at each position z is defined in the code. The value of $m^*(E, z)$ is determined by two other z-dependent parameters, $E_g(z)$ and $\Delta_{so}(z)$ (see Equation 4.12), therefore two corresponding vectors `Eg_z` and `dso_z` are defined as well. Let us consider the case of the effective mass, first. At a given position along the growth direction z_i, the program checks whether in that part of the structure a well or a barrier is present. Then, according to the result, `m_z`$[z_i]$ is set equal to either `m_w` or `m_b`. The same procedure is applied to `Eg_z` and `dso_z`.

Once calculated the band structure, the program outputs a text file containing the potential and the square modulus of the wavefunctions $|\psi_i(z)|^2$ as a function of the growth direction z. Some example results are reported in Chapter 2, in Figures 2.8 and 2.14. Once obtained the eigenfunctions, the program calculates for each transition $i \rightarrow j$ the scattering times τ_{ij}^{IR}, τ_{ij}^{alloy}, τ_{ij}^{LO} and τ_{ij}^{tot} (through Equations B.1, B.3, B.5 and 4.13), the oscillator strength f_{ij} and the dipole matrix element d_{ij} (through Equation 4.14).

4.2 New generation of 4µm patch-antenna QCD

In this thesis work, in addition to the characterization of a 9µm patch-antenna QCD, we also started the design of an analogous structure operating at a wavelength of 4µm. In the following, we describe the challenges that such device introduces, from the point of view of both simulations and growth, and what we did to overcome them.

4.2.1 Choice of the structure

In order to have our device operating at a wavelength between 4 and 5 µm, an ISB transition in the active well in the energy range 248 - 310 meV is needed. The use of GaAs in the wells and AlGaAs in the barriers, like in the 9µm QCD discussed in the previous chapters, leads to a conduction band offset (CBO) of 276.32 meV. This value is exactly within the desired transition energy range, which is not ideal for the QCD operation. Indeed, even with a 250 meV transition, electrons in the excited state could be easily excited by thermal energy to the continuum and bypass the cascade region. Therefore, it is necessary to choose another combination of materials to achieve a larger CBO.

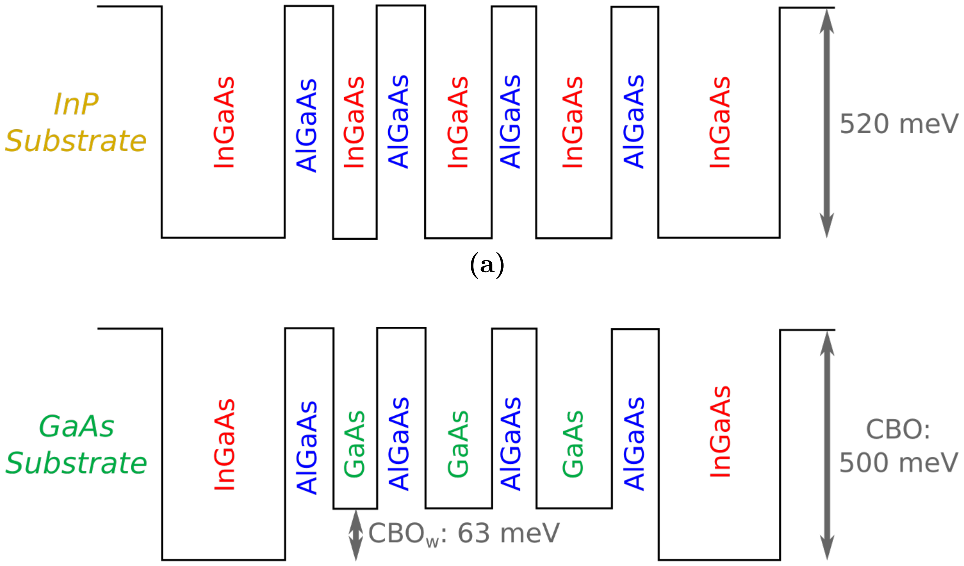

(a)

(b)

Figure 4.5: Schematic conduction band diagram of the two possible geometries for the 4µm patch-antenna QCD: (a) a standard InGaAs / AlGaAs structure and (b) a step well structure, with InGaAs in the active well and GaAs in the cascade region.

One possibility is using $In_xGa_{1-x}As$ in the wells and $Al_yGa_{1-y}As$ in the barriers,grown on a InP substrate (Figure 4.5a). A value of $x = 0.53$ ensures lattice matching to InP and along with $y = 0.45$ generates a CBO of 520 meV. However, the use of an InP substrate could lead to some fabrication problems since the wet-etching of this substrate, necessary to define the patches, generates unwanted residuals products. Therefore, we decided to discard this option.

An alternative to the previous structure is a new geometry, that we will refer to as *step-well* geometry, which has never been applied to QCDs. The idea involves using two different materials to create the QWs, generating wells of different height along the structure, hence the name "step-well". In our case, the $In_xGa_{1-x}As$ / $Al_yGa_{1-y}As$ combination would be used for the active well only. All the remaining structure (i.e. the cascade region) would be made of GaAs / $Al_yGa_{1-y}As$ (Figure 4.5b). In this case the compositions to have a lattice matched structure are $x = 0.1$ and $y = 0.5$, yielding a CBO of 500 meV. In this way, on one hand, the active well has enough CBO to allow a 4µm transition and, on the other hand, it is possible to grow the active region on a GaAs substrate, for which the etching process is well known. For this reason we opted for this geometry, rather than the first one.

4.2.2 Adapting the code for step-well simulations

The step-well geometry solves the problem of etching during growth, but introduces complications in the simulation process. Indeed, The C++ program adopted for the simulations does not provide the possibility of having three different materials in the active region. Therefore, in this thesis work, we introduced some changes in the program, needed to accomplish this task.

The creation of a step-well potential is possible thanks to the `multiplier_well` parameter. One can set the parameter `Epot` equal to the CBO of InGaAs / AlGaAs, i.e. 500 meV, and then scale the wells in the cascade accordingly. In particular, if we denote CBO and CBO$_w$ the conduction band offsets of InGaAs / AlGaAs and InGaAs / GaAs, respectively (see Figure 4.5b), then the correct value of the well multiplier is given by:

$$\texttt{multiplier\_well} = 100 \times \frac{CBO_w}{CBO} = 100 \times \frac{63\text{meV}}{500\text{meV}} = 12.6,$$

where we have reported the calculation for our particular system, where the indium percentage is $x = 0.1$ and therefore the CBO_w results as 63meV.

This allows to create the correct shape of the potential, however it is not enough to perform the simulation correctly. Indeed, it is necessary that the material parameters (i.e. m^*, E_g and Δ_{so}) of InGaAs are associated to the deeper wells and those of GaAs to the shallower ones. Our work was devoted to modify the program to make this possible.

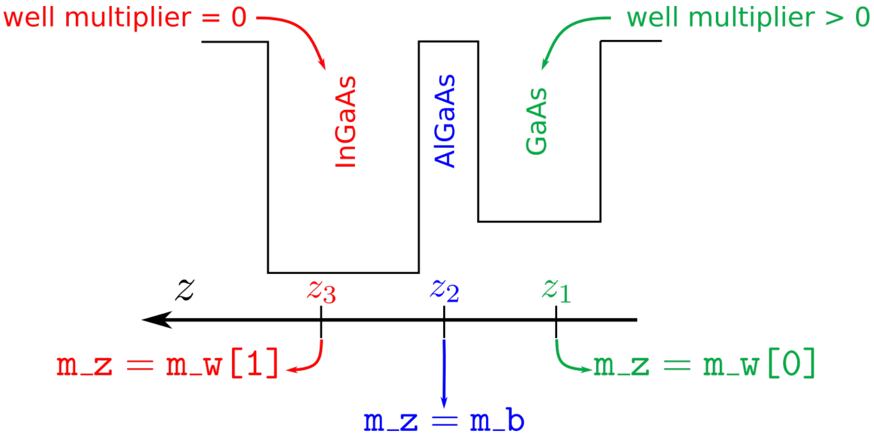

Figure 4.6: Schematic representation of the filling process of the z-dependent effective mass vector `m_z`.

We introduced a sixth material choice in the program: `matchoice = 6`, corresponding to this three-compunds system. Inside the program, we changed the variable containing the effective mass of the well `m_w` to a two dimensional array `m_w[]`, with `m_w[0]` containing the InGaAs effective mass and `m_w[1]` the GaAs one. We did the same for the band gap and split-off energy variables: `Eg_w[2]`, `dso_w[2]`. In order to fill correctly the corresponding z-dependent vector, we added to the code a control on the value of `multiplier_well` for a given well. Let us consider the case of the effective mass. If the `multiplier_well` parameter is equal to zero, then the well is an InGaAs one and `m_z` is set equal to the InGaAs effective mass `m_w[0]`. Instead, if its value is larger than zero, the well is a GaAs one and `m_z` is set equal to the GaAs effective mass `m_w[1]`. Figure 4.6 shows a schematic diagram of this process. The same approach is followed for `Eg_z` and `dso_z`. We left unchanged the process regarding the effective mass in the barriers, because there we have only one type of material.

Approximations and possible improvements

In the process of adapting the code we had to make some approximations.

1. The Kane energy E_p, that appears in the expression for the effective mass $m^*(z, E)$ in Equation 4.12, is not a z-dependent quantity, as opposed to E_g and Δ_{so}. Therefore, we could not apply the same method used for the other three parameters to distinguish between the Kane energy in the InGaAs wells and in the GaAs ones. However, we calculated that the change in E_p between the GaAs and $In_{0.1}Ga_{0.9}As$ case is negligible. Indeed, we calculated that $E_p^{GaAs} = 24.1$eV and $E_p^{InGaAs} = 23.9$eV, a difference of less than 1%. Therefore we set $E_p = E_p^{GaAs}$, since GaAs is more present in the structure than InGaAs. A possible improvement to the code would be to allow the possibility of a band structure calculation with a z-dependent Kane energy.

2. The calculation of the oscillator strength f_{ij} based on Equation 4.14 does not involve a z-dependent effective mass, but just a fixed value of m^*. We calculated the value of f_{ij} in the case of two states of the same QW in a step-well structure, using first the $In_{0.1}Ga_{0.9}As$ and then GaAs effective mass. We obtained values of $f_{ij}^{GaAs} = 0.66$ and $f_{ij}^{InGaAs} = 0.62$, i.e. a difference of 6%, which we consider acceptable. We opted for putting the GaAs effective mass in the calculation. Of course, the ideal solution and a possible improvement would be to include a z-dependent effective mass in the integral of the dipole matrix element $\langle\psi_j|z|\psi_i\rangle$, from which the oscillator strength is calculated.

3. In the calculation of the three scattering times (Equations B.1, B.3 and B.5), it is necessary to specify some material-specific parameters, e.g. Λ and Δ for τ^{IR}, ΔE_c for τ^{alloy} and ω_{LO} for τ^{LO}. Also in this case, the original program does not allow to set two different values of these parameters, one for GaAs and one for InGaAs. As discussed previously, the most important contribution comes from the LO-phonon scattering rate, therefore we can focus on the difference between $\hbar\omega_{LO}$ in the case of GaAs and $In_{0.1}Ga_{0.9}As$. For GaAs its value is 36 meV [3], while for $In_{0.1}Ga_{0.9}As$ it is 35.9 meV [57], a difference of 0.3% that we can neglect. Therefore we opted for putting all of the relaxation times parameters equal to the GaAs ones.

4.3 Results of the simulations

After changing the code to simulate step-well structures, we worked on the design of the new structure. As discussed at the beginning of the chapter, at this stage, one modifies the widths of wells and barriers in order to optimize all the relevant physical parameters, such as position of the levels, scattering times, oscillator strength, etc.

The growth sheet of the final structure is reported in Appendix C. It is an active region with 5 periods of 5 QWs and an active transition of ∼280 meV, corresponding to a wavelength of ∼4.4µm. Figure 4.7 shows the corresponding computer simulation of the band structure of one period, with numbers labeling the different energy states.

In the following, we report the most important transition parameters calculated in the simulation. A complete list of all the parameters can be found in Appendix

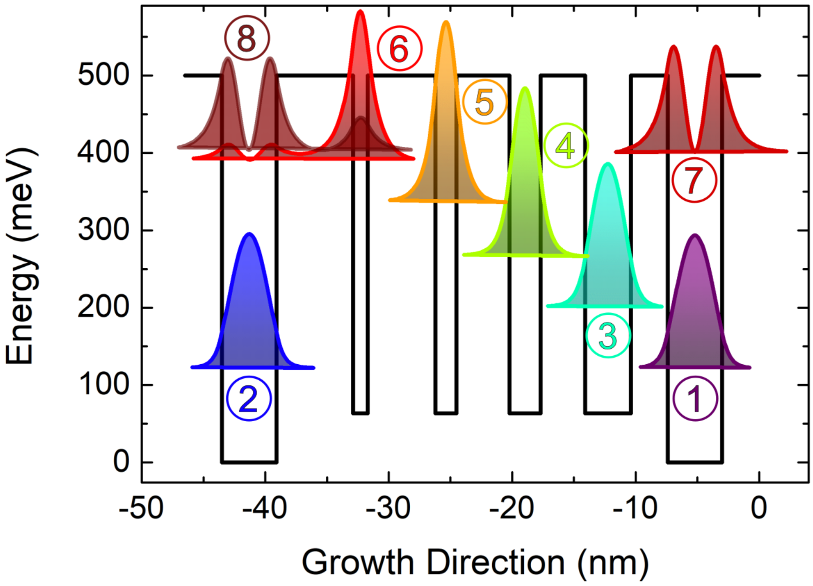

Figure 4.7: Band structure simulation of the 4.4µm step-well QCD designed in this thesis work. Each number labels an energy state in the structure.

D. The scattering times between the ground state of the active well and the two excite states are:

$$\tau_{26}^{tot} = 5.52 \text{ ps}$$
$$\tau_{28}^{tot} = 1.02 \text{ ps},$$

The scattering time between the last level of the cascade and the ground state of the adjacent well is calculated to be:

$$\tau_{31}^{tot} = 6.78 \text{ ps},$$

which is low enough to avoid effects of charge accumulation in level 3 and a corresponding parasitic capacitance.

The sum of the oscillator strengths between the ground state of the active well and the two excited state of the same well is:

$$f_{26} + f_{28} = 0.8,$$

indicating that 80% of the oscillator strength is concentrated in the optical transition.

Conclusions

In this thesis work, we carried out an electrical and optical characterization of a 8.6µm Quantum Cascade Detector (QCD) in a patch-antenna geometry and we simulated and designed an analogous device operating at 4.4µm.

In the first part of this work, we measured the dark current-voltage characteristic of the device as a function of temperature and, applying a simplified model we developed based on references [33] and [34], we extracted the activation energy E_a of the dark current. In order to associate this quantity to the thermally activated electronic transitions in the QCD active region, we performed a simulation of the band structure of the system and we used it to estimate the activation energy. The comparison of the experimental results and the simulations of E_a show an excellent agreement.

The second part of the work was devoted to the optical characterization and performance evaluation of the patch-antenna QCD. We first studied the spectral response of the device for different patch sizes s in order to find for which value of s the microcavity resonates with the active transition in the device. Once found the resonant patch size, we performed photocurrent measurements on the device with a calibrated blackbody source and we measured its responsivity. We repeated the measurement at different temperatures, from 78K to room temperature. By comparing the results with a device having the same active region, but in a standard *mesa* geometry, we observed a responsivity enhancement by a factor of 6 at liquid nitrogen temperature and by a factor of 10 at 200 K. The patch-antenna QCD offers a room temperature responsivity of 50 mA/W at 0V bias, which is significantly higher than the highest value reported in the literature for QCDs in the 9µm spectral range [30]. Finally, we calculated the detectivity of the device and we obtained a room temperature detectivity of $2 \cdot 10^7 \mathrm{cmHz}^{1/2}\ \mathrm{W}^{-1}$, which the mesa device was able to achieve only at 170K, indicating a 130K boost in the temperature performance thanks to the microcavity-antenna affect.

In the last part of this thesis work we designed a patch-antenna QCD operating at 4.4µm. In order to overcome some challenges introduced by the lower wavelength of operation, we proposed for the first time a *step-well* QCD. In this geometry, the quantum well where the optical transition occurs is deeper than the others forming the structure. We introduced some modifications to the program for the QCD active region simulations in order to simulate such structure and we produced the final growth sheet of the device.

This work showed that QCD performance can largely benefit from the properties of double-metal microcavities, especially at room temperature. This, combined with the fast response time of QCDs (in the picosecond range), paves the way to several practical applications for these detectors in molecular spectroscopy, imaging and telecommunications.

Appendices

Appendix A

Growth Sheet of 8.6µm QCD

n^+	GaAs	$5 \times 10^{18}\text{cm}^{-3}$	500Å
i	$\text{Al}_{0.35}\text{Ga}_{0.65}\text{As}$	-	32Å
i	GaAs	-	45Å
i	$\text{Al}_{0.35}\text{Ga}_{0.65}\text{As}$	-	33Å
i	GaAs	-	33Å
i	$\text{Al}_{0.35}\text{Ga}_{0.65}\text{As}$	-	28Å
i	GaAs	-	25Å
i	$\text{Al}_{0.35}\text{Ga}_{0.65}\text{As}$	-	46Å
i	GaAs	-	20Å
i	$\text{Al}_{0.35}\text{Ga}_{0.65}\text{As}$	-	67Å
i	GaAs	-	10Å
n^+	GaAs	$1.25 \times 10^{18}\text{cm}^{-3}$	50Å
i	GaAs	-	10Å
⋮	⋮	⋮	⋮
	↓↓	x8 Periods	↓↓
i	$\text{Al}_{0.35}\text{Ga}_{0.65}\text{As}$	-	32Å
n^+	GaAs	$6 \times 10^{18}\text{cm}^{-3}$	500Å
i	$\text{Al}_{0.35}\text{Ga}_{0.65}\text{As}$		4000Å
Undoped GaAs substrate			

Table A.1: Growth sheet of the 8.6µm QCD characterized in this thesis work. The red lines indicate the active region.

Appendix B

ISB scattering times

B.1 Interface roughness

The interface roughness scattering is due to defects that appear at the interface between two different materials during the growth process. The defect distribution is typically assumed to be gaussian around the interface position [58][59]. The mean height of the roughness is indicated with Δ and the mean distance along z with Λ. The interface roughness scattering rate can be shown to be [55]:

$$\frac{1}{\tau_{ij}^{IR}} = \frac{\pi m_i^*}{\hbar^3}\Lambda^2\Delta^2 \sum_{m,n} F_{ij}^m F_{ij}^n \exp\left(-\frac{\widehat{q}^2\Lambda^2}{4}\right), \tag{B.1}$$

where $\widehat{q}^2 = 2m_j^* E_{ij}/\hbar^2$. F_{ij}^m is the interaction strength at the m-th interface and it is expressed as:

$$F_{ij}^m = -\delta E_c(z_m)\psi_i(z_m)\psi_j(z_m), \quad \delta E_c(z_m) = E_c(z_m^+) - E_c(z_m^-), \tag{B.2}$$

where z_m is the position of the m-th interface.

B.2 Alloy disorder

If a ternary compound of the type $A_xB_{1-x}C$ is present in the system (e.g. $\mathrm{Al}_x\mathrm{Ga}_{1-x}\mathrm{As}$), then the disorder present in such alloys, causes electron scattering [59][60]. The consequent alloy disorder scattering rate can be expressed as [55]:

$$\frac{1}{\tau_{ij}^{alloy}} = \frac{1}{8}\frac{m_i^* a^3 (\Delta E_c)^2 x(1-x)}{\pi\hbar^3}\int_{alloy}\psi_i^2(z)\psi_j^2(z)\mathrm{d}z, \tag{B.3}$$

where a is the alloy lattice constant and ΔE_c is the conduction band offset.

B.3 LO-phonon emission

The LO-phonon scattering is the most efficient relaxation mechanism for ISB transitions. Its scattering rate at temperature $T = 0\mathrm{K}$ is given by [61]:

$$\frac{1}{\tau_{ij}^{LO}(T=0\mathrm{K})} = \frac{m_i^* e^2 \omega_{LO}}{2\hbar^2 \varepsilon_p} \int_0^{2\pi} \frac{I_{ij}(Q)}{Q} \mathrm{d}\theta, \tag{B.4}$$

where

$$\begin{aligned} Q &= \sqrt{k_i^2 + k_j^2 - 2k_i k_j \cos\theta} \\ k_j^2 &= k_i^2 + \frac{2m_i^*}{\hbar}(E_i - E_j - \hbar\omega_{LO}) \\ I_{ij}(Q) &= \int \mathrm{d}z \int \mathrm{d}z' \psi_i(z)\psi_j(z) \exp(-Q|z-z'|)\psi_i(z')\psi_j(z'). \end{aligned}$$

$\hbar\omega_{LO}$ is the LO-phonon energy (that depends on the specific material that is used) and $\varepsilon_p = \frac{4\pi\varepsilon_0}{\varepsilon_\infty^{-1} - \varepsilon_s^{-1}}$, with ε_∞ high frequency and ε_s static electric permittivity. At finite temperature we have to take into account the phonon population, described by the Bose-Einstein statistics. Therefore, the scattering rate for an arbitrary T is obtained through:

$$\frac{1}{\tau_{ij}^{LO}(T)} = \frac{1}{\tau_{ij}^{LO}(T=0\mathrm{K})} \left[1 + \left(\exp\left(\frac{\hbar\omega_{LO}}{k_B T} \right) - 1 \right)^{-1} \right]. \tag{B.5}$$

Appendix C

Growth sheet of 4.4µm step-well QCD

n^+	GaAs	$5 \times 10^{18}\text{cm}^{-3}$	500Å
i	$Al_{0.5}Ga_{0.5}As$	-	30Å
i	GaAs	-	37Å
i	$Al_{0.5}Ga_{0.5}As$	-	36Å
i	GaAs	-	25Å
i	$Al_{0.5}Ga_{0.5}As$	-	43Å
i	GaAs	-	17Å
i	$Al_{0.5}Ga_{0.5}As$	-	55Å
i	GaAs	-	12Å
i	$Al_{0.5}Ga_{0.5}As$	-	62Å
i	$In_{0.1}Ga_{0.9}As$	-	5Å
n^+	$In_{0.1}Ga_{0.9}As$	$2 \times 10^{18}\text{cm}^{-3}$	34Å
i	$In_{0.1}Ga_{0.9}As$	-	5Å
⋮	⋮	⋮	⋮
	$\downarrow\downarrow$	x5 Periods	$\downarrow\downarrow$
Undoped GaAs substrate			

Table C.1: Growth sheet of the 4.4µm step-well QCD designed during this thesis work. The red lines indicate the active region.

Appendix D

Results of simulations

D.1 Scattering times

(i,j)	τ_{ij}^{tot} (ps)	τ_{ij}^{LO} (ps)	τ_{ij}^{IR} (ps)	τ_{ij}^{alloy} (ps)
$(1,2)$	$3.46\cdot10^{11}$	0	$3.46\cdot10^{11}$	$4.18\cdot10^{14}$
$(1,3)$	6.78	13.49	13.76	$1.63\cdot10^{3}$
$(1,4)$	709.70	$1.53\cdot10^{3}$	$1.36\cdot10^{3}$	$5.03\cdot10^{4}$
$(1,5)$	$2.98\cdot10^{4}$	$5.68\cdot10^{4}$	$6.68\cdot10^{4}$	$1.04\cdot10^{6}$
$(1,6)$	$4.56\cdot10^{4}$	$6.95\cdot10^{4}$	$1.46\cdot10^{5}$	$1.45\cdot10^{6}$
$(1,7)$	0.95	1.38	3.41	30.97
$(1,8)$	$8.41\cdot10^{3}$	$1.21\cdot10^{4}$	$3.07\cdot10^{4}$	$2.73\cdot10^{5}$
$(2,3)$	$6.99\cdot10^{11}$	$1.65\cdot10^{12}$	$1.23\cdot10^{12}$	$1.02\cdot10^{14}$
$(2,4)$	$1.68\cdot10^{8}$	$4.14\cdot10^{8}$	$2.93\cdot10^{8}$	$8.81\cdot10^{9}$
$(2,5)$	$3.10\cdot10^{4}$	$6.54\cdot10^{4}$	$6.26\cdot10^{4}$	$1.05\cdot10^{6}$
$(2,6)$	5.52	9.14	15.17	171.98
$(2,7)$	$6.41\cdot10^{3}$	$1.00\cdot10^{4}$	$1.94\cdot10^{4}$	$2.00\cdot10^{5}$
$(2,8)$	1.02	1.59	3.16	31.75
$(3,4)$	2.47	6.97	3.85	663.68
$(3,5)$	343.92	889.23	576.46	$2.07\cdot10^{4}$
$(3,6)$	$2.26\cdot10^{4}$	$5.27\cdot10^{4}$	$4.22\cdot10^{4}$	$6.02\cdot10^{5}$
$(3,7)$	6.97	14.99	14.04	183.36
$(3,8)$	$9.44\cdot10^{4}$	$1.46\cdot10^{5}$	$3.00\cdot10^{5}$	$2.35\cdot10^{6}$
$(4,5)$	1.21	6.00	1.53	276.11
$(4,6)$	205.68	740.13	291.35	$1.27\cdot10^{4}$
$(4,7)$	93.40	268.00	149.07	$3.74\cdot10^{3}$
$(4,8)$	$1.30\cdot10^{3}$	$4.13\cdot10^{3}$	$1.95\cdot10^{3}$	$6.34\cdot10^{4}$
$(5,6)$	0.58	4.85	0.66	181.97
$(5,7)$	360.77	$1.77\cdot10^{3}$	456.34	$6.59\cdot10^{4}$

(i,j)	τ_{ij}^{tot} (ps)	τ_{ij}^{LO} (ps)	τ_{ij}^{IR} (ps)	τ_{ij}^{alloy} (ps)
$(5,8)$	3.76	30.71	4.30	865.83
$(6,7)$	408.84	0	409.74	$1.87{\cdot}10^{5}$
$(6,8)$	0.02	0	0.02	17.53
$(7,8)$	60.40	0	60.49	$3.86{\cdot}10^{4}$

Table D.1: Scattering times of the 4.4μm structure designed in this thesis work, calculated for any combination of energy levels $(i,\ j)$. The values of i and j refer to the labels in Figure 4.7. The scattering times between levels whose separation is less than the LO-phonon energy $\hbar\omega_{LO}$ are set equal to 0.

D.2 Transition parameters

(i,j)	d_{ij} (Å)	f_{ij}	E_{ij} (meV)
$(1,2)$	$1.86{\cdot}10^{-4}$	$2.10{\cdot}10^{-13}$	0.34
$(1,3)$	5.35	0.04	79.35
$(1,4)$	0.37	$3.48{\cdot}10^{-4}$	145.23
$(1,5)$	0.06	$1.57{\cdot}10^{-5}$	214.73
$(1,6)$	0.06	$1.56{\cdot}10^{-5}$	269.57
$(1,7)$	12.26	0.74	279.57
$(1,8)$	0.13	$8.44{\cdot}10^{-5}$	281.67
$(2,3)$	$3.11{\cdot}10^{-5}$	$1.35{\cdot}10^{-12}$	79.00
$(2,4)$	$-1.52{\cdot}10^{-3}$	$5.89{\cdot}10^{-9}$	144.88
$(2,5)$	0.09	$3.00{\cdot}10^{-5}$	214.38
$(2,6)$	-5.37	0.14	269.22
$(2,7)$	0.15	$1.07{\cdot}10^{-4}$	279.23
$(2,8)$	-11.54	0.66	281.32
$(3,4)$	6.57	0.05	65.88
$(3,5)$	0.37	$3.27{\cdot}10^{-4}$	135.38
$(3,6)$	0.07	$1.77{\cdot}10^{-5}$	190.22
$(3,7)$	6.59	0.15	200.23
$(3,8)$	0.05	$9.06{\cdot}10^{-6}$	202.32
$(4,5)$	6.81	0.06	69.50
$(4,6)$	0.42	$3.80{\cdot}10^{-4}$	124.34
$(4,7)$	2.33	0.01	134.34
$(4,8)$	-0.14	$4.62{\cdot}10^{-5}$	136.44
$(5,6)$	7.28	0.05	54.84

(i,j)	d_{ij} (Å)	f_{ij}	E_{ij} (meV)
$(5,7)$	0.99	$1.12 \cdot 10^{-3}$	64.84
$(5,8)$	-2.48	0.01	66.94
$(6,7)$	1.68	$4.99 \cdot 10^{-4}$	10.00
$(6,8)$	-33.04	0.23	12.10
$(7,8)$	3.82	$5.37 \cdot 10^{-4}$	2.10

Table D.2: Transition dipole moment, oscillator strength and energy difference between any combination of energy levels $(i,\ j)$ in the 4.4μm step-well structure. The values of i and j refer to the labels in Figure 4.7.

Bibliography

[1] B. Levine, K. Choi, C. Bethea, J. Walker, R. Malik, *Applied Physics Letters* **1987**, *50*, 1092–1094.

[2] L. Gendron, M. Carras, A. Huynh, V. Ortiz, C. Koeniguer, V. Berger, *Applied Physics Letters* **2004**, *85*, 2824–2826.

[3] F. R. Giorgetta, E. Baumann, M. Graf, Q. Yang, C. Manz, K. Kohler, H. E. Beere, D. A. Ritchie, E. Linfield, A. G. Davies, Y. Fedoryshyn, H. Jackel, M. Fischer, J. Faist, D. Hofstetter, *IEEE Journal of Quantum Electronics* **2009**, *45*, 1039–1052.

[4] D. Palaferri, Y. Todorov, A. Bigioli, A. Mottaghizadeh, D. Gacemi, A. Calabrese, A. Vasanelli, L. Li, A. G. Davies, E. H. Linfield, F. Kapsalidis, M. Beck, J. Faist, C. Sirtori, *Nature* **2018**, *556*, 85–88.

[5] `https://es.infratec.eu/thermography/`.

[6] M. Eck, PhD thesis, Albert-Ludwigs-Universitaät Freiburg im Breisgau, **2014**.

[7] M. A. Khalighi, M. Uysal, *IEEE Communications Surveys & Tutorials* **2014**, *16*, 2231–2258.

[8] C. Subran, M. Radunsky, M. Henson, *Photoniques* **2011**, 52–55.

[9] P. Corrigan, R. Martini, E. A. Whittaker, C. Bethea, *Optics Express* **2009**, *17*, 4355.

[10] A. Rogalski, *Opto-Electronics Review* **2012**, *20*, 279–308.

[11] M. Henini, M. Razeghi, *Handbook of Infra-red Detection Technologies*, Elsevier, **2002**.

[12] B. V. Emmanuel Rosencher, *Optoelectronics*, Cambridge University Press, **2011**.

[13] W. Lawson, S. Nielsen, E. Putley, A. Young, *Journal of Physics and Chemistry of Solids* **1959**, *9*, 325–329.

[14] `http://www.mercuryconvention.org/`.

[15] H. Schneider, H. C. Liu, *Quantum well infrared photodetectors*, Springer, **2007**.

[16] A. P. Ravikumar, G. Chen, K. Zhao, Y. Tian, P. Prucnal, M. C. Tamargo, C. F. Gmachl, A. Shen, *Applied Physics Letters* **2013**, *102*, 161107.

[17] J. Faist, F. Capasso, D. L. Sivco, C. Sirtori, A. L. Hutchinson, A. Y. Cho, *Science* **1994**, *264*, 553–556.

[18] A. Vardi, G. Bahir, F. Guillot, C. Bougerol, E. Monroy, S. E. Schacham, M. Tchernycheva, F. H. Julien, *Applied Physics Letters* **2008**, *92*, 011112.

[19] M. Graf, G. Scalari, D. Hofstetter, J. Faist, H. Beere, E. Linfield, D. Ritchie, G. Davies, *Applied Physics Letters* **2004**, *84*, 475–477.

[20] A. Vardi, N. Kheirodin, L. Nevou, H. Machhadani, L. Vivien, P. Crozat, M. Tchernycheva, R. Colombelli, F. H. Julien, F. Guillot, C. Bougerol, E. Monroy, S. Schacham, G. Bahir, *Applied Physics Letters* **2008**, *93*, 193509.

[21] P. Offermans, *Study of III-V semiconductor nanostructures by cross-sectional scanning tunneling microscopy*, Citeseer, **2005**.

[22] J. H. Davies, *The Physics of Low-Dimensional Semiconductors*, Cambridge University Press, **2010**.

[23] M. Grundmann, *The Physics of Semiconductors*, Springer-Verlag GmbH, **2016**.

[24] P. Harrison, A. Valavanis, *Quantum wells, wires and dots: theoretical and computational physics of semiconductor nanostructures*, John Wiley & Sons, **2016**.

[25] L. C. West, S. J. Eglash, *Applied Physics Letters* **1985**, *46*, 1156–1158.

[26] H. C. Liu, F. Capasso, *Intersubband Transitions in Quantum Wells: Physics and Device Applications, Volume 62 (Semiconductors & Semimetals)*, Academic Press, **1999**.

[27] G. Bastard, *Paris: Les Ed. de Physique* **1988**.

[28] C. Sirtori, F. Capasso, J. Faist, S. Scandolo, *Physical Review B* **1994**, *50*, 8663–8674.

[29] F. R. Giorgetta, E. Baumann, R. Théron, M. L. Pellaton, D. Hofstetter, M. Fischer, J. Faist, *Applied Physics Letters* **2008**, *92*, 121101.

[30] P. Reininger, B. Schwarz, H. Detz, D. MacFarland, T. Zederbauer, A. M. Andrews, W. Schrenk, O. Baumgartner, H. Kosina, G. Strasser, *Applied Physics Letters* **2014**, *105*, 091108.

[31] C. Koeniguer, G. Dubois, A. Gomez, V. Berger, *Physical Review B* **2006**, *74*.

[32] A. Gomez, N. Péré-Laperne, L.-A. de Vaulchier, C. Koeniguer, A. Vasanelli, A. Nedelcu, X. Marcadet, Y. Guldner, V. Berger, *Physical Review B* **2008**, *77*.

[33] A. Delga, PhD thesis, Université Paris Diderot, **2012**.

[34] Z. Asghari, PhD thesis, Université Paris Diderot, **2019**.

[35] S. M. Sze, *Physics of Semiconductor Devices*, Wiley-Blackwell, **2006**.

[36] M. J. Adams, *An Introduction to Optical Waveguide*, John Wiley & Sons Inc, **1981**.

[37] K. Okamoto, *Fundamentals of Optical Waveguides*, Academic Press, **2005**.

[38] Y. N. Chen, Y. Todorov, B. Askenazi, A. Vasanelli, G. Biasiol, R. Colombelli, C. Sirtori, *Applied Physics Letters* **2014**, *104*, 031113.

[39] Y. Todorov, L. Tosetto, J. Teissier, A. M. Andrews, P. Klang, R. Colombelli, I. Sagnes, G. Strasser, C. Sirtori, *Optics Express* **2010**, *18*, 13886.

[40] D. Palaferri, PhD thesis, Université Paris Diderot, **2018**.

[41] Y. Xu, Y. Li, R. K. Lee, A. Yariv, *Physical Review E* **2000**, *62*, 7389–7404.

[42] A. Bitzer, H. Merbold, A. Thoman, T. Feurer, H. Helm, M. Walther, *Optics Express* **2009**, *17*, 3826.

[43] D. Palaferri, Y. Todorov, A. Mottaghizadeh, G. Frucci, G. Biasiol, C. Sirtori, *New Journal of Physics* **2016**, *18*, 113016.

[44] D. Palaferri, Y. Todorov, Y. N. Chen, J. Madeo, A. Vasanelli, L. H. Li, A. G. Davies, E. H. Linfield, C. Sirtori, *Applied Physics Letters* **2015**, *106*, 161102.

[45] D. Palaferri, Y. Todorov, D. Gacemi, S. Barbieri, L. H. Li, A. G. Davies, E. H. Linfield, C. Sirtori, *Applied Physics Letters* **2018**, *113*, 161105.

[46] Y. N. Chen, PhD thesis, Université Paris Diderot, **2015**.

[47] B. C. Smith, *Fundamentals of Fourier Transform Infrared Spectroscopy*, CRC Press, **2011**.

[48] O. Gravrand, J. Wlassow, L. Bonnefond in High Energy, Optical, and Infrared Detectors for Astronomy VI, (Eds.: A. D. Holland, J. Beletic), SPIE, **2014**.

[49] N. W. Ashcroft, N. D. Mermin, *Solid State Physics*, Thomson Learning, **1976**.

[50] P. M. Yu, M. Cardona, *Fundamentals of Semiconductors: Physics And Materials Properties, Volume 3*, Springer, **2010**.

[51] M. L. Cohen, J. R. Chelikowsky, *Electronic Structure and Optical Properties of Semiconductors*, Springer, **2012**.

[52] I. Vurgaftman, J. R. Meyer, L. R. Ram-Mohan, *Journal of Applied Physics* **2001**, *89*, 5815–5875.

[53] E. O. Kane, *Journal of Physics and Chemistry of Solids* **1957**, *1*, 249–261.

[54] J. Faist, *Quantum cascade lasers*, OUP Oxford, **2013**.

[55] G. Pegolotti, PhD thesis, Université Paris Diderot, **2015**.

[56] W. H. Press, S. A. Teukolsky, W. T. Vetterling, B. P. Flannery, *Numerical Recipes: The Art of Scientific Computing*, Cambridge University Pr., **2007**.

[57] T. P. Pearsall, R. Carles, J. C. Portal, *Applied Physics Letters* **Mar. 1983**, *42*, 436–438.

[58] T. Ando, A. B. Fowler, F. Stern, *Reviews of Modern Physics* **1982**, *54*, 437–672.

[59] T. Unuma, M. Yoshita, T. Noda, H. Sakaki, H. Akiyama, *Journal of Applied Physics* **2003**, *93*, 1586–1597.

[60] A. Vasanelli, A. Leuliet, C. Sirtori, A. Wade, G. Fedorov, D. Smirnov, G. Bastard, B. Vinter, M. Giovannini, J. Faist, *Applied Physics Letters* **2006**, *89*, 172120.

[61] R. Ferreira, G. Bastard, *Physical Review B* **1989**, *40*, 1074–1086.

Acknowledgements

This thesis work has been carried out at LPENS laboratories, inside the QUAD group, at École Normale Supérieure in Paris.

I would like to thank Professor Daniela Cavalcoli, my supervisor from the University of Bologna, for motivating me to have this experience and for the constant help she gave me from the beginning.

A special thanks to Professor Carlo Sirtori, my supervisor from École Normale Supérieure, for giving me the possibility to work in his group and for his continuous help and support during this experience in Paris. His guide has been essential to the fulfillment of this thesis work.

I would like to thank PhD student Azzurra Bigioli for introducing me to the laboratory and helping me from the first to the last day of my internship. It has been a pleasure for me working at her side every day during this experience.

I thank Professor Angela Vasanelli for her precious help in understanding and modifying the code for the active region simulations.

I also thank researcher Yanko Todorov and research engineer Djamal Gacemi for their help in solving both conceptual and technical problems in the laboratory.

Finally, I want to thank all the post-doc, PhD and master students of the QUAD group: Mathieu Jeannin, Gregoire Vallet, Allegra Calabrese, Andy Haky, Masoud Kheyri, Thomas Bonazzi and Hamza Dely. Each one of them kindly helped and supported me during this experience.

Ringrazio i miei genitori, che mi hanno supportato dall'inizio alla fine del mio percorso di studi, aiutandomi e sostenendomi in ogni mia scelta. Senza di loro raggiungere questo traguardo non sarebbe stato possibile.

Ringrazio infine a Caterina, per il sostegno e la forza che da sempre mi dà, per essere stata la mia complice nei momenti più gioiosi e la mia àncora nei momenti più difficili.